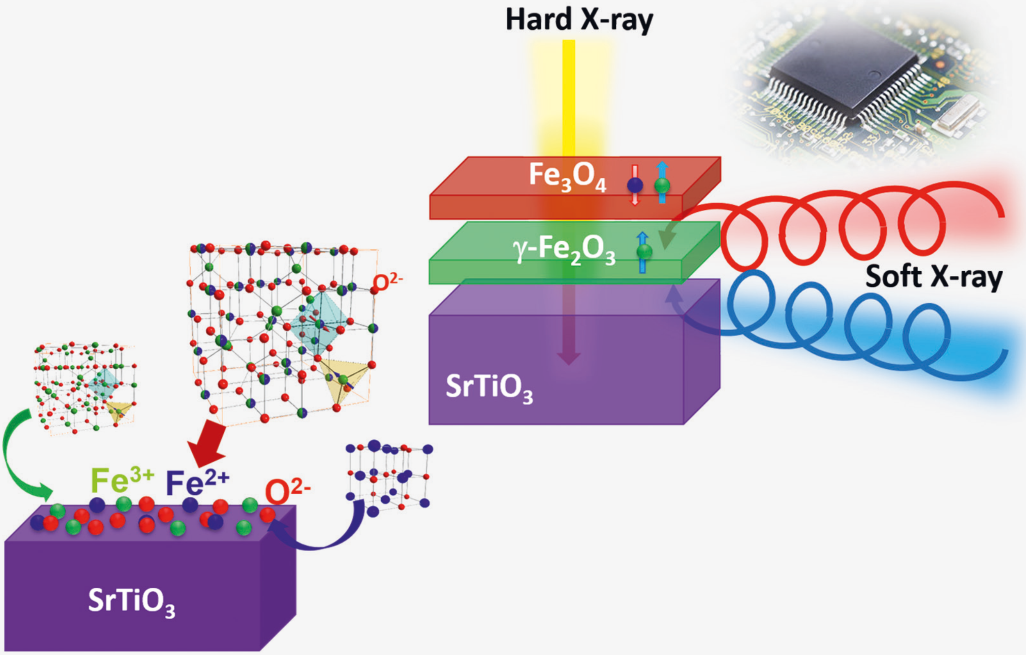

Interface Functionalization of Magnetic Oxide Fe_3O_4/$SrTiO_3$ Heterostructures

Mai Hussein Abdalla Hamed

Schlüsseltechnologien / Key Technologies
Band / Volume 231
ISBN 978-3-95806-535-2

Mitglied der Helmholtz-Gemeinschaft

Schriften des Forschungszentrums Jülich
Reihe Schlüsseltechnologien / Key Technologies Band / Volume 231

Forschungszentrum Jülich GmbH
Peter Grünberg Institut (PGI)
Elektronische Eigenschaften (PGI-6)

Interface Functionalization of Magnetic Oxide $Fe_3O_4/SrTiO_3$ Heterostructures

Mai Hussein Abdalla Hamed

Schriften des Forschungszentrums Jülich
Reihe Schlüsseltechnologien / Key Technologies Band / Volume 231

ISSN 1866-1807 ISBN 978-3-95806-535-2

Bibliografische Information der Deutschen Nationalbibliothek.
Die Deutsche Nationalbibliothek verzeichnet diese Publikation in der
Deutschen Nationalbibliografie; detaillierte Bibliografische Daten
sind im Internet über http://dnb.d-nb.de abrufbar.

Herausgeber und Vertrieb: Forschungszentrum Jülich GmbH
Zentralbibliothek, Verlag
52425 Jülich
Tel.: +49 2461 61-5368
Fax: +49 2461 61-6103
zb-publikation@fz-juelich.de
www.fz-juelich.de/zb

Umschlaggestaltung: Grafische Medien, Forschungszentrum Jülich GmbH

Druck: Grafische Medien, Forschungszentrum Jülich GmbH

Schriften des Forschungszentrums Jülich
Reihe Schlüsseltechnologien / Key Technologies, Band / Volume 231

D 464 (Diss. Duisburg, Univ., 2021)

ISSN 1866-1807
ISBN 978-3-95806-535-2

Zusammenfassung

Oxidheterostrukturen besitzen eine große Auswahl an elektrischen und magnetischen Eigenschaften, die insbesondere durch Wechselwirkungen an ihren Grenzflächen entstehen. Eine der größten Herausforderungen ist es magnetische Eigenschaften auf atomarer Ebene von Oxidheterogrenzflächen zu entwerfen und zu kontrollieren. In diesem Kontext ist das Verbinden von Übergangsmetalloxiden zu Heterostrukturen, aufgrund ihrer bemerkenswerten Eigenschaften wie aufkommende Leitfähigkeit, Magnetismus oder Ferroelektrizität, sehr vielversprechend. Darüber hinaus sind Eisenoxide, einschließlich FeO, Fe_3O_4 und Fe_2O_3 Polymorphe (α-Fe_2O_3, γ-Fe_2O_3...) mit ihrer Vielzahl an elektrischen und magnetischen Funktionalitäten, sehr interessant für viele magnetische Anwendungen und heterogene Katalyse. Die Steuerung der Oxidgrenzflächen stärkt zusätzlich die Herstellung von funktionalen Bauteilen. Daher ist unser Hauptziel das Verstehen, die Kontrolle und das Optimieren der Grenzflächeneigenschaften.

Zu diesem Zweck demonstrieren wir die Entstehung und Kontrolle von magnetischen Grenzflächen zwischen Magnetit Fe_3O_4, einem ferrimagnetischen Halbmetall, und $SrTiO_3$, einem transparenten diamagnetischen Isolator, der als das Fundament für oxidbasierte Elektronik gilt. Es wurde festgellt, dass der Verwey-Übergang (T_V) von volumenartigen bis zu ultradünnen Fe_3O_4-Filmen fortbesteht und von 117±4 K (38 nm) bis 25±4 K (2 nm) abnimmt. Elementselektive elektronische und magnetische Eigenschaften von ultradünnen Filmen und verdeckten Grenzflächen werden mit winkelabhängigem HAXPES- und XMCD-Techniken untersucht. Wir beweisen, dass die $SrTiO_3$ Substrate sowohl Kristallverspannung als auch Grenzflächenoxidation induzieren. Die substratinduzierte Kristallverspannung führt zu der Neuausrichtung der Easy-Achse zu [100]. Des Weiteren beobachten wir mit abnehmender Filmdicke eine Reduktion von Fe^{2+}-Ionen begleitet von einer Zunahme der Fe^{3+}-Ionen sowohl auf tetraedrischen als auch oktaedrischen Positionen, woraus wir auf eine Bildung einer magnetisch aktiven, ferrimagnetischen 2 u.c. γ-Fe_2O_3 Zwischenschicht schließen. Um die magnetischen Grenzflächenphase zu manipulieren wird ein Nachglühprozess durchgeführt, der eine kontrollierte Reduktion des γ-Fe_2O_3 auslöst und somit schlussendlich zu eine stöchiometrischen und ferrimagnetischen Fe_3O_4/$SrTiO_3$ (001) Heterogrenzfläche führt.

Wir weisen die thermisch induzierten Phasenumwandlung zischen Fe_3O_4, γ-Fe_2O_3 und FeO ultradünnen Eisenoxidfilmen nach, die ein Anteil von All-Oxide-Heterostrukturen sind, und stellen eine umfassende thermodynamische Analyse der entstehenden Grenzflächen Redox Prozesse durch aktive Redox Reaktionen über drei relevante Grenzflächen vor: (1) die Außenatmosphäre/Fe_xO_y Film Grenzfläche, (2) die Grenzfläche zwischen Fe_xO_y/Fe_xO_y Zwischenschichten and (3) die Fe_xO_y/Oxidsubstrate Grenzfläche. Dabei decken wir die essentielle – aber meistens vernachlässigte – Rolle der Oxidsubstrate auf, die als zusätzlicher Sauerstofflieferant oder als Sauerstoffabnehmer das Standard FexOy Temperatur-Druck- Phasendiagramm vollständig ändern kann. Wir stellen ein angepasstes Phasendiagramm speziell für die Fe_xO_y/Nb:$SrTiO_3$ und Fe_xO_y/YSZ Heterostrukturen basierend auf gesamte effektive Sauerstoffaktivität vor.

Unsere Studie geht über die derzeitige Funktionalisierung von Oxidheterostrukturen und deren Phasenübergänge hinaus. Dieser neuartige Ansatz eröffnet einen Weg zum reversiblen Tuning von physikalischen Funktionalitäten und damit zu einer zukünftigen Integration von $Fe_3O_4/SrTiO_3$-Heterostrukturen in resistiven und magnetisch schaltenden Bauteilen.

Abstract

Oxide heterostructures possess a wide range of electrical and magnetic properties, mainly via interactions across their interfaces. The prospect of designing and controlling the magnetic properties at the atomic scale of oxide heterointerfaces is one of the major challenges. In this context, merging transition-metal oxides into heterostructures is very promising, owing to their many remarkable properties, such as emerging conductivities, magnetism or ferroelectricity. Furthermore, iron oxides including FeO, Fe_3O_4 and Fe_2O_3 polymorphs (α-Fe_2O_3, γ-Fe_2O_3...) with a multitude of electric and magnetic functionalities are interesting for many magnetic applications and heterogeneous catalysis. Controlling the oxide interfaces additionally strengthens the manufacturing of functional devices. Therefore, our primary goal is understanding, controlling and tuning the interface properties.

For this purpose, we demonstrate the emergence and control of magnetic interfaces between magnetite Fe_3O_4, a ferrimagnetic half-metal, and $SrTiO_3$, a transparent non-magnetic insulator which is considered the bedrock of oxide-based electronics. The Verwey transition (T_V) is found to persist from bulk-like down to ultrathin Fe_3O_4 films, decreasing from 117±4 K (38 nm) to 25±4 K (2 nm), respectively. Element-selective electronic and magnetic properties of the ultrathin films and buried interfaces are studied by angle-dependent HAXPES and XMCD techniques. We prove that the $SrTiO_3$ substrates induce both strain and interface oxidation. The substrate-induced strain causes the easy axis to switch to [100]. Furthermore, we observe a reduction of Fe^{2+} ions with decreasing film thickness, accompanied by an increase of Fe^{3+} ions in both tetrahedral and octahedral sites, and conclude on the formation of a magnetically active ferrimagnetic 2 u.c. γ-Fe_2O_3 intralayer. To manipulate the interfacial magnetic phase, a post-annealing process is conducted which causes the reduction of the γ-Fe_2O_3 that finally leads to stoichiometric and ferrimagnetic $Fe_3O_4/SrTiO_3$ (001) heterointerfaces.

We demonstrate the thermally induced phase transformations between Fe_3O_4, γ-Fe_2O_3 and FeO ultrathin iron oxide films, which are part of all-oxide heterostructures, and present a comprehensive thermodynamic analysis of the emerging interfacial redox processes through active redox reactions across three relevant interfaces, i.e. (1) the outside atmosphere/Fe_xO_y film interface, (2) the interface between Fe_xO_y/Fe_xO_y intralayers and (3) the Fe_xO_y/oxide substrate interface. We thereby reveal the essential – but mostly underrated – role of oxide substrates, which can completely alter the standard Fe_xO_y temperature-pressure phase diagram as an additional oxygen supplier or scavenger. We introduce an adjusted phase diagram specifically for Fe_xO_y/ Nb:$SrTiO_3$ and Fe_xO_y / YSZ heterostructures based on a total effective oxygen activity.

Our study goes beyond the current functionalization of oxide heterostructures and their phase transitions. This novel approach opens up the route towards reversible tuning of the physical functionalities, thus, a future integration of $Fe_3O_4/SrTiO_3$ heterostructures into resistive and magnetic switching devices.

Contents

List of Tables

List of Figures

CHAPTER 1

Introduction

Currently, conventional electronics is based on semiconductor technology and information which is carried and manipulated by the charge of the electrons. The development possibilities of this semiconductor technology described by Moore's law predict that the number of transistors integrated into a circuit doubles about every two years. Although this trend of electronics development has been true for several decades, it recently started slowing down. However, the need for electronics development to be highly efficient in terms of speed, storage capacity, multi-functionality, and power consumption, is continuously increasing. Thus, a new field has emerged known as spintronics. In spintronics, the spin of the electrons is added as another degree of freedom for information transport. Spintronics evolved after the discovery of giant magnetoresistance (GMR) effect by Nobel laureates: Albert Fert [1] and Peter Grünberg [2]. Tunnel magnetoresistance (TMR) is another spintronics effect, which can be utilized in devices that are built by half-metal magnetic materials.

Many oxides have been predicted to be "half-metallic", i.e. highly spin-polarized, for example: (1) the ferromagnetic manganites $La_{1-x}Ca_xMnO_3$ [3] and $La_{1-x}Sr_xMnO_3$ [4]. For both material systems, a remarkably high TMR at very low temperature has been observed [5]. Therefore, the search for half-metal oxides with higher Curie temperature T_C becomes essential. (2) The ferrimagnetic magnetite Fe_3O_4 with a T_C of 860 K: the experimental spin-polarization at the Fermi level using photoemission spectroscopy has been found to be at most $-80\,\%$ [6, 7]. However, the theoretical calculations predict a value of $-100\,\%$ [8, 9]. Surprisingly, positive values for the spin-polarization of Fe_3O_4 have been reported through transport measurements at many experiments [10–12]. This disparity in sign may be attributed to the oxygen off-stoichiometry of the magnetite films or the emerging electronic properties of the interfaces within the different oxide heterostructures. Although, the control of spin-polarization of the magnetite is a challenge, magnetite is still a promising candidate for spintronics. If interfaced with oxides, exciting phenomena arise, such as spin-dependent transport [13–17] or spin Seebeck effect [18].

Magnetite is one of the oldest known magnetic materials which interestingly has been found in many biological systems. Magnetite particles have been discovered in pigeons' beaks which navigate them precisely through the Earth's magnetic field [19]. Magnetite has also been found in "freshwater magnetotactic bacteria" where magnetite helps them to orient [20]. In addition to bacteria and animals, magnetite has also been discovered in the human brain [21]. In general, iron oxides (Fe_xO_y) also have a wide range of electric and magnetic properties (the details will be discussed in Chapter 2). For spintronics, the possibility of a controlled interconversion via chemical phase transitions between the different iron oxides functional phases may open up novel routes to control magnetic states and spin-based phenomena on a nanometer scale. For example, the ability to switch between ferrimagnetic and antiferromagnetic states in ultrathin iron oxide films may enable us to efficiently tune spin-dependent transport.

Oxide-oxide heterostructures offer an extensive variety of electronic and magnetic properties, which are considered the foundation for the current spintronics research. In particular, this concerns their oxide interfaces which reveal emergent phenomena. One example is the formation of a conducting two-dimensional electron gas (2DEG) at the interface of insulating heteroepitaxial oxides [22, 23]. A second example is the formation of magnetic interfaces between non-magnetic oxides [24]. The substrate for these studies is mostly $SrTiO_3$. In this thesis, the focus will be on the interfacial properties between Fe_3O_4 and $SrTiO_3$.

Motivated by the interesting properties of the magnetite and the different iron oxides phases, the goals of this thesis are (1) investigating the electronic and magnetic properties of the iron oxide/substrate interfaces, (2) understanding the interfacial thermodynamic properties, (3) controlling the redox process and (4) tuning the electronic and magnetic properties of Fe_xO_y films grown on "active" oxide substrates.

The thesis is structured as follows: in Chapter 2, we introduce the theoretical aspects describing the different iron oxides phases, focusing on the Fe_3O_4. Afterwards, the properties of the oxides substrates which have been used in this work are discussed. In particular, $SrTiO_3$ (STO) as "active" substrate and yttrium stabilized zirconia (YSZ) as "inert" substrate are proposed. The last part of this chapter is devoted to the physical chemistry, in particular, the surface energies of the iron oxides phases and $SrTiO_3$ with different surface terminations and the corresponding Ellingham diagram.

In Chapter 3, the experimental techniques which have been employed in this work are explained. The Fe_3O_4 thin films have been grown by pulsed laser deposition (PLD). The structure and magnetic properties of the films have been measured using atomic force microscopy (AFM), X-ray diffraction (XRD), and vibrating sample magnetometer (VSM). Element-selective and depth-dependent chemical and magnetic information of the films and buried interfaces have been probed by synchrotron methods; i.e. hard X-ray photoemission spectroscopy (HAXPES), X-ray absorption spectroscopy (XAS) and X-ray magnetic circular dichroism (XMCD).

Chapter 4 focuses on the optimization of the growth parameters of Fe_3O_4 thin films. The central point of this chapter is studying the influence of growth temperature on the magnetic properties of the Fe_3O_4/Nb:$SrTiO_3$ heterostructures. We address the switching of the magnetic easy axis direction caused by (1) the large mismatch between the film and the substrate which induces magnetostriction, and (2) the Verwey transition which induces additional structure anisotropy. For this study, we conducted HAXPES and XMCD techniques to investigate the stoichiometry of Fe_3O_4 films. VSM has been used in order to investigate the magnetic properties of the samples at a temperature higher and lower than the Verwey transition. Additionally, we used the VSM to explore the switching of the magnetic easy axis. From these studies, we found that the magnetic properties are significantly manipulated by (1) the underlying oxide substrate $SrTiO_3$ and (2) the growth temperature.

The effect of the $SrTiO_3$ substrate on the chemical and electronic structure of the iron oxides at the interface has been studied in Chapter 5. We study the effect of reduced dimensionality on electronic and magnetic properties. The element-selective electronic and magnetic properties of the ultrathin films and buried interfaces are probed by HAXPES and XMCD. XMCD spectra are compared to model spectra and the cation ratio of Fe^{2+} and Fe^{3+} are calculated. We propose that the $SrTiO_3$ substrates supply oxygen for the Fe_3O_4 films which leads to the creation of an interfacial γ-Fe_2O_3 intralayer. We tuned between the ferrimagnetic γ-Fe_2O_3 and Fe_3O_4 phases by careful annealing treatment for the films in oxygen pressure.

In Chapter 6, we investigate the properties of Fe_3O_4 films grown on the inert YSZ substrates at different growth temperatures and different thicknesses. We used XRD and VSM to examine the quality of bulk films. Furthermore, we conducted HAXPES to study the chemical properties of the interfaces. We detect the formation of the Fe_2O_3 phase in addition to the Fe_3O_4 phase for the ultrathin films. Thus, the YSZ as well as the STO substrates disturb the effective oxygen pressure and form interfacial oxidized phases.

We present a comparative annealing study for Fe_3O_4 films grown on Nb:STO and YSZ in Chapter 7. Using HAXPES, we study the redox reactions and the thermodynamics of the heterostructures at three relevant interfaces: (A) the atmosphere/Fe_xO_y film interface, (B) the interface between phase-transformed Fe_xO_y/Fe_xO_y intralayers and (C) the Fe_xO_y/substrate interface. Our results suggested that the heterostructures do not obey the standard phase diagram of iron oxides because of the additional oxygen supply from the substrates. Utilizing the van 't Hoff analysis and thermodynamics concepts, we calculate the total effective oxygen pressure which leads to an "adjusted" phase diagram for iron oxides in all-oxide heterostructures with $SrTiO_3$.

Finally, we summarize the main results discussed in the thesis, and some open questions and outlook for future investigations in Chapter 8. The knowledge acquired in this thesis improves considerably our understanding of the magnetic oxide interfaces. This will enable us to tailor and engineer a new device structure for future use in spintronics.

CHAPTER 2

Theoretical background

The major aim of this thesis is to investigate the interfacial properties of $Fe_3O_4/SrTiO_3$ heterostructures, controlling and tuning the electronic and magnetic properties of the interfaces. Therefore, before diving into the details of the experimental results, we will focus in this chapter on some theoretical background, which will guide our discussion in the next chapters. First, in Section 2.1, we will give an overview of the characterization of the iron oxides in general, and magnetite in particular. Second, in Section 2.2, we will introduce the properties of the oxide substrates $SrTiO_3$ and YSZ. In the last step, in Section 2.3, we will introduce thermodynamic concepts at oxides interfaces, which will help to understand the chemical reactions and their favour ability to occur.

2.1 Magnetite versus other iron oxides

The iron oxides have varieties of magnetic and electric properties. In particular, magnetite Fe_3O_4 is a ferrimagnetic half-metallic material. The reduced phase of magnetite is wüstite, $Fe_{1\text{-x}}O$, which is antiferromagnetic. On the other hand, the oxidized phase for Fe_3O_4 is Fe_2O_3, which has different phases. The well-known phases are γ-Fe_2O_3 (ferrimagnetic insulator) and α-Fe_2O_3 (antiferromagnetic insulator). Thus, tuning the magnetic and electric properties can be achieved by controlling the oxidation and reduction of the Fe_3O_4 phase (Figure 2.1). Therefore, we will explain the properties of iron oxides briefly with the focus on the magnetite phase.

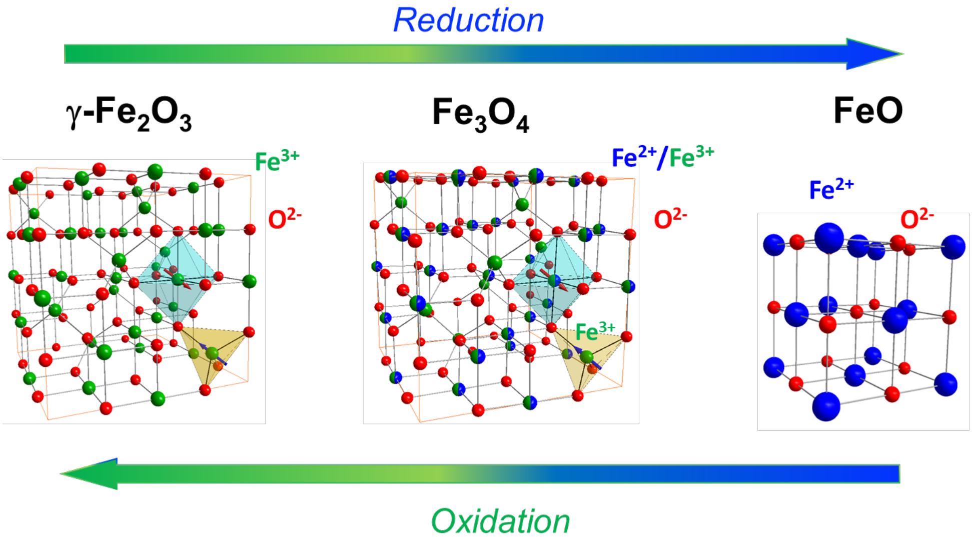

Figure 2.1: Unit cells of the iron oxide phases γ-Fe_2O_3, Fe_3O_4 and $Fe_{1\text{-}x}O$ and the thermodynamical processes driving the oxidation-reduction reactions of the chemical phase transitions. Middle, the inverse spinel Fe_3O_4 unit cell with Fe^{3+} cations (green) equally occupy tetra- (T_d) and octahedral (O_h) sites, while Fe^{2+} cations (blue) occupy O_h sites. Left, the inverse spinel γ-Fe_2O_3 unit cell with Fe^{3+} cations (green) distributed to the tetra- (T_d) and octahedral (O_h) sites. Right, the rock salt $Fe_{1\text{-}x}O$ unit cell with Fe^{2+} cations (blue) and oxygen (red).

2.1.1 The ferrimagnetic half-metal: Magnetite (Fe_3O_4)

Magnetite exhibits a multitude of interesting properties. It is a ferrimagnetic material with a high Curie temperature of $T_C = 860\,\mathrm{K}$. It is a half-metal with a negative spin polarization of up to $-100\,\%$ at the Fermi level. From band theory calculations, the t_{2g} spin-down bands of the octahedral O_h sites are located at the Fermi level E_f, while the spin-up bands reveal a gap at E_f [25]. Furthermore, magnetite possesses a conductor-insulator transition below the Verwey temperature at $\approx 120\,\mathrm{K}$.

Crystalline structure

Magnetite takes an inverse spinel structure with a crystal lattice constant of 8.394 Å [26]. The respective unit cell is depicted in Figure 2.1. It has a cubic Fd$\bar{3}$m (227) structure which can be written as $[Fe^{3+}]_{T_d}[Fe^{2+}Fe^{3+}]_{O_h}O_4$. The tetrahedral sites are occupied by Fe^{3+} cations and the octahedral sites are occupied evenly by Fe^{3+} and Fe^{2+}. This specific occupation of Fe^{2+} and Fe^{3+} cations is responsible for the ferrimagnetic and electric properties of magnetite.

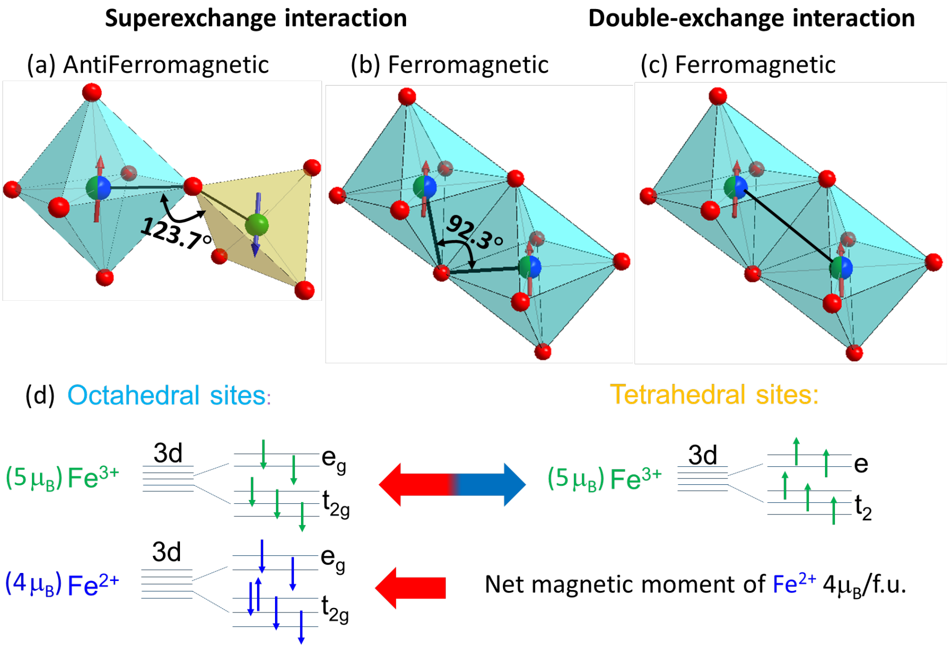

Figure 2.2: Schematics describe the magnetism in the inverse spinel magnetite through first the superexchange interaction: (a) the antiferromagnetic coupling between the cations on the T_d and on the O_h sites and (b) the ferromagnetic coupling between the cations on the O_h sites. Second, the double-exchange interaction: (c) the ferromagnetic coupling between the O_h sites. (d) The valence states of the cations on the O_h and T_d sites and the net magnetic moment of Fe^{2+} equals $4\,\mu_B$/f.u..

Magnetic properties

The ferrimagnetism of Fe_3O_4 is a consequence of the antiferromagnetic coupling between tetrahedral (T_d) and octahedral (O_h) cations and the ferromagnetic coupling between the octahedral Fe^{2+} ($3d^6$) and Fe^{3+} ($3d^5$) cations, as shown in Figure 2.2. The antiferromagnetic and ferromagnetic coupling mechanisms result from the indirect exchange interactions, the superexchange and double-exchange. These interactions can be described using the rules of Goodenough [27], Kanamori [28] and Anderson [29]. First, the antiferromagnetic coupling between the T_d and O_h cations is induced by the superexchange interaction mediated by an overlap of the Fe 3d orbitals with the intermediate oxygen 2p orbitals at an angle of about 125° (Figure 2.2 (a)). Second, the ferromagnetic coupling between Fe^{2+} and Fe^{3+} cations on the O_h sites is driven by two indirect exchange mechanisms: (1) the superexchange interaction at an angle of 92.3° between Fe^{2+}-O-Fe^{3+}, and (2) the double-exchange interaction, which causes both the delocalization of the extra electron of Fe^{2+} and the conductivity of Fe_3O_4 (Figure 2.2 (b) and (c)). As a result, the magnetic moment of the Fe^{3+} cations ($\pm 5\,\mu_B$) cancel each other

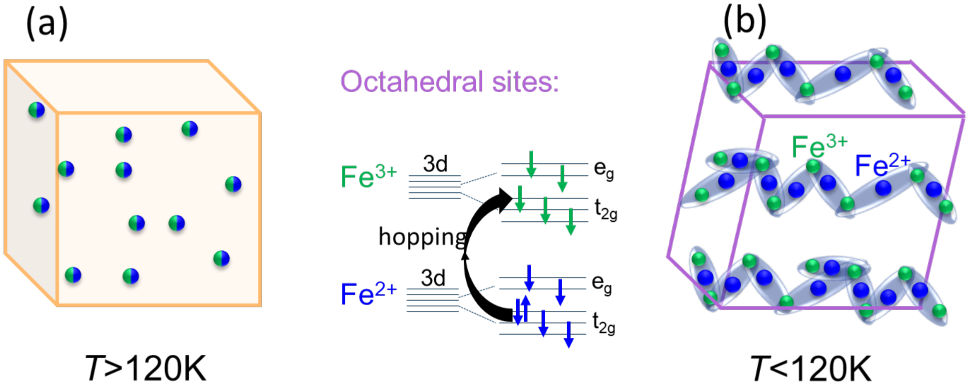

Figure 2.3: Schematics representation of the metal-insulator transition (Verwey transition) at $T = 120\,\mathrm{K}$ of Fe_3O_4, (a) $T > 120\,\mathrm{K}$: cubic structure of Fe_3O_4 unit cell and conductivity originated through hoping between the Fe^{2+} and Fe^{3+} cations on the O_h sites, and (b) $T < 120\,\mathrm{K}$: transition to monoclinic structure and charge and orbital ordering within the trimerons which consist of two end-linked Fe^{3+} (green) and one centered Fe^{2+} (blue).

out leaving the net moment of the Fe^{2+} cations, which equals $4\,\mu_B$/f.u. [30–32].

Verwey transition

Magnetite possesses an interesting first-order metal-insulator transition at $T_V = 120\,\mathrm{K}$ known as the Verwey transition [33]. At $T > 120\,\mathrm{K}$, Fe_3O_4 is a conductor with a cubic structure. The metallicity of Fe_3O_4 mainly originates from the hopping of the extra electron from Fe^{2+} ($3d^6$) to Fe^{3+} ($3d^5$), which is only possible when both Fe cations are aligned ferromagnetically (double exchange interaction) as shown in Figure 2.3 (a). At $T < 120\,\mathrm{K}$, the electron hopping freezes out and the resistivity increases by two orders of magnitude. Numerous investigations have addressed the mechanism behind the Verwey transition. According to a recent study [34], at $T < 120\,\mathrm{K}$, the charge and orbital ordering occur over three-Fe-sites called trimerons. Trimerons consist of two end-linked Fe^{3+} and one centered Fe^{2+} cations as shown in Figure 2.3 (b). They found that the Fe^{2+} electrons are not fully localized. Instead, the electrons are distributed shortly over the trimerons. Furthermore, this transition is accompanied by a structural transition from a cubic to a monoclinic phase [35]. The low-temperature monoclinic structure is magnetically ordered [36].

2.1.2 The antiferromagnetic: Wüstite ($Fe_{1\text{-}x}O$)

$Fe_{1\text{-}x}O$ with the Fe^{2+} oxidation state crystallizes in a simple rocksalt structure. It has a cubic unit cell with a lattice constant of 4.3 Å. The space group is Fm3m [37] where the Fe^{2+} cations occupy the octahedral sites (Figure 2.1). The $Fe_{1\text{-}x}O$ is a defective compound

Table 2.1: Structural, magnetic and electric properties of different iron oxide phases.

Iron Oxide	**Iron Valence**	**Crystal Structure**	**Lattice Constant**(Å)	**Magnetic Properties**	**Electric Properties**
$Fe_{1\text{-}x}O$	2+	Rock Salt	4.3	Antiferro	Depending on defects
Fe_3O_4	2+/3+	Inverse Spinel	8.394	Ferri	Half metal
γ-Fe_2O_3	3+	Defected Spinel	8.4053	Ferri	Insulator
α-Fe_2O_3	3+	Corundum	5.0355 13.7471	Antiferro	Insulator

with 1-x ranging between 0.83 to 0.95. The FeO is "contaminated" by the Fe^{3+} cations, which occupy the tetrahedral sites [38]. According to the defect distribution, $Fe_{1\text{-}x}O$ can be a good conductor [39]. At room temperature, wüstite is paramagnetic, but it exhibits antiferromagnetism with a Néel temperature of 200 K.

2.1.3 The ferrimagnetic insulator: Maghemite (γ-Fe_2O_3)

The Fe_2O_3 oxide has many different phases. The most abundant phases are the maghemite γ-Fe_2O_3 and the hematite α-Fe_2O_3. γ-Fe_2O_3 has an inverse spinel structure (Fd$\bar{3}$m), similar to Fe_3O_4 and its lattice constant equals 8.4053 Å [40]. In the γ-Fe_2O_3 unit cell, the Fe^{3+} cations occupy both tetrahedral and octahedral sites, thus, extra vacancies are located on the octahedral sites. Its structure can be written in the form of $[Fe^{3+}]_{T_d}[V_O^{\bullet\bullet}Fe^{3+}]_{O_h}O_4$, where $V_O^{\bullet\bullet}$ indicates the vacancies on O_h sites. Maghemite is a ferrimagnetic material with a Curie temperature of 820–956 K. Similar to magnetite, the tetrahedral Fe^{3+} cations are antiferromagnetically coupled with the octahedral Fe^{3+}. The Fe^{3+} are not evenly distributed on the tetrahedral and octahedral sites. Thus, the magnetization contributions from the Fe^{3+} cations do not fully cancel each other out. According to the number of vacancies, the net moment of γ-Fe_2O_3 equals $M_S = 2\text{-}2.5\,\mu_B$/f.u.. In the γ-Fe_2O_3 phase, hopping is not possible, because of the absence of Fe^{2+}, thus it is an insulator.

2.1.4 The antiferromagnetic insulator: Hematite (α-Fe_2O_3)

Hematite α-Fe_2O_3 is the only iron oxide, which does not have the cubic unit cell. It has a corundum structure with unit cell lengths ($a = 5.0355$ Å and $c = 13.7471$ Å) and its space group is R$\bar{3}$c [41]. It is an antiferromagnetic material with a Néel temperature of 260 K. In Table 2.1, we summarize the properties of the different iron oxides phases.

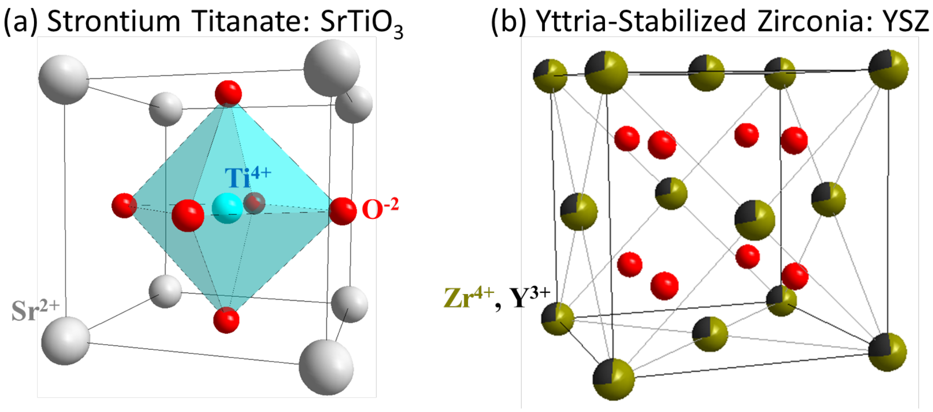

Figure 2.4: Schematics for the crystalline unit cells of: (a) the perovskite $SrTiO_3$ with Sr^{2+} (gray) cations in the corners of the cubic and Ti^{4+} (light blue) occupying the octahedral sites. (b) fcc Yttria-stabilized zirconia with Zr^{4+} (dark yellow) and Y^{3+} (black) cations.

2.2 Oxide substrates

In the scope of this thesis, we aim to investigate the effect of the oxide substrates on the properties of the Fe_3O_4 films. The interfacial redox process is highly dependent on the oxygen supply of the underlying oxide substrates. Thus, we choose two oxide substrates that have different properties with regard to the oxygen supply: strontium titanate $SrTiO_3$ is considered as "active", whereas yttria-stabilized zirconia (YSZ) is considered as "inert".

2.2.1 Strontium titanate ($SrTiO_3$)

$SrTiO_3$ (STO) has a cubic perovskite structure with a lattice constant of 3.905 Å [42]. The Sr^{2+} cations are located in the corners of the cubic and Ti^{4+} occupying the octahedral sites as shown in Figure 2.4 (a). STO is a diamagnetic insulator with a band gap of 3.25 eV [43]. By Nb doping, the STO becomes a conductor. The Nb^{5+} cations substitute Ti^{4+} which introduce additional electrons into the system. The conductivity state of the system changes but the structure and the magnetic properties remain similar.

2.2.2 Yttria-stabilized zirconia (YSZ)

Yttria-stabilized zirconia (YSZ) consists of the primary phase ZrO_2 which is monoclinic at room temperature and unstable cubic at 2370 °C. The stabilization of the cubic structure at room temperature is achieved by doping with Y_2O_3. YSZ is an insulator

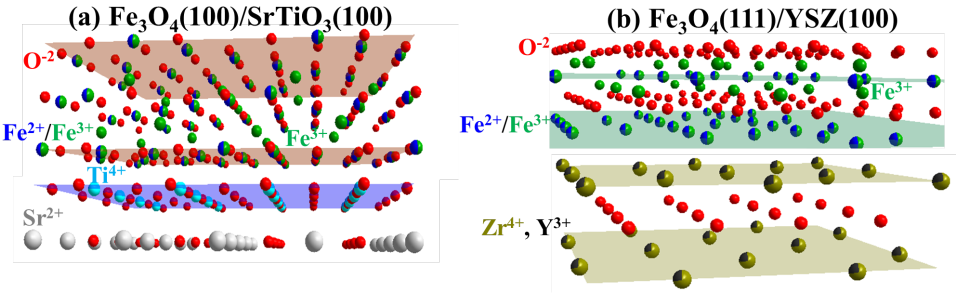

Figure 2.5: Schematics for the epitaxial growth of: (a) Fe_3O_4 (100) on TiO_2-terminated $SrTiO_3$ (100) and (b) Fe_3O_4 (111) on Yttria-stabilized zirconia YSZ (100).

Table 2.2: Calculated lattice mismatch between the iron oxides and the oxide substrates.

Oxide Substrates	**Fe_3O_4 %**			**γ-Fe_2O_3 %**			**$Fe_{1-x}O$ %**		
	(100)	(110)	(111)	(100)	(110)	(111)	(100)	(110)	(111)
$SrTiO_3$ (100)	-7.5	>20	>20	-7.6	>20	>20	-1	>20	>20
YSZ (100)	>20	-13.5	+6	>20	-13.6	+6	+1.7	>20	>20

with a cubic structure and a lattice constant of 5.16 Å [44]. The Zr^{4+} and Y^{3+} cations are located on the face-centered cubic fcc positions as shown in Figure 2.4 (b).

2.2.3 Epitaxial growth of Fe_3O_4 on oxide substrates and formation of anti-phase boundaries

The epitaxial growth of magnetite on $SrTiO_3$ is a challenge. The Fe_3O_4 unit cell has a lattice constant of 8.395 Å, which is slightly smaller than the double of the lattice constant of $SrTiO_3$. The lattice mismatch between the $SrTiO_3$ (100) and Fe_3O_4 (100) is −7.5 %, which influences the interfaces roughness and their general properties as we will discuss in Chapter 4 and 5. On the other hand, the lattice mismatch between Fe_3O_4 (100) and YSZ (100) is higher than 30 %, which forces the Fe_3O_4 unit cell to grow parallel to the (111) planes as it is shown in Figure 2.5. The new mismatch between the Fe_3O_4 (111) and YSZ (100) is 6 %. Table 2.2 shows some values for the lattice mismatch between the different iron oxides phases and the oxide substrates.

Formation of anti-phase boundaries

During the growth of Fe_3O_4 films, many defects are formed. One of the well-known defects in Fe_3O_4 films are anti-phase boundaries (APBs) [45]. The growth of the film initiates with the formation of many islands. When the neighboring islands are shifted with respect to each other, APBs are formed. This APBs structural shift is accompanied

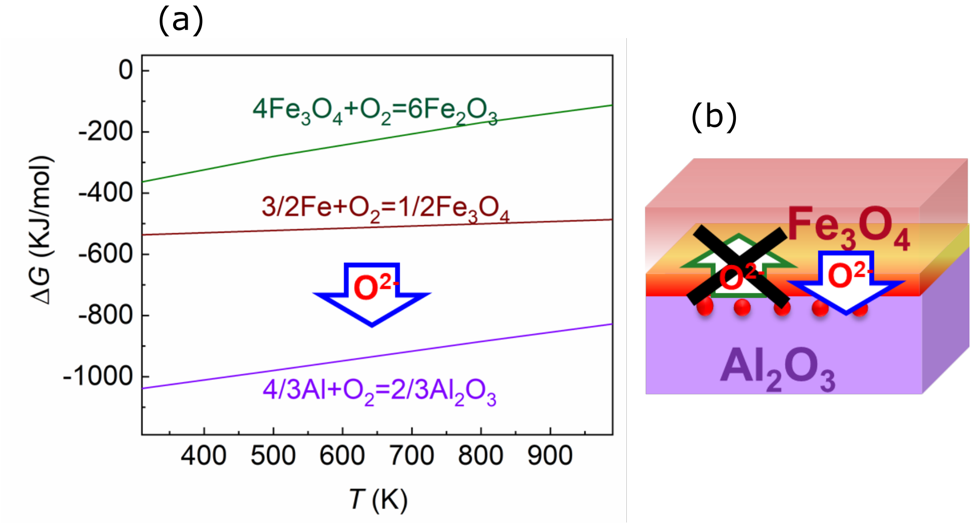

Figure 2.6: (a) Ellingham diagram of Fe_2O_3, Fe_3O_4 and Al_2O_3 calculated from the NIST database [48]. (b) A schematic for the oxide-oxide reactions at the interface between Al_2O_3 and Fe_3O_4. According to Ellingham diagram the oxygen ions can only move towards Al_2O_3.

by a repositioning of Fe cations on the octahedral sites which frustrates the superexchange interaction. The atomic structure perturbation leads to an antiferromagnetic coupling between those cations through an angle of 180° around the defect boundary [46, 47].

2.3 Fundamental aspect of physical chemistry

The migration of oxygen ions within the oxides heterostructures layers promotes novel phenomena at the interfaces. In particular, it induces phase transitions accompanied by transitions of the physical properties. The direction of the migrating oxygen ions or the direction of the oxidation (reduction) reactions within the oxide heterostructures can be predicted by understanding the thermodynamic concepts. The direction of the reactions can be extracted from the Gibbs free energy of formation for the different metal oxides and from the Ellingham diagram. The Gibbs free energy is influenced strongly by the surface termination, as will be introduced in the following subsection.

2.3.1 Ellingham diagram

The Gibbs free energy is defined as

$$\Delta G^0(T) = \Delta H - \Delta S\,T, \tag{2.3.1}$$

Table 2.3: Standard Gibbs free energy of the iron oxides and the oxide substrates calculated from the NIST database [48] at room temperature.

Iron oxides	ΔG^0 (kJ/mol)	**Oxide substrates**	ΔG^0 (kJ/mol)
Fe_2O_3	-851.55	$SrTiO_3$	-1500
Fe_3O_4	-1164.21	TiO_2-terminated $SrTiO_3$ ($V_O^{\bullet\bullet}$)	-900 to -1039 [49]
FeO	-290.15	ZrO_2	-1112.1
		YSZ:ZrO_2-Y_2O_3(10 %)	-1200 [50]

where, $\Delta G^0(T)$ is the change of Gibbs free energy as a function of the temperature T, ΔH the enthalpy and ΔS the entropy changes. The Ellingham diagram represents the Gibbs free energy of the oxides as a function of the temperature. The diagram has some features which determine the reactivity of the different metal oxides. In particular, the oxide with lower Gibbs free energy in the diagram (Al_2O_3-Acceptor) will reduce an oxide whose free energy of formation is higher in the diagram (Fe_3O_4-Donor). Figure 2.6 shows exemplarily the Ellingham diagram of Fe_3O_4 and Fe_2O_3 in comparison with Al_2O_3. Hereby, Al_2O_3 serves as an example for a simple oxide to understand the general concepts before discussing the complex oxide in the next section. As the Al_2O_3 line falls below both the Fe_3O_4 and Fe_2O_3 lines, the oxygen ion migration direction across the interfaces points towards the Al_2O_3. Thus, Al_2O_3 can reduce Fe_3O_4 and Fe_2O_3. Therefore, thermodynamics is the key to understanding the growth mechanism of the iron oxides films and their chemical interactions on the oxide substrates. On the other hand, the kinetics (time scale) of the transitions may carry important energetic information, that, we do not consider in this thesis.

2.3.2 $SrTiO_3$ surface terminations and Gibbs free energy

In the previous section, we discussed the Ellingham diagram and the redox reactions between the iron oxides and a simple oxide like Al_2O_3. However, the thermodynamics and thus the redox reaction change with complex oxides. For example, surface termination, oxygen vacancies, and doping concentration affect the Gibbs free energy. In this study, we chose two complex oxide substrates $SrTiO_3$ and YSZ, which are different in the oxygen diffusivity or Gibbs free energy of their surfaces.

First, the Gibbs free energy of $SrTiO_3$ equals -1500 kJ/mol. However, the Gibbs free energy of TiO_2-terminated $SrTiO_3$ differs from the SrO-terminated $SrTiO_3$ as well as the bulk $SrTiO_3$. Furthermore, the oxygen vacancies $V_O^{\bullet\bullet}$ perturb the Gibbs free energy of TiO_2-terminated $SrTiO_3$ by 461 kJ/mol to 600 kJ/mol [49]. This means that the Gibbs formation energy is strongly changing to about -900 kJ/mol for the TiO_2-terminated $SrTiO_3$. The creation of oxygen vacancies can be supported by the growth conditions. Also, the chemical etching, which is used to produce TiO_2 terminations, can introduce oxygen vacancies [51]. The created oxygen vacancies indeed perturb the Gibbs free energy and lead to the possible reduction of the $SrTiO_3$ by Fe_3O_4 films (oxygen migration direction towards Fe_3O_4) as we will discuss in Chapter 5.

Second, the Gibbs free energy ΔG_F^o of the ZrO_2 equals $-1112.1\,\mathrm{kJ/mol}$. However, the Gibbs free energy ΔG_F^o of YSZ with a Y_2O_3 doping level of 10 % equals $-1200\,\mathrm{kJ/mol}$. This again means that the doping level changes the Gibbs free energy. In Table 2.3, we introduce some values of the Gibbs free energy at standard conditions for the iron oxides and oxide substrates.

CHAPTER 3

Experimental Methods

This study focuses on investigating, tuning and controlling the electronic and magnetic properties of Fe_3O_4/oxide-substrates interfaces. Therefore, this chapter briefly introduces the different techniques required to achieve our goals.

3.1 Pulsed laser deposition (PLD)

Pulsed laser deposition (PLD) is a commonly used technique for growing crystalline oxides thin films. In the PLD technique, high-power laser pulses are focused on a target producing neutral and ionized species that are deposited onto a substrate to form a thin film, as shown in Figure 3.1. The adjustment of the deposition parameters is crucial for the growth of high-quality stoichiometric films [52].

The PLD process steps employed in this thesis can be described as follows:

(1) A 50 W KrF excimer laser with a pulse width of 25 ns and a wavelength of $\lambda = 248\,\mathrm{nm}$ is used[1]. The strong absorption of ultraviolet nanosecond pulses by the target material over a small volume is required for the creation of the plasma plume. The laser fluence F, which is calculated by the energy of laser pulses and the size of the laser spot on the target, is essential for the ablation process. The laser fluence and the pulse repetition rate can be adjusted between $F = 1{-}3\,\mathrm{J/cm^2}$ and $f = 1 - 50\,\mathrm{Hz}$, respectively.

---

[1] We thank R. Dittmann (PGI-7) for providing us the PLD setup.

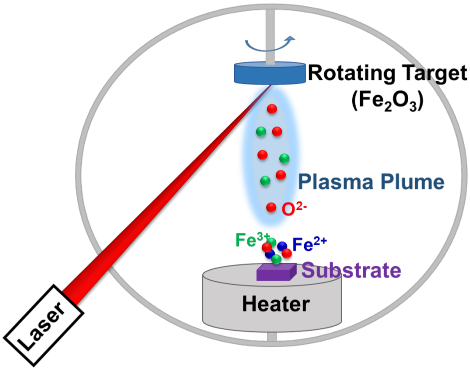

Figure 3.1: Schematic illustration of the PLD setup. Laser pulses are directed on a rotating target of Fe_2O_3 material that generates a plasma plume. The ablated material, which consists of neutral and ionized species, interacts with the background pressure and then condenses on a heated substrate forming a film.

(2) The ablated material consists of the cations of the target (Fe_2O_3 with purity 99.9 % - Praxair). These neutral and ionized species interact with the background oxygen pressure inside the chamber and form the desired film stoichiometry. This film does not necessarily have the same phase as the target. In this study, oxygen gas is supplied in a chamber with a base pressure of 1×10^{-7}mbar.

(3) The interacting plume is directed towards a substrate, which is mounted at a distance of 50 mm away from the target. The substrate is mounted on a heater, with a maximum operating temperature of 850 °C, required to introduce sufficient energy for the adatoms to diffuse and arrange themselves to form the desired crystalline film. In Chapter 4, the PLD process is investigated in detail.

3.2 Characterization techniques

The physical and chemical properties of the oxide films and substrates are studied by several characterization techniques. Before the deposition, it is necessary to confirm the formation of a TiO_2-terminated $SrTiO_3$ substrate surface, which is validated by atomic force microscopy (AFM) by characterizing the trace morphology. Furthermore, the surface morphology of the Fe_3O_4 films is detected by either AFM or X-ray reflectivity (XRR). XRR is also used to define the thickness of the films. In a next step, in order to investigate the crystal structure and the epitaxial growth, X-ray diffraction (XRD) is conducted. Finally, the magnetic properties, in particular, the Verwey temperature which is indicative for the Fe_3O_4 phase, are measured by vibrating sample magnetometry (VSM).

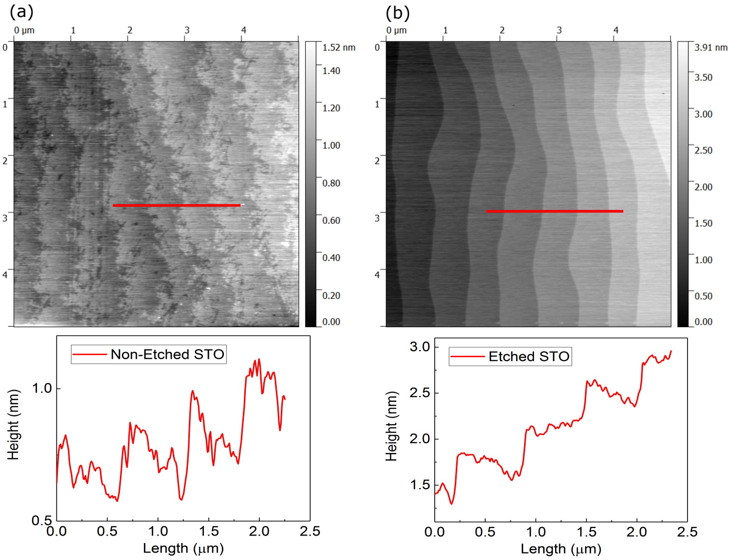

Figure 3.2: AFM morphology measurements confirm the formation of TiO_2-terminated $SrTiO_3$ substrate surfaces (the TiO_2-terminated results in the traces patterns): (a) before and (b) after the chemical etching and annealing procedures (Appendix A.4).

3.2.1 Atomic force microscopy (AFM)

The surface morphology of the films and substrates is investigated by an Asylum Research Cypher AFM. The measurements are done in the AC (tapping) mode in air. A tip of the type "Arrow NCR" is used.

In tapping mode, the cantilever oscillates with a frequency close to the resonance. In our experiment, the cantilever is set to a free amplitude of 1 V. The changes in the surface morphology cause variation of the amplitude of the cantilever oscillation, which is directly translated by the deviation of the reflected laser beam from the cantilever. The scan size is a square of 5 µm × 5 µm, which is scanned with a rate of 5 Hz.

The AFM provides a three-dimensional surface morphology with a subnanometer resolution, which is sufficient to monitor the step terrace structure of TiO_2-terminated $SrTiO_3$ substrates as it is depicted in Figure 3.2. The surface roughness can be calculated by the root mean square (RMS) of the AFM image, which is determined using the Gwyddion software [53].

3.2.2 X-ray diffraction (XRD) and reflectivity (XRR)

The crystal structure, the film crystallinity, the lattice constant, the film thickness and the surface and interface roughness are characterized by X-ray diffraction (XRD) and X-ray reflectivity (XRR). The measurements in this thesis are performed using a four-cycle Philips MRD Pro diffractometer in the Bragg-Brentano geometry[2]. The setup has a Cu-K_α X-ray tube, which provides wavelengths of $\lambda_{K_{\alpha 1}} = 1.540\,\text{Å}$ and $\lambda_{K_{\alpha 2}} = 1.544\,\text{Å}$.

XRD

In XRD, an X-ray beam is traveling through a crystal solid and interacts with the electronic structure of the lattice and is scattered. Because of the periodicity of the crystal lattice, the scattered X-rays interfere with each other. Constructive interference is allowed if Bragg's condition is fulfilled

$$n\lambda = 2d_{hkl}sin\theta \tag{3.2.1}$$

where d_{hkl} is the spacing between the crystal planes (hkl).

The in-plane a_{ip} and out-of-plane lattice constant c_{oop} for a cubic system, if the condition $a_{ip} = c_{oop}$ is fulfilled, can be calculated by

$$d_{hkl} = \frac{c_{oop}}{\sqrt{h^2 + k^2 + l^2}} \tag{3.2.2}$$

The out-of-plane lattice constant is an indicator for the crystallinity and facilitates quantitative measurements of the strain provided by the substrate. The strain strongly affects the magnetic and electric properties of the films. For heteroepitaxial growth, if the films have lattice mismatch with the substrates, they are grown within three possible scenarios: (1) fully strained, i.e. compressive or tensile, (2) fully relaxed and (3) partially strained. If the in-plane lattice constant of the films attempts to be equal to the substrate lattice constant – the unit cell size is preserved – consequently the out-of-plane lattice constant deviates from that of the bulk as we will discuss in detail later in Chapter 4.

XRR

In this work, X-ray reflectivity (XRR) is used to measure the thickness of the film and the roughness of the surfaces and interfaces. If the incident X-ray has an angle smaller than the critical angle, it gets reflected from the surface. With increasing the angle, the X-ray enters the surface and reflects from the interfaces. The reflected beams interfere and produce interference oscillations (Kiessig fringes [54]), which carry the information about the thickness and intralayer roughness.

The X-ray reflectivity (XRR) is carried out with a small incident angle, $2\theta = 0.1°\text{-}5°$. The film thickness d can be determined by

$$d \approx \frac{\lambda}{2\Delta\theta}, \tag{3.2.3}$$

where $\Delta\theta$ is the angle between two adjacent fringes. In this study, the thickness and the roughness of both surfaces and interfaces are calculated by fitting the experimental data using the software X'Pert Reflectivity. The software makes use of the Parratt formalism [55].

---

[2] We thank Peter-Grünberg-Institut: Electronics Materials (PGI-7) for providing us measurement time on the Philips XPert MRD diffractometer.

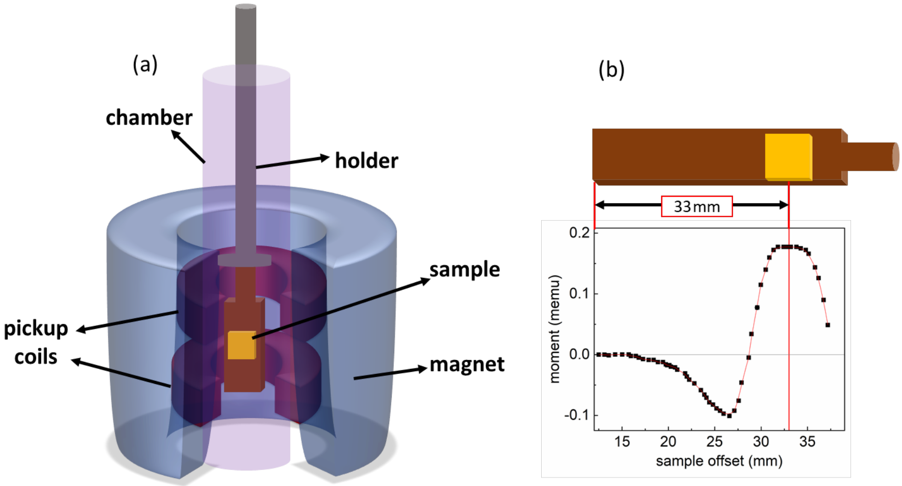

Figure 3.3: (a) Vibrating sample magnetometer schematics. (b) Sample offset determination, i.e. centering the sample to the coils, for a sample with magnetic moment 2×10^{-4} emu by performing the touchdown operation.

3.2.3 Vibrating sample magnetometer (VSM)

The magnetic properties of the samples have been measured using a vibrating sample magnetometer (VSM) (Figure 3.3). The VSM used in this thesis is a module of the Quantum Design Dynacool physical property measurement system (PPMS)[3]. It has a sensitivity of 3×10^{-7} emu which is one order of magnitude smaller than the magnetic moment of 1 u.c. of Fe_3O_4 (2.768×10^{-6} emu). In the VSM, the sample is vibrating sinusoidally. One data point is measured with an amplitude of 2 mm and frequency of 40 Hz within 2 s in a uniform in-plane magnetic field. The magnetic field is aligned along the [100]-axis of the sample. An induced voltage is generated. The sample is positioned at the vertical center of a pickup coil where the voltage is induced and then amplified. The PPMS allows a well-controlled sample environment in the temperature range from 1.9 K to 400 K and the magnetic field range from -9 T to 9 T.

The VSM allows us to measure the magnetic moment of the whole sample, which means that both the film and the substrate contribute. The diamagnetic contribution of the STO substrate can be subtracted from the raw signal to extract the magnetic moment of the film. Ideally, each substrate should be measured first before the growth, however, this is not applicable. If we assume that the magnetization of Fe_3O_4 is saturated below 3 T, the magnetic behavior at high magnetic fields is dominated by the substrate. Thus, linear fitting is applied to the signal at the high fields ranging from 3 T to 5 T and the resulting line is subtracted as depicted in Figure 3.4.

---

[3] We thank O. Petracic (Jülich Centre for Neutron Science (JCNS-2 / PGI-4)) for providing us measurement time on the Quantum Design Dynacool PPMS.

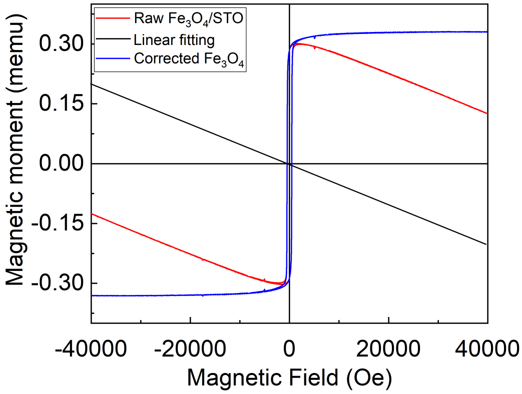

Figure 3.4: Example for a hysteresis loop measured at 100 K of 38 nm thick Fe_3O_4/STO (red), linear fitting represent the diamagnetic contribution of the $SrTiO_3$ substrate (black) and the calculated loop of the Fe_3O_4 film (blue).

3.3 Synchrotron-based X-ray spectroscopy

X-ray photons interact with material via either photoelectric effect or (in)elastic scattering. The photoelectric effect describes the absorption process of photons by the core level and valence electrons. According to the energy of the photons, the electrons are emitted into the continuum (X-ray photoelectron spectroscopy (XPS)) or excited into higher empty states (X-ray absorption spectroscopy(XAS)). Studying the XPS and XAS are powerful techniques to investigate the element-specific electronic and magnetic structure of the heterostructures.

In this thesis, synchrotron radiation is needed for both XAS and XPS. For XAS and X-ray magnetic circular dichroism (XMCD), a tunable and switchable-polarization soft X-ray source is needed, which is only provided by a synchrotron facility. For XPS, depth profiling and element-selective chemical structure of the films and buried interfaces can only be studied by hard X-rays, which is also mostly provided by synchrotron facilities. In this case, the measurement technique is known as hard X-ray photoelectron spectroscopy (HAXPES). Before describing the experimental details about the synchrotron sources, some theoretical aspects will be discussed in the following sections.

3.3.1 Fermi's golden rule

In the photoemission process, an electron in an initial state $|i\rangle$ is excited to a final state $|f\rangle$ via photon absorption. Assuming that the interactions among electrons can be neglected, the problem can be simplified to single electron-photon interactions. The photon causes a weak perturbation to the system. The transition probability per unit time W_{fi}, which indicates the probability that the transition from the initial to the final state will happen, is given by Fermi's Golden Rule [56]:

$$W_{fi} = \frac{2\pi}{\hbar} |\langle f|\hat{H}|i\rangle|^2 \delta(E_f - E_i - h\nu) \tag{3.3.1}$$

where, E_f is the final state energy, E_i is the initial state energy and $h\nu$ is the photon energy. The delta function $\delta(E_f - E_i - h\nu)$ ensures the conservation of the energy during the transition. The most important term in this equation is $\langle f|\hat{H}|i\rangle$, which is known as the matrix element M_{fi}. The matrix element includes information about the photoexcitation process. It depends on the final and initial state with the effect of the perturbation operator $\hat{H}$.

Dipole selection rules

In order to calculate the matrix element M_{fi}, the initial $|i\rangle$ and the final states $\langle f|$ have to be known. In the X-ray photoelectron spectroscopy, the final state $\langle f|$ can be described by a free electron. In X-ray absorption spectroscopy, the matrix element M_{fi} for some specific combinations of the initial $|i\rangle$ and final states $\langle f|$ is zero, which means that these transitions are forbidden. The states fulfilling the *dipole selection rules* [57] contribute to the spectrum. The dipole selection rules are given by

$$\Delta J = 0, \pm 1, \tag{3.3.2}$$

$$\Delta M_J = 0, \pm 1, \tag{3.3.3}$$

$$\Delta S = 0 \tag{3.3.4}$$

where, J is the total angular momentum quantum number, M_J is the projection of the total angular momentum and S is the spin quantum number. The selection rules explain, for example, that the transitions L-edge (2p → 3d) are allowed.

3.3.2 Three-step model of photoemission

One approximation for the photoemission process is the *three-step model* [58]. In this model, the emission process is divided into three steps as depicted in Figure 3.5:

(1) **Optical excitation:**

If a photon with energy $E_\gamma = h\nu$ is absorbed by an atom, the electron is excited from an initial state with energy E_i to a final state with energy E_f.

$$E_\gamma = h\nu = E_f - E_i \tag{3.3.5}$$

The transition probability is given by Fermi's golden rule in Equation 3.3.1.

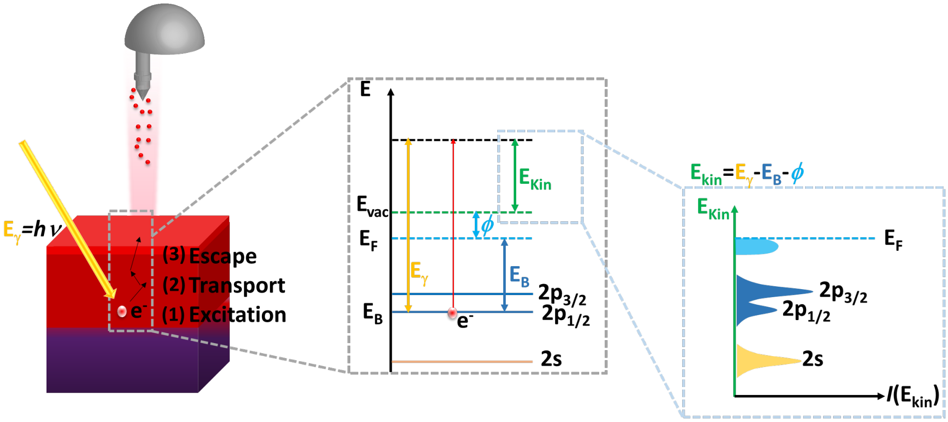

Figure 3.5: Schematics summarizing the photoemission process: (1) Optical excitation where a photon with energy $E_\gamma = h\nu$ is absorbed by an electron which is excited into an unoccupied state, (2) Transport of the electron through the solid where the electron undergoes elastic and inelastic scattering, and (3) Escape into the vacuum after overcoming the surface potential. The emitted photoelectron kinetic energy reflects the crystal electronic states.

(2) **Transport of the electron through the solid:**

After exciting the electron from the core level to a final state above the Fermi level, the excited electron travels through the crystal towards the surface. During the electron trip through the solid, it undergoes several elastic and inelastic scattering processes. The elastic scattering causes the deflection of the electron without losing its energy. On the other hand, the inelastic scattering leads to a loss in its kinetic energy, consequently, losing the information about the core level binding energy as will be explained in Section 3.3.3.

(3) **Escape into the vacuum:**

The electron needs additional energy to overcome the surface potential energy (the work function ϕ) and travel into the vacuum. Thus, the escaped electron has a kinetic energy E_{Kin} given by

$$E_{Kin} = E_\gamma - E_B - \phi, \tag{3.3.6}$$

where E_B is the binding energy of the core level.

3.3.3 Information depth

As described in Section 3.3.2, electrons may undergo inelastic scattering on their way through the solid, causing loss of their energy, thus, losing the information about the

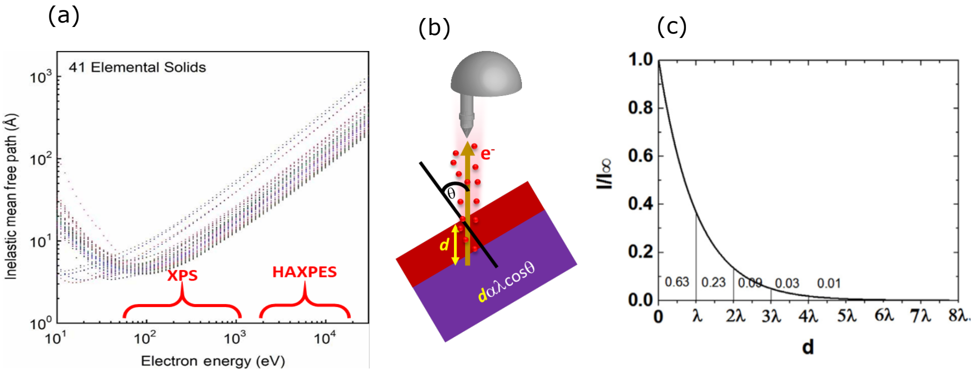

Figure 3.6: (a) The inelastic mean free path as a function of the kinetic energy of the electron for different elemental solids from the low atomic number Z Li to the high Z Bi [59]. (b) Schematic depicts the variation of information depth d depending on the experimental geometry. (c) The relative intensities of the escaping electrons as a function of the depth from the surface into the solid [60].

binding energy of the core level. In this case, the photoelectrons contribute to the spectral background instead of the core level peak. Therefore, it is crucial to identify the distance, which an electron can travel through the material without inelastic scattering, defining the inelastic mean free path λ_{IMFP}.

The inelastic mean free path λ_{IMFP} depends on the elemental solids and the kinetic energy of the electrons as shown in Figure 3.6 (a). The inelastic mean free path has a similar behavior for different chosen materials, which is called *universal curve*. One can estimate that the inelastic mean free path depends mainly on the electron energy. In the HAXPES range, the λ_{IMFP} increases with increasing energy and is at least one order of magnitude larger than the λ_{IMFP} of XPS.

Although the inelastic mean free path is independent of the experimental geometry, i.e. the angle between the detector and the surface normal θ, the maximum information depth strongly depends on the angle θ. The intensity of the photoelectrons I, which originates from a certain depth d, can be determined by the Beer-Lambert law

$$I = I_{\infty} \cdot exp\left(-\frac{d}{\lambda cos\theta}\right) \quad . \tag{3.3.7}$$

Thus, the information depth d is about three times the inelastic mean free path, 3λ. As the contribution from $d > 3\lambda$ is less than 9 %, it approaches the noise level as depicted in Figure 3.6 (c).

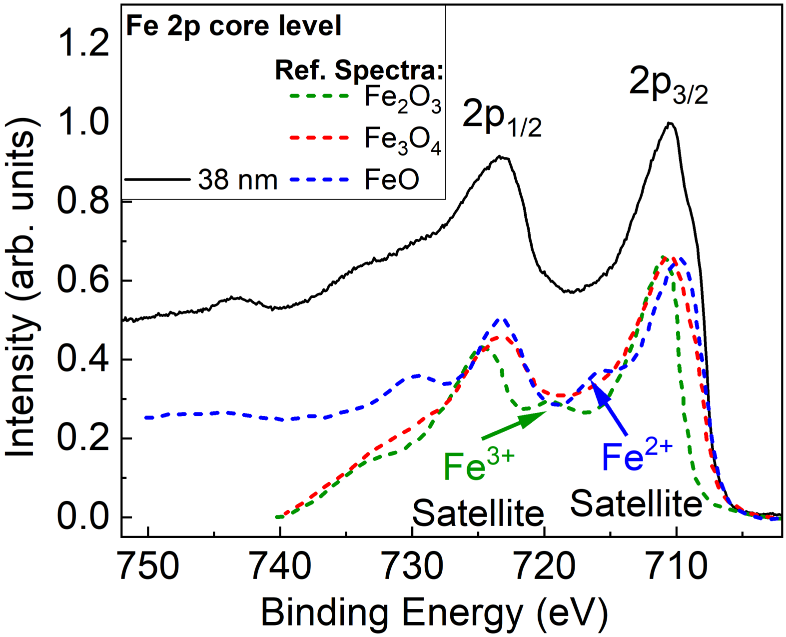

Figure 3.7: Experimental HAXPES spectra for Fe 2p core level of the 38 nm Fe_3O_4 on $SrTiO_3$ (001) recorded using a photon energy of $h\nu = 6\,keV$ and reference spectra of different iron oxides Fe_2O_3, Fe_3O_4 and FeO [61, 62].

3.3.4 Photoemission spectral features

The excitation of electrons from the core level contributes to the photoemission spectra. However, there are additional features that cannot be explained by only the core level excitation and neglecting the interaction between the particles. Several spectral features relevant to this study will be explained in the following sections.

Chemical shifts

In this study, we are focusing on the iron oxide phases. They have different chemical structures; i.e. Fe_3O_4 has mixed-valence states of both Fe^{2+} and Fe^{3+}, Fe_2O_3 has only a contribution from Fe^{3+} and, finally, FeO has a Fe^{2+} valance state. Each of the iron oxide phases has a particular atomic configuration, for example, the ground state configuration of Fe metal is $4s^2\ 3d^6$, but for Fe^{3+} and Fe^{2+}, it is $4s^0\ 3d^5$ and $4s^0\ 3d^6$, respectively. The change of the chemical valency is translated into a change of the binding energy and causes a shift in the core level peaks. Figure 3.7 shows the experimental HAXPES spectrum of Fe 2p core level of a Fe_3O_4 thin film in comparison to reference spectra of the different iron oxide phases. A clear shift in the binding energies between the different chemical phases is shown in the reference spectra. The Fe $2p_{3/2}$ core-level of FeO with Fe^{2+} valence state is located at an energy of 709.8 eV. In comparison, the Fe $2p_{3/2}$ of Fe_2O_3 with Fe^{3+} valence state is located at an energy of 710.8 eV. The chemical shift between the two peaks is $\Delta E = 1\,\mathrm{eV}$. Fe_3O_4 has a mixed-valence state of Fe^{2+} and Fe^{3+}. Therefore, the Fe $2p_{3/2}$ core level consists of a peak attributed to the Fe^{3+} and a shoulder attributed to Fe^{2+}. Thus, the shifts of the binding energies enable us to identify the different iron oxides by HAXPES spectra.

Spin-orbit splitting

The electron has an orbital angular momentum $L = 0,1,2....$ (s, p, d,....), in addition to a spin angular momentum $S = \pm 1/2$ (spin up or spin down). The coupling between the spin and orbital moment, the spin-orbit interaction, causes additional splitting of the core level binding energies. It is represented by the total angular momentum $J_\pm = L \pm S$. Thus, the core level is splitting into two levels with different binding energy (except for the s level where $L = 0$). For example, the spectrum of the 2p core level consists of two peaks ($2p_{1/2}$ and $2p_{3/2}$). The intensity ratio R between the two peaks can be determined by the branching ratio

$$R = \frac{2J_- + 1}{2J_+ + 1} \tag{3.3.8}$$

For example, the relative intensities between the two peaks of the 2p core level ($2p_{1/2}$: $2p_{3/2}$) equal 1:2. As depicted in Figure 3.7, the HAXPES spectrum of the Fe 2p core level reveals two main peaks, $2p_{1/2}$ and $2p_{3/2}$.

Multiplet splitting

After the photoexcitation, an unpaired core electron can couple to the spin of the valence shell (d-electrons for iron oxides). This interaction causes additional splitting (or broadening) in the main peaks – Fe $2p_{3/2}$ and $2p_{1/2}$ – as shown in Figure 3.7. For example, the Fe $2p_{3/2}$ of the Fe_2O_3 phase consists of four peaks [63, 64]. To explain this phenomenon, we can divide the problem into two stages: (1) a core-electron of Fe_2O_3, which has the ground state of $2p^6 3d^5$, and gets excited to an excited state of $\mathbf{2p}^5 3d^5$ configuration. (2) The unpaired core-electron p^5 (excited state) is coupled to the d^5 (ground state), resulting in the splittings observed in the main peak.

Satellite peaks

Another spectral feature, which cannot be explained by the core electron excitation, is the appearance of satellite peaks. In this thesis, satellite peaks are an important feature for characterizing the different iron oxide phases. As it is shown in Figure 3.7, the satellite peaks of the iron oxide phases are located at different binding energies. The binding energies of the satellite peaks are 715.5 eV and 719 eV for the FeO and Fe_2O_3 phases, respectively. For Fe_3O_4, which has a mixed oxidation state of Fe^{2+} and Fe^{3+}, both satellites peaks from both states merge and thus disappear [61, 62].

The satellites of iron oxides are known as "*shakeup*" satellites. Much of the literature attempts to explain the origin of the satellites. The satellites could be interpreted by the sudden approximation where the photoionization process causes a sudden perturbation, leading to an excited state, which may lead to shakeup transitions. The valence electrons are excited to a higher unoccupied state. Consequently, the kinetic energy of the photoelectron is reduced and causes the satellites at higher binding energies [65]. In other words, the coupling between the core hole and the excited states explains the presence of the satellites [63, 64]. In literature, the origin of the satellites may be attributed to the charge-transfer from the ligand (oxygen) to the 3d-metal (iron), the 3d electrons correlation and the Fe 3d - O 2p hybridization [61, 66].

Charging effect

The creation of photoelectrons during the photoionization process leads to a positively charged sample, decreasing the kinetic energy of the core level electrons. In this study, the charging effect is overcome by grounding the samples and using conductive substrates (Nb:SrTiO$_3$) or compensating the surface charge by connecting the surface to the conductive grounded electrode.

3.3.5 Hard X-ray photoelectron spectroscopy (HAXPES)

Hard X-ray photoelectron spectroscopy (HAXPES) is a powerful *element selective* technique to identify the chemical and electronic structure of *buried* interfaces due to its large bulk sensitivity. The X-ray energy used to irradiate the samples is in the range of $E_\gamma = 2\text{-}10\,\mathrm{keV}$. Referring to Section 3.3.3, one can understand that the probing depth of HAXPES is ranging from 10 nm up to 30 nm according to the kinetic energy of the photoelectron (or the photon energy E_γ). This is considered as one of the advantages of the HAXPES technique in comparison to the *surface*-sensitive X-ray photoemission spectroscopy (XPS). In this work, the experiments have been performed at two different beamlines:

(1) P09, PETRA III, Hamburg, Germany

At PETRA III, P09 beamline (since June 2018 P022), we conducted HAXPES with an energy of 5945.56 eV at room temperature in normal emission geometry with an angle $\theta = 5°$ and grazing emission 60°. The energy resolution of this experiment is $\Delta E = 100\,\mathrm{meV}$. More details about the beamline can be found in [67, 68]

(2) HIKE, KMC-1, BESSY II, Berlin, Germany

In BESSY II, HIKE beamline, the HAXPES experiment is conducted using a photon energy of 4 keV. One of the advantages of this beamline is that an annealing option simultaneously with HAXPES is available with temperatures up to 700 °C. In this beamline, the hard X-ray beam is aligned at 3° grazing angle with respect to the sample. The detector is aligned normal to the sample surface. In our experiment, the samples are adjusted to an angle of 10° to the normal of the sample surface. The energy resolution of the experiment is $\Delta E = 200\,\mathrm{meV}$ [69, 70].

3.3.6 X-ray absorption spectroscopy (XAS)

If a monochromatic X-ray beam with energy $h\nu$ irradiates a sample of thickness d, the transmitted beam intensity $I(h\nu)$ is attenuated according to the Beer-Lambert law

$$I(d) = I_0 \cdot exp(-\mu(h\nu)d) \tag{3.3.9}$$

where, $I_0(h\nu)$ is the incident X-ray intensity and $\mu(h\nu)$ is the linear absorption coefficient. Two important facts can be drawn from this equation: (1) the absorption coefficient μ depends on the photon energy $h\nu$. Generally, it decreases with increasing the energy, except for some particular wavelengths where μ increases abruptly, i.e. the absorption edges. (2) The transmitted intensity $I(h\nu)$ decreases exponentially with the thickness d below the detection limit for thick samples. Therefore, for thick samples (the thin films and substrates), the detection of the X-ray absorption coefficient is only possible using secondary processes, i.e. the sample fluorescence or the emission of secondary electrons.

In case of fluorescence yield detection mode, the absorbed X-ray causes the transitions of electrons from their initial states to excited states for a temporary time. The excited electrons then fall back into their ground states and cause the reemission of photons. In this experiment, the intensity of the fluorescence photons is detected with a photodiode placed close to the sample. This measurement mode is called Fluorescence Yield (FY). This method is bulk sensitive since the fluorescence photons have an attenuation length of several µm. Despite its bulk sensitivity, one of the disadvantages of this mode is the self-absorption or saturation effect. For thick films, the self-absorption will cause a reduction in the heights of the peaks, consequently, a blurring of the spectral information and increasing of the noise will be prominent.

In the electron yield detection mode, one collects the secondary and Auger electrons, which escape from the sample as the result of the absorption of X-ray photons. The Auger electrons travel through the sample to the surface then escape to the continuum. As they move to the surface, electrons may scatter with other electrons and transfer their energies thus causing the formation of secondary electrons. This results in an electron cascade. The escaped electrons leave positive charges in the sample, which are compensated by grounding the sample through a sensitive current amplifier. The measured sample current is then directly related to the absorption coefficient $\mu(h\nu)$. Since all the electrons that emerge from the sample surface are detected, this mode is called Total Electron Yield (TEY). One of the disadvantages of this mode is that the electrons interact strongly with the solid. Therefore, only the electrons which originate close to the surface (several nm) can escape to the vacuum. Thus, the TEY is a surface-sensitive measurement mode.

3.3.7 X-ray magnetic circular dichroism (XMCD)

X-ray absorption spectroscopy can probe the electronic, magnetic and ferroelectric properties of a solid. By tuning the X-ray polarization of the incident beam, the magnetic moment can be measured by the X-ray magnetic circular dichroism (XMCD) technique and ferroelectricity can be probed by the X-ray linear dichroism. In the following, we will focus on the XMCD, which was employed in this thesis.

The absorption coefficient $\mu(h\nu)$ is strongly affected by the X-ray energy. However, the X-ray energy is not the only factor that affects $\mu(h\nu)$. The X-ray absorption spectra of ferromagnetic materials depend on the external magnetic field (to saturate the magnetization), the X-ray polarization and the experimental geometry (sample orientation). The sample geometry is important in the X-ray magnetic circular dichroism. For example, if the sample is magnetically anisotropic, the XMCD spectra recorded at different orientations will have different intensities depending on whether the measurements are performed parallel to the magnetic easy axis or perpendicular to it. The dichroic signal can be obtained by either applying right and left circular polarized light or applying a magnetic field with opposite polarities.

We can explain the origin of XMCD using the two-step model [32] (Figure 3.8 (a)). In the first step, the incident circular polarized X-rays transfer their angular momentum to the excited electrons, which are spin-polarized. Thus, the X-rays with positive (negative) helicity excite electrons with spin up (down), respectively. In this step, the spin-orbit coupling of the core level plays an important role. For example, the L_3 edge (transition from the core level $2p_{3/2}$), and the L_2 edge ($2p_{1/2}$) have opposite spin polarization because they have opposite spin-orbit coupling (l+s and l-s, respectively). In the second step, the exchange splitting of the valence shell is the major parameter, i.e. their occupation for the spin up and down electrons are unequal. According to Fermi's golden rule and the selection rules discussed in Section 3.3.1, the polarized electrons can only occupy states with the same spin orientation. Therefore, the valence shell acts as a detector for the spin and orbital momentum of the photoelectron.

In order to extract the XMCD spectra from the XAS spectra, two XAS spectra of the sample are recorded using either (1) positive and negative helicity X-rays or (2) magnetic field with reversed magnetization directions. The XMCD spectra are given by the difference between the two absorption spectra.

$$\mu_{XMCD}(h\nu) = \mu^{-}(h\nu) - \mu^{+}(h\nu), \tag{3.3.10}$$

where, μ^{+} and μ^{-} represent the absorption spectra that are recorded using inverse magnetization or polarization. The use of either reversed polarized light or magnetization direction results in the same spectra, because the dichroic spectrum depends on the alignment between the polarization vector of the incident light and the magnetization vector of the sample.

The sum rules

The spin magnetic moment m_{Spin} and the orbital magnetic moment m_{Orb} can be calculated by applying the sum rules [71, 72]

$$m_{Spin} + 7 < T_z >= -\frac{3p - 2q}{r} N_h, \tag{3.3.11}$$

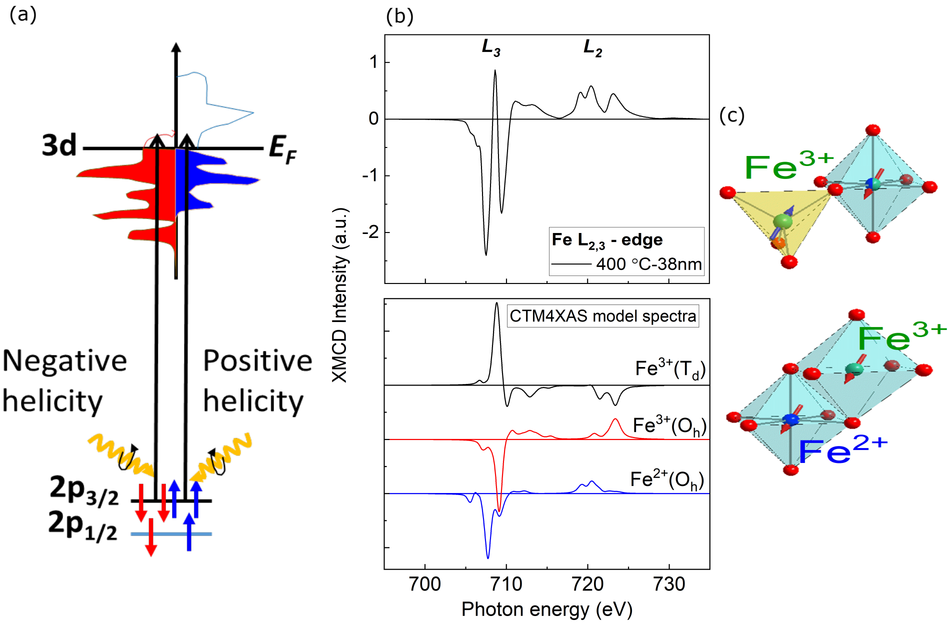

Figure 3.8: (a) Schematics depicting the XMCD at the $L_{2,3}$ edge. Using two reversed right (left) polarized X-rays, spin-polarized photoelectrons are excited to the 3d bands which work as a detector because of the exchange splitting [32]. (b) The XMCD spectrum of Fe $L_{2,3}$ edge of Fe_3O_4 films (38 nm thick) grown at temperature 400 °C in comparison to model spectra calculated using CTM4XAS software for Fe^{3+} and Fe^{2+} on different sites (tetrahedral (T_d) and octahedral (O_h)). (c) Schematics presenting the antiferromagnetic coupling between the Fe cations in the tetrahedral and octahedral sites and the ferromagnetic coupling between the Fe cations in the octahedral sites of Fe_3O_4. Thus, the different coupling mechanisms between the different sites are responsible for the characteristic "W shape" of the XMCD spectra for the Fe L_3 edge.

$$m_{Orb} = -\frac{2q}{3r} N_h, \tag{3.3.12}$$

where N_h is the number of empty states per formula unit (for magnetite Fe_3O_4 equals 13.5 [73]), and T_z indicates the magnetic dipole moment operator that can be neglected to the first order for cubic systems [74]. The values of p and q are calculated from the XMCD integration

$$p = \int_{L_3} (\mu^+ - \mu^-) d\omega \quad q = \int_{L_{3,2}} (\mu^+ - \mu^-) d\omega, \tag{3.3.13}$$

while r is calculated by the XAS integration

$$r = \frac{1}{2} \int_{L_{3,2}} (\mu^+ + \mu^-) d\omega. \tag{3.3.14}$$

XMCD of Fe_3O_4 - Fe $L_{3,2}$ edge

One of the advantages of the XMCD technique is the sensitivity to the element-specific magnetic moment. Thus, the different cation distributions and stoichiometry of the complex systems can be investigated. In this thesis, we are interested in Fe_3O_4 which has a complex magnetic structure. Fe cations with different valences (Fe^{2+} and Fe^{3+}) occupy different lattice sites. In Figure 3.8 (b), XMCD spectrum of a 38 nm thick Fe_3O_4 film is compared to a model spectra calculated using CTM4XAS 5.5 software [75]. Fe^{3+} cations occupying the tetrahedral sites are antiferromagnetically coupled to the Fe^{2+} and Fe^{3+} cations in the octahedral sites (Figure 3.8 (c)). Moreover, the Fe^{2+} and Fe^{3+} cations in the octahedral sites are ferromagnetically coupled. Thus, the L_3 edge has the well-known "W shape", which characterizes the magnetite Fe_3O_4 with positive peak attributed to the $Fe^{3+}_{T_d}$ and two negative peaks attributed to the $Fe^{2+}_{O_h}$ and $Fe^{3+}_{O_h}$. For this reason, the XMCD is a powerful technique not only to calculate the elemental spin and orbital magnetic moment but also to detect the chemical stoichiometry of Fe_3O_4 and differentiate between the Fe_3O_4 phase and the spinel ferrimagnetic γ-Fe_2O_3 phase.

I10, The Diamond Light Source, Didcot, UK

X-ray absorption spectra (XAS) were recorded at the high field magnet system end-station of the I10, the Beamline for Advanced Dichroism Experiments (BLADE) at the DIAMOND Light Source, Didcot. The station can provide magnetic fields in the range of $B = \pm 14$ T and temperatures in the range of $T = 3$-420 K. The magnetic field is directed along the direction of the X-ray beam [76]. Circular polarized X-rays with energies of E = 0.4-2 keV are available. A near-grazing emission geometry $\theta = 80°$ has been used as the thin oxide films are expected to have a mostly in-plane easy axis of magnetization.

CHAPTER 4

Growth optimization of Fe_3O_4/$SrTiO_3$ heterostructures

Growing high-quality magnetite (Fe_3O_4) films on one of the bedrocks of oxide-based electronics, $SrTiO_3$ (STO) substrates, is one of the major goals of this study. Magnetite (lattice constant = 8.395 Å) has a −7.5 % compressive mismatch with respect to the $SrTiO_3$ substrate (lattice constant = 3.905 Å), which makes growing Fe_3O_4 on $SrTiO_3$ a challenge. For example, dislocations, twinning and formation of anti-phase boundaries (APBs) [45], as well as a large surface roughness [77, 78] were reported for Fe_3O_4/$SrTiO_3$ heterostructures. Also, a cationic inversion [79] and formation of polycrystalline films [80] were discussed. Moreover, the formation of undesired interfaces, e.g. the antiferromagnetic FeO phase was observed [81].

In this chapter, we will discuss the influence of the pulsed laser deposition (PLD) growth parameters, in particular, the growth temperature, on the structure and magnetic properties of Fe_3O_4/STO heterostructures. The substrate temperature is a critical growth parameter for growing magnetite thin films [82, 83]. It influences the surface morphology, the crystallinity and even the stoichiometry of the films. Most magnetic oxides are grown at high growth temperatures up to 700 °C [84], which is favorable for the crystallinity of the films. A high substrate temperature increases the surface mobility of the atoms. This results in a reduction in the surface defects and dislocations and, thus, improves the crystallinity of the grown films. However, this is not the case for Fe_3O_4 thin films as we will clarify in the following sections. In some cases, the high temperature can cause interdiffusion reactions between the substrates and the films, which affect the growth quality. Hence, it is essential to discuss the effect of the growth temperature on the different properties of the films in detail.

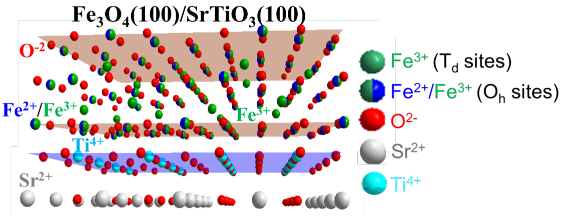

Figure 4.1: Schematic arrangement of the Fe_3O_4 (001) lattice on TiO_2-terminated Nb:$SrTiO_3$ (001).

4.1 PLD growth conditions

A series of Fe_3O_4 films were grown by PLD at different growth temperatures on conductive TiO_2-terminated 0.1 % Nb-doped $SrTiO_3$ (001) substrates (from Crystec GmbH, Berlin) as it is shown in Figure 4.1. The TiO_2-termination was achieved by a chemical etching process [1] [85]. We focus on the effect of growth temperature on the properties of the films. Therefore, we varied the growth temperature between $T_{growth} = 200\,°C$-$700\,°C$. All other PLD growth parameters were kept constant[2]. The laser frequency and the laser fluence were kept at $f = 5$ Hz and $F = 1.5\,J/cm^2$, respectively. The deposition time was chosen to be 25 min which results in a film thickness of $d = 38 \pm 2$ nm. The growth background O_2 pressure was kept at 2×10^{-6} mbar.

4.2 Surface morphology and structural characterization

One of the main challenges in the growth of the magnetite thin films is the large surface roughness [77, 78], which makes the optimization of the surface morphology crucial. Two different techniques have been used to investigate the surface properties: (1) atomic force microscopy (AFM) and (2) X-ray reflectivity (XRR). First, we discuss the effect of growth temperature on the films' surface morphology by atomic force microscopy. Furthermore, the structural properties are investigated by XRD.

4.2.1 Experimental details

The surface morphology of the films and substrates is investigated by an Asylum Research Cypher AFM. The measurements are done in the AC (tapping) mode in air. The scan size is a square of 5 µm × 5 µm with rate of 5 Hz.

The structure, thickness and surface roughness of the grown films are characterized using X-ray diffraction (XRD) and X-ray reflectivity (XRR). Both, XRR and XRD experiments

---

[1] We introduce the Nb:$SrTiO_3$ substrate surface treatment in Appendix A.4.

[2] We investigated the influence of the different growth parameters on the quality of the films, therefore, the optimum sets of the parameters have been refined depicted in Appendix A.3.

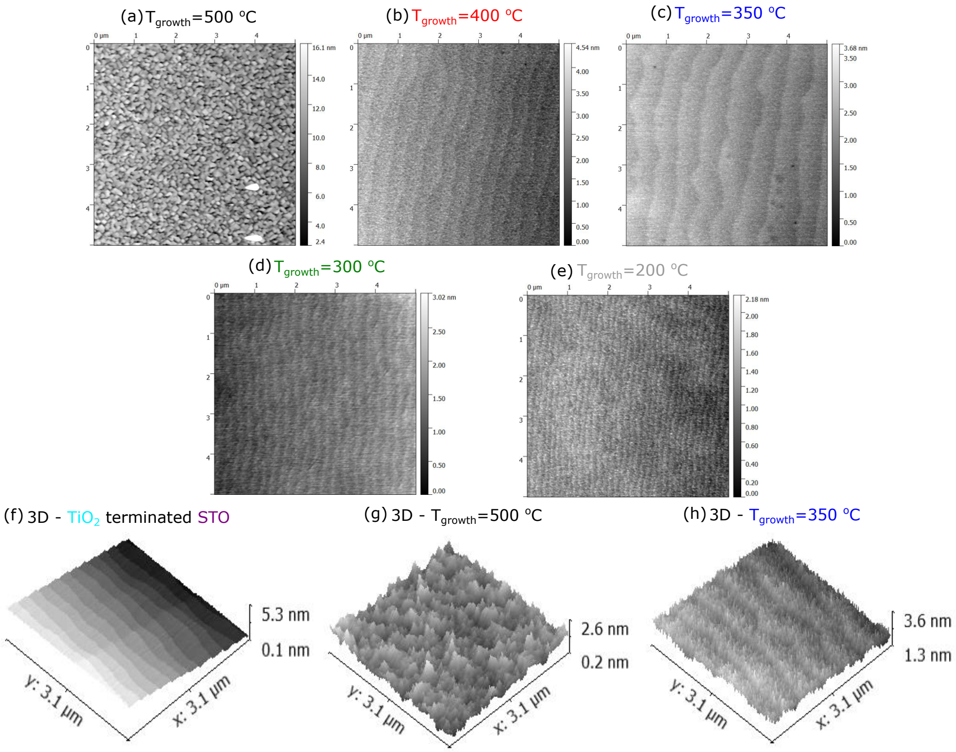

Figure 4.2: Two different sets of AFM images: The first set is 2D images of the Fe_3O_4 thin films grown at varying temperatures (a) 500 °C, (b) 400 °C, (c) 350 °C, (d) 300 °C and (e) 200 °C. The second set consists of 3D images of (f) TiO_2-terminated Nb:$SrTiO_3$ substrate, and Fe_3O_4 thin films grown at temperatures (g) 500 °C and (h) 350 °C.

were performed at room temperature on a Philips XPert MRD using Cu-K_α-radiation. In XRR, the θ-2θ scans of the films are measured in the grazing-incident mode. In XRD, out-of-plane θ-2θ scans were measured within a 2θ range from 15° to 110° with a scattering vector parallel to the surface normal.

4.2.2 AFM

AFM 5 µm × 5 µm (2D-) scans of the Fe_3O_4 films grown at growth temperatures of $T_{growth} = 500$, 400, 350, 300 and 200 °C are displayed in Figure 4.2 (a-e). Furthermore, 3D-AFM images of a $SrTiO_3$ substrate in comparison with two Fe_3O_4 films grown at $T_{growth} = 500$ and 350 °C are depicted in Figure 4.2 (f-g). For the Fe_3O_4 film grown at $T_{growth} = 500$ °C, Figure 4.2 (a) shows the absence of the terrace structure of the underlying TiO_2-terminated $SrTiO_3$. This means that the terraces structure of the substrate is

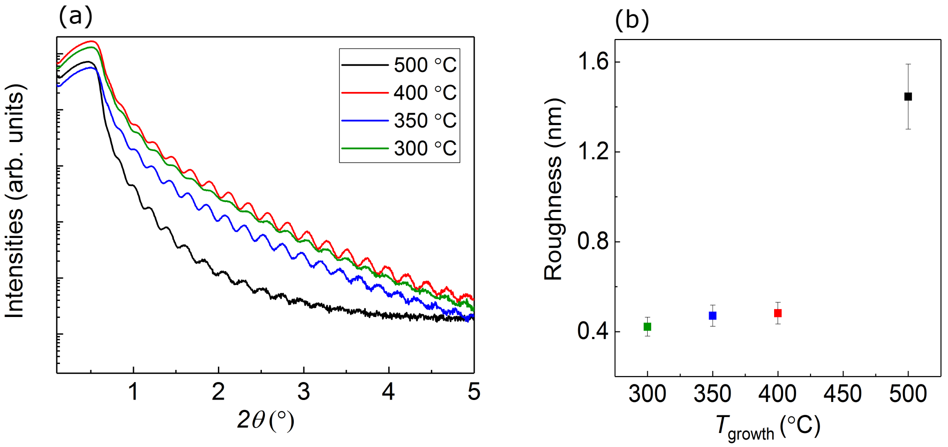

Figure 4.3: (a) X-ray reflectivity of films grown at different temperatures and (b) the calculated surface roughness of the films as a function of the growth temperature.

not adopted by the film, which indicates the undesired island growth of the Fe_3O_4 thin film on the $SrTiO_3$ substrate [86, 87]. The surface roughness can be quantified by the Root Mean Square (σ_{RMS}). It gives the mean value of the surface height variation. The σ_{RMS} is determined using the Gwyddion software [53]. The σ_{RMS} equals 1.96±0.1 nm of the Fe_3O_4 film grown at $T_{growth} = 500\,°C$. For the Fe_3O_4 films grown at temperatures below 500 °C, the terrace structure of the underlying $SrTiO_3$ substrates is transferred to the magnetite films, which indicates the layer by layer growth of the Fe_3O_4 thin film. Additionally, the surface roughness reduces to 0.26-0.19 nm for the films grown at 400-200 °C, respectively.

4.2.3 XRR

X-ray reflectivity (XRR) is used to investigate the roughness of not only the surfaces but also the interfaces. Furthermore, the thickness of the films can be investigated by XRR. Figure 4.3 (a) illustrates the θ-2θ scans in the range of $2\theta = 0.1°$-$5°$ of the Fe_3O_4 films grown at different temperatures. Above the critical angle of 0.4°, the intensity decreases exponentially. It is known that the amplitude of the exponential decay of the XRR intensity I depends on the surface roughness σ_{RMS},

$$I \propto exp(-\sigma_{RMS}^2 q_z^2) \tag{4.2.1}$$

where q_z is the scattering vector. Thus, the intensity drops faster with increasing roughness. On top of the exponential decay, oscillations (so-called Kiessig fringes) are observed in the XRR intensity for all Fe_3O_4 thin films. The Kiessig fringes carry the information about the thickness and intralayer roughness. In Figure 4.3, the diffractogram of the film grown at $T_{growth} = 500\,°\mathrm{C}$ shows a faster drop of the intensity compared to the films grown at lower temperatures. Additionally, the Kiessig fringes are disappearing at $2\theta \approx 3.5°$. The disappearance of the fringes indicates a high roughness of the surface and interface.

The measured reflectivity curves are fitted using the Parratt algorithm, implemented in the Philips X'Pert Reflectivity software. From the fits, the film thickness and the surface roughness are obtained. An example of a fitted diffractogram is depicted in Appendix A.1. The calculated surface roughness values versus growth temperature are illustrated in Figure 4.3 (b). Although the values of σ_{RMS} obtained from XRR are larger than those obtained by AFM[3], they show a similar T-dependency. The roughness of the film grown at $T_{growth} = 500\,°\mathrm{C}$ is significantly larger (1.45 ± 0.15 nm) than that of the films synthesized at $T_{growth} \leqslant 400\,°\mathrm{C}$ (below 0.5 nm). The higher roughness calculated by XRR in comparison to the values extracted from AFM is related to technique resolution, fitting procedures, and the surface and interface roughness as we explain in Appendix A.3.

In summary, using AFM and XRR we found that PLD-grown Fe_3O_4 films on $SrTiO_3$ develop a flat surface for growth temperatures $T_{growth} \leqslant 400\,°\mathrm{C}$. Next, we investigate the quality of the films in terms of crystallinity, magnetic properties and stoichiometry.

4.2.4 XRD

The crystallinity and structural properties of the Fe_3O_4/Nb:$SrTiO_3$ (001) films are investigated by X-ray diffraction (XRD). To confirm the epitaxial growth of the films, out-of-plane θ-2θ scans were measured within a 2θ range from 15° to 110°. All XRD patterns are normalized to the $SrTiO_3$ (002) reflection. The lattice constant of the inverse spinel Fe_3O_4 is 8.395 Å, which is more than twice the lattice constant of $SrTiO_3$ (3.905 Å). This results in a compressive lattice mismatch of -7.5%.

Figure 4.4 (a) illustrates the θ-2θ surveys of the Fe_3O_4/$SrTiO_3$ heterostructures. Each scan shows four main peaks, which correspond to the reflections of the $SrTiO_3$ (001) substrate. At $2\theta \approx 43°$ and $2\theta \approx 95°$, additional peaks appear, corresponding to the Fe_3O_4 (004) and (008) reflections. These Fe_3O_4 reflections show up for all films except for the one grown at $T_{growth} = 200\,°\mathrm{C}$, revealing the amorphous nature of the latter one. The presence of only two reflections, (004) and (008), for all other films indicates the epitaxial and single-crystalline growth even at high temperatures.

Detailed θ-2θ scans around the Fe_3O_4 (004) and $SrTiO_3$ (002) reflections are shown in Figure 4.4 (b). For all films grown at different temperatures, the Fe_3O_4 (004) peak positions are shifted from the position of bulk-like Fe_3O_4 (blue dashed line). For the Fe_3O_4 film grown at $T_{growth} = 400\,°\mathrm{C}$, the Fe_3O_4 (004) peak is very close to the bulk position. In contrast, for the Fe_3O_4 film grown at $T_{growth} = 500\,°\mathrm{C}$, the (004) peak is shifted towards larger angles. However, for the Fe_3O_4 films grown at $T_{growth} = 300\,°\mathrm{C}$ and $350\,°\mathrm{C}$, the (004) peak is shifted towards smaller angles. The XRD 2θ angle is related

---

[3] We introduce a detailed explanation for the XRR experiment which clarifies the challenges may face the calculation of roughness by XRR Appendix A.3.

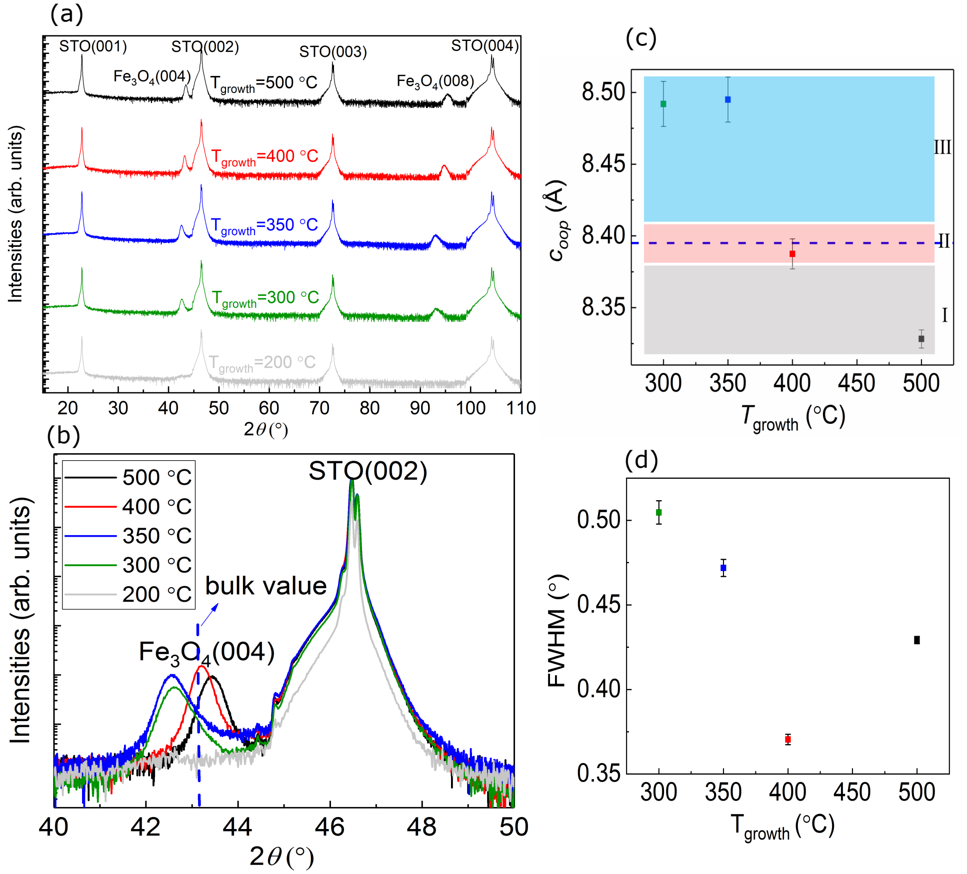

Figure 4.4: Out-of-plane X-ray diffraction θ-2θ scans of Fe_3O_4 films grown at different temperatures of (a) all reflections (survey) and (b) the Fe_3O_4 (004) reflection. (c) The out-of-plane lattice constant c_{oop} representing the three regions: I) tensile strain, II) absence of strain (relaxed growth) and III) compressive strain. (d) The FWHM of Fe_3O_4 (004) reflections, for the films with respect to the growth temperature.

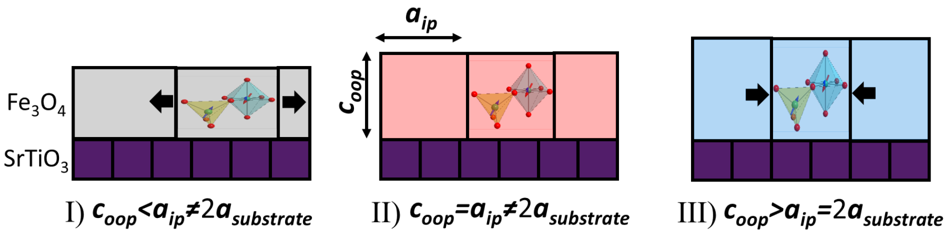

Figure 4.5: Schematics of Fe_3O_4 unit cells grown on $SrTiO_3$, representing the three possible distortions I) tensile strain, II) absence of strain (relaxed growth) and III) compressive strain.

to the out-of-plane lattice constant by Braggs law (Equation 3.2.1). The temperature dependence of 2θ angle implies the temperature dependence of the out-of-plane lattice constant c_{oop}.

Ideally, if the Fe_3O_4 films are totally relaxed, the out-of-plane equals the in-plane lattice constant as well as the bulk lattice constant of Fe_3O_4. If the films are totally strained, the in-plane lattice constant of the Fe_3O_4 films equals the in-plane lattice constant of the $SrTiO_3$ substrate. The out-of-plane lattice constant c_{oop} versus the growth temperature T_{growth} of the films is depicted in Figure 4.4 (c). The plot can be divided into three regions, indicating (I) tensile strain, (II) absence of strain (relaxed growth) and (III) compressive strain. Under the assumption that unit cell is volume preserved: the out-of-plane lattice constant of the $T_{growth} = 400\,°C$ film is only slightly smaller than the bulk value of Fe_3O_4, $c_{oop} = 8.3875 \pm 0.01\,Å$. Thus, we expect that the out-of-plane lattice constant equals the in-plane lattice constant, meaning that the film is totally relaxed (region II). The out-of-plane lattice constant of the $T_{growth} = 500\,°C$ film ($c_{oop} = 8.328 \pm 0.006\,Å$) is smaller than the bulk value (region I), indicating unexpected tensile strain. In contrast, the out-of-plane lattice constants of the $T_{growth} = 300\,°C$ and $350\,°C$ films ($c_{oop} = 8.492 \pm 0.016\,Å$ and $8.495 \pm 0.016\,Å$, respectively) are larger than the bulk value, indicating the expected compressive strain (region III).

4.2.5 Discussion

We grew a series of Fe_3O_4 thin films at different growth temperatures. The growth temperature influences the surface morphology and structural properties. Smooth surfaces have been observed for growth temperatures $<500\,°C$. However, the film grown at $T_{growth} = 500\,°C$ has a rough surface. The high roughness can be explained by the island growth mode, which is a result of (1) the negative lattice mismatch of $-7.5\,\%$. (2) At high growth temperature, the ions have enough energy to move freely on the $SrTiO_3$ surfaces. Therefore, the ions are clustered and form islands. Thus, smooth surfaces at lower growth temperatures can be explained as the Fe_3O_4 is biaxially strained and grows epitaxially in a layer by layer growth mode. As a consequence, the Fe_3O_4 films adopt the surface structure of the STO substrates, causing the STO terraces to appear in the AFM images. In this case, the films experience compressive strain as indirectly observed by the out-of-plane lattice constant measurements.

In literature, the Fe_3O_4 films grown on STO were assumed to be totally relaxed if their thickness $d \geq 10 \times d_{critical} = 70\,\mathrm{nm}$ [88]. The in-plane lattice constant of the relaxed Fe_3O_4 film equals the bulk lattice constant of Fe_3O_4. If $d < d_{critical} = 7\,\mathrm{nm}$ the films are strained, i.e. the in-plane lattice constant of the film equals the lattice constant of the substrate. In between those two thicknesses, the films are expected to be partially strained. In this case, we can estimate the film's in-plane lattice constant a_{ip} by the equation

$$a_{ip} = a_o + \frac{d_{critical}}{d}(2a_{substrate} - a_o) \tag{4.2.2}$$

where a_o is the ideal bulk value of the Fe_3O_4 lattice constant and $a_{substrate}$ is the $SrTiO_3$ substrate's lattice constant [89]. The factor two accounts for the fact that the mismatch is calculated between *two* STO unit cells and *one* Fe_3O_4 unit cell. Ideally, our film thickness d equals 38 nm. Thus, the films' in-plane lattice constant a_{ip} is calculated to equal 8.287 Å. The unit cell volume a_0^3 is constant and equals 591.646 $\mathrm{\AA}^3$. Therefore, the out-of-plane lattice constant equals 8.615 Å. None of our Fe_3O_4 films have an out-of-plane lattice constant equal to the calculated one. The closest value is 8.495 Å for the film grown at $T_{growth} = 300\,°\mathrm{C}$. Although the Fe_3O_4 film grown at $T_{growth} = 400\,°\mathrm{C}$ has only a film thickness of 38 nm, which is much smaller than the theoretical total relaxation thickness of $d = 70\,\mathrm{nm}$, it is totally relaxed. This observation has also been proven by a series of X-ray magnetic linear dichroism (XMLD) measurements and calculations which were performed on the same film by the group of Frank de Groot, Debye Institute for Nanomaterials Science, Netherlands [90].

4.3 Chemical and magnetic structure

We now study the stoichiometry and magnetic structure of the magnetite films using synchrotron-based spectroscopy. The depth profiling and element-selective chemical structure analysis of the films and buried interfaces are conducted by hard X-ray photoelectron spectroscopy (HAXPES). In order to investigate the element selective magnetic structure, X-ray absorption spectroscopy (XAS) and X-ray magnetic circular dichroism (XMCD) are conducted.

4.3.1 Experimental details

Element-selective and depth-dependent chemical information of the films and buried interfaces were obtained by hard X-ray photoelectron spectroscopy (HAXPES) at PETRA III (DESY, Hamburg). All spectra shown in this chapter were taken using a photon

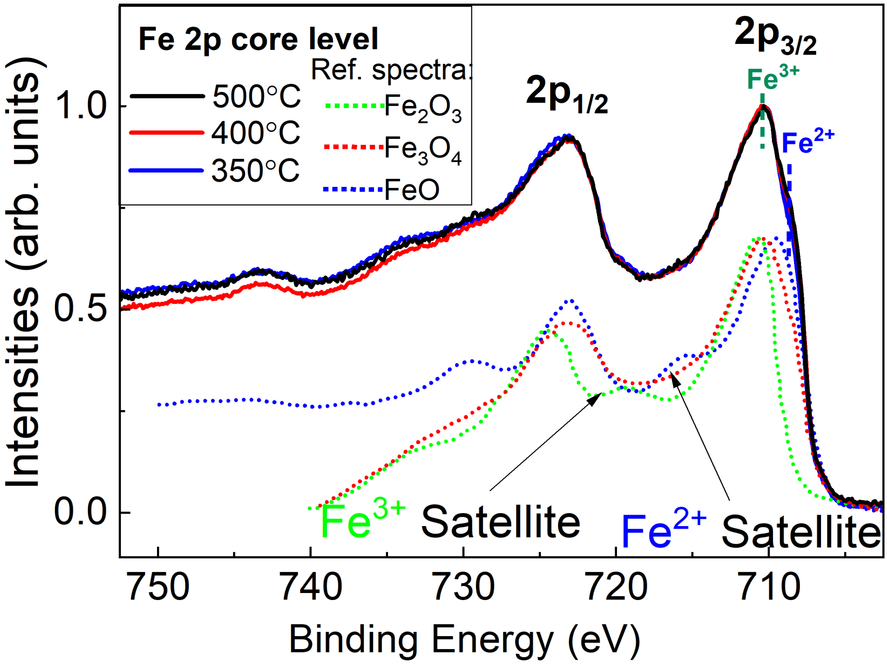

Figure 4.6: Fe 2p core level spectra of $Fe_3O_4/SrTiO_3$ (001) grown at different temperatures recorded using a photon energy of $h\nu = 6$ keV. Reference spectra were extracted from [61, 62].

energy of $h\nu = 6$ keV at room temperature and in a normal emission geometry with an angle $\theta = 5°$ normal to the sample surface. The information depth depends on the inelastic mean free path λ and the geometry of the experiment. Furthermore, the inelastic mean free path depends on the kinetic energy of the electron as explained in Section 3.3.3. For Fe_3O_4 and a photon energy of $h\nu = 6$ keV in normal emission geometry, the information depth is approximately 25-30 nm.

By XMCD, spin and orbital moments of the films are calculated. XMCD spectra obtained from X-ray absorption spectroscopy (XAS) were performed at I10 beamline "BeamLine for Advanced Dichroism Experiments" (BLADE) at the Diamond Light Source in Didcot, UK. The samples were cooled down to 10 K and a magnetic field of 1 T was applied parallel to the surface of the sample. The experimental geometry was chosen such that the sample surface is aligned at a grazing angle of 80° (in-plane [100] axis) with respect to the incident beam (near-grazing emission). XAS spectra were recorded in total electron yield mode (TEY) by measuring the sample drain current. In order to calculate the XMCD asymmetry, four absorption spectra were taken for each sample using left (+) and right (-) circular polarization in the sequence (+ - - +).

4.3.2 HAXPES

Fe 2p core-level HAXPES spectra of 38 nm thick Fe_3O_4 films grown at different growth temperatures are depicted in Figure 4.6. In order to identify the chemical properties, the experimental spectra were compared to the reference spectra of FeO, Fe_2O_3 and Fe_3O_4 [61, 62]. Two features are observed to differentiate between the iron oxides phases: (1) the satellite peak and (2) the Fe $2p_{3/2}$ core level peak/shoulder. The origin of the satellite peak is described in Section 3.3.4. First, for FeO and Fe_2O_3, the satellite's binding energies are 715.5 eV and 719 eV, respectively, which can be easily distinguished by lab-XPS (resolution: $\Delta E = 0.8$ eV) and HAXPES ($\Delta E = 0.2$ eV). For Fe_3O_4, which has a mixed oxidation state of Fe^{2+} and Fe^{3+}, the satellites of both states merge, as depicted in Figure 4.6. For all studied Fe_3O_4 films, we find that the two satellites are indeed merged. Second, the Fe $2p_{3/2}$ core level peaks of the three Fe_3O_4 films grown at different temperatures are composed of the Fe^{3+} peak and a shoulder that refers to Fe^{2+}. Consequently, all three films consist of stoichiometric Fe_3O_4 in the detection limit of the HAXPES experiment.

In summary, the analysis of the satellites and Fe $2p_{3/2}$ core level suggest the formation of stoichiometric films for all applied growth temperatures.

4.3.3 XAS and XMCD

XAS of Fe $L_{2,3}$-edge

Next, we determine the element-specific magnetic properties of the $Fe_3O_4/SrTiO_3$ films. We can distinguish between the different iron oxides, in particular, Fe_3O_4, α-Fe_2O_3 and γ-Fe_2O_3 by the XAS spectra [91]. The average XAS spectrum is calculated by averaging the four polarized absorption spectra (+ - - +). XAS spectra of the Fe $L_{2,3}$-edge of films grown at different growth temperatures are shown in Figure 4.7 (a), (b) and (c). The pre-edge features A and D are mainly related to $Fe^{2+}_{O_h}$. They are almost similar for all films. The peaks B, C, E and F originate from mixed contributions of $Fe^{2+}_{O_h}$, $Fe^{3+}_{T_d}$ and $Fe^{3+}_{O_h}$ sites. We observe that both, intensity ratios and peak positions are almost identical for the films. Only the 500 °C film shows a slightly lower intensity at the C peak position. The difference in the intensity is mostly not related to off-stoichiometry, because all the pre-edge features A and D are similar, which are considered to be stoichiometric detectors. This indicates the consistency of the Fe^{2+} and Fe^{3+} ratios in all films, in line with the HAXPES results.

XMCD of Fe $L_{2,3}$-edge

In order to calculate the XMCD asymmetry, the differences between the two absorption spectra with left- (+) and right-handed (-) circular polarized light are calculated according to Equation 3.3.10. Figure 4.8 exemplarily shows two XAS spectra of the Fe_3O_4 film grown at $T_{growth} = 400$ °C recorded with opposite circular polarization. Due to the ferrimagnetic nature of Fe_3O_4, the two polarized XAS spectra differ in the L_3- and L_2-edges. Figure 4.9 illustrates the Fe $L_{2,3}$-edge XMCD spectra of the three films grown at different

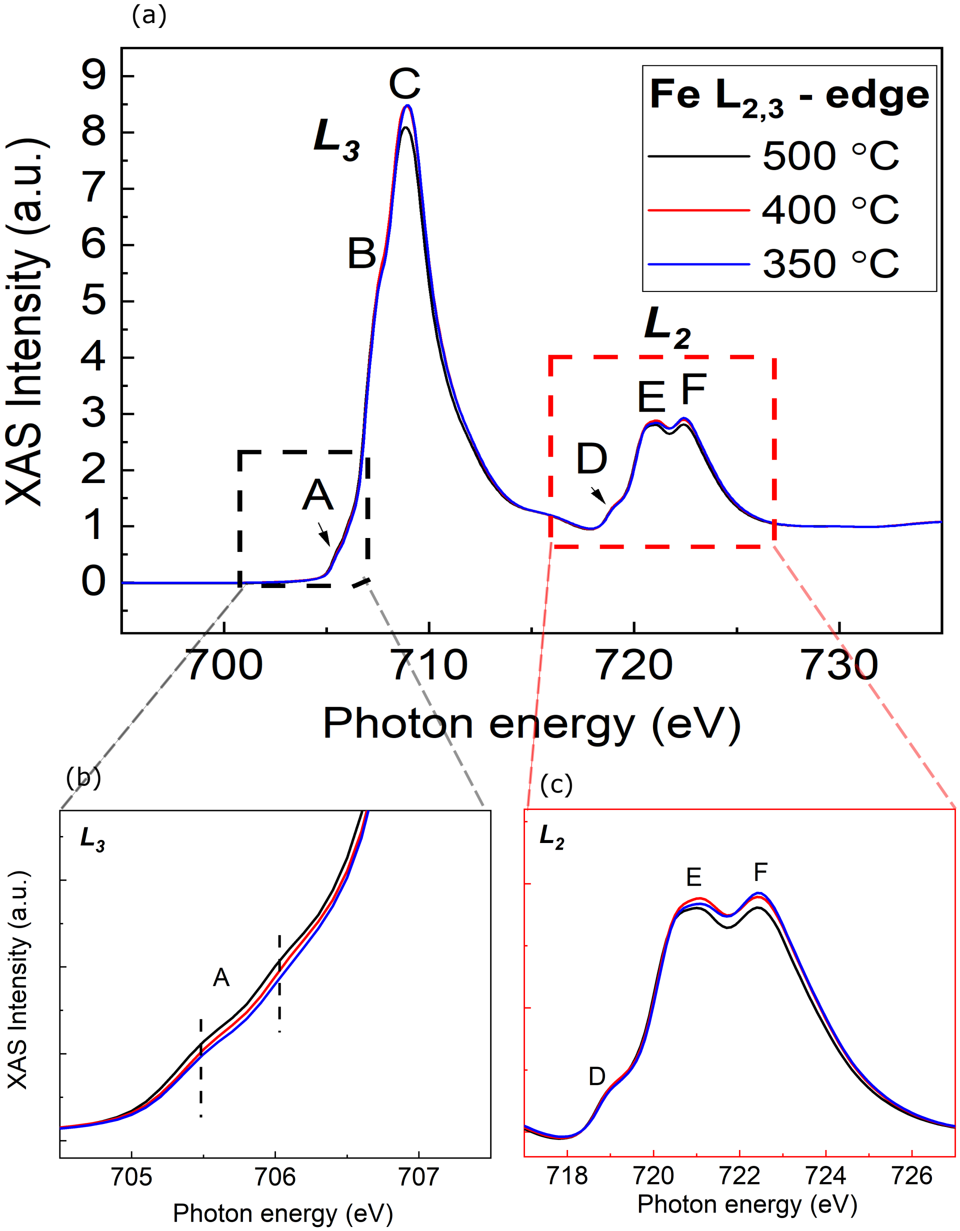

Figure 4.7: (a) Fe $L_{2,3}$-edge XAS spectra of Fe_3O_4 films with varying growth temperature, XAS fine structure of (b) L_3 and (c) L_2 edge.

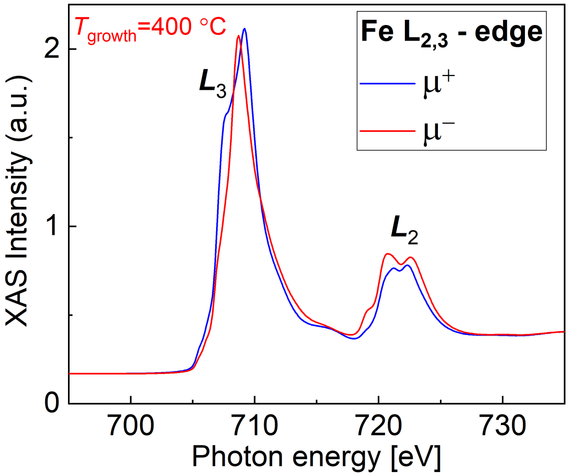

Figure 4.8: Two XAS spectra of the Fe_3O_4 film grown at $T_{growth} = 400\,°C$ recorded with two different X-ray polarization, a left- μ^+ and right-handed μ^-.

temperatures. For the L_3 edge (Figure 4.9 (b)), the two pre-edge peaks a and b originate mainly from $Fe^{2+}_{O_h}$. Their peak intensities are almost the same for all three Fe_3O_4 films. The peaks c, d and e are well-known fingerprints for distinguishing Fe_3O_4 from γ-Fe_2O_3 [92, 93]. The $Fe^{2+}_{O_h}$ (c peak) and $Fe^{3+}_{O_h}$ (e peak) are ferromagnetically coupled (negative XMCD L_3 edge) and antiferromagnetically coupled to $Fe^{3+}_{T_d}$ (d peak) (positive XMCD L_3 edge), see Section 3.3.7. The literature values of the intensity ratio between the c and e peak I_c/I_e is 1.5 and 0.4 for Fe_3O_4 and γ-Fe_2O_3, respectively [92]. For the three Fe_3O_4 films, I_c/I_e is within the error equal to 1.5, which indicates the proper stoichiometry of Fe_3O_4. Furthermore, in the L_2 edge XMCD (Figure 4.9 (c)), peak f corresponds to $Fe^{2+}_{O_h}$, peak g corresponds to $Fe^{2+}_{O_h}$, $Fe^{3+}_{T_d}$ and $Fe^{3+}_{O_h}$ and peak h corresponds to $Fe^{3+}_{T_d}$. All these features are similar for the three Fe_3O_4 films. This again indicates the films' Fe_3O_4 stoichiometry.

Spin and orbital moment: the sum rules

The sum rules are conducted to calculate the element specific orbital and spin magnetic moment [71, 72]. Figure 4.10 shows XAS and XMCD spectra exemplarily for the Fe_3O_4 film grown at $T_{growth} = 400\,°C$. Their integration is needed to determine the integrals p, q and r according to Equations 3.3.13 and 3.3.14. The r integral equals the area below the $L_{2,3}$ edge of the average XAS spectrum.

Our experimental spectra consist of (1) the $L_{2,3}$ edge which is basically formed as a result of the transitions from 2p to 3d and (2) a background which is formed by transitions to higher final states (4s and vacuum). The background transitions are known as the characteristic edge jump. Thus, to calculate the r, we have to subtract the background. We modeled the background by a two-step function, which typically is used for itinerant magnets [72] but works as reasonably well for the magnetite Fe L-edge [94]. The two-step function is fitted such that the height ratio between the remaining L_2- and L_3-edge equals 1:2. The two-step function edges are defined at 707.6 eV for the L_3 edge and 720.8 eV for

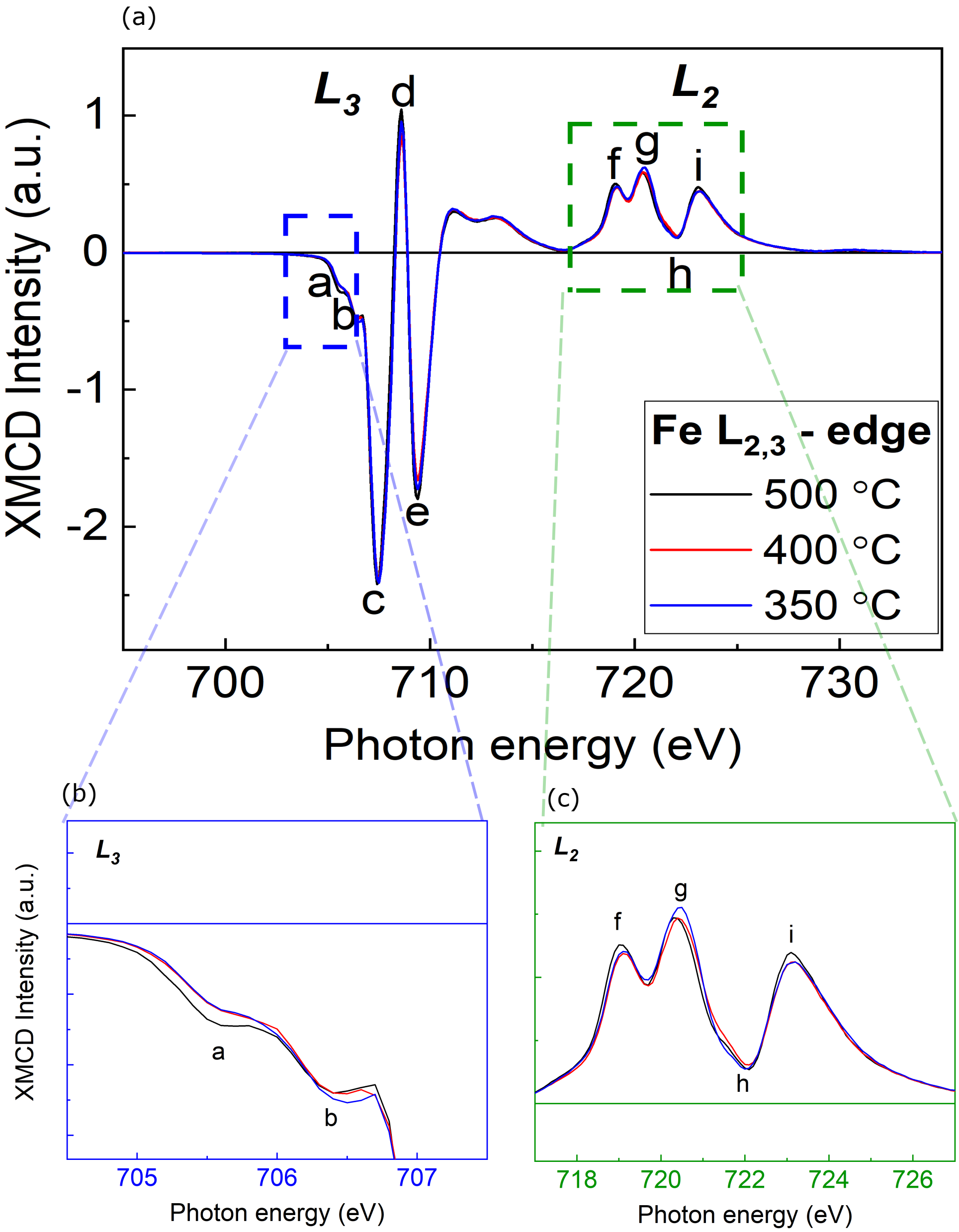

Figure 4.9: (a) Fe $L_{2,3}$-edge XMCD spectra of Fe_3O_4 films with varying growth temperature, (b) L_3 and (c) L_2 edge XMCD fine structure, respectively.

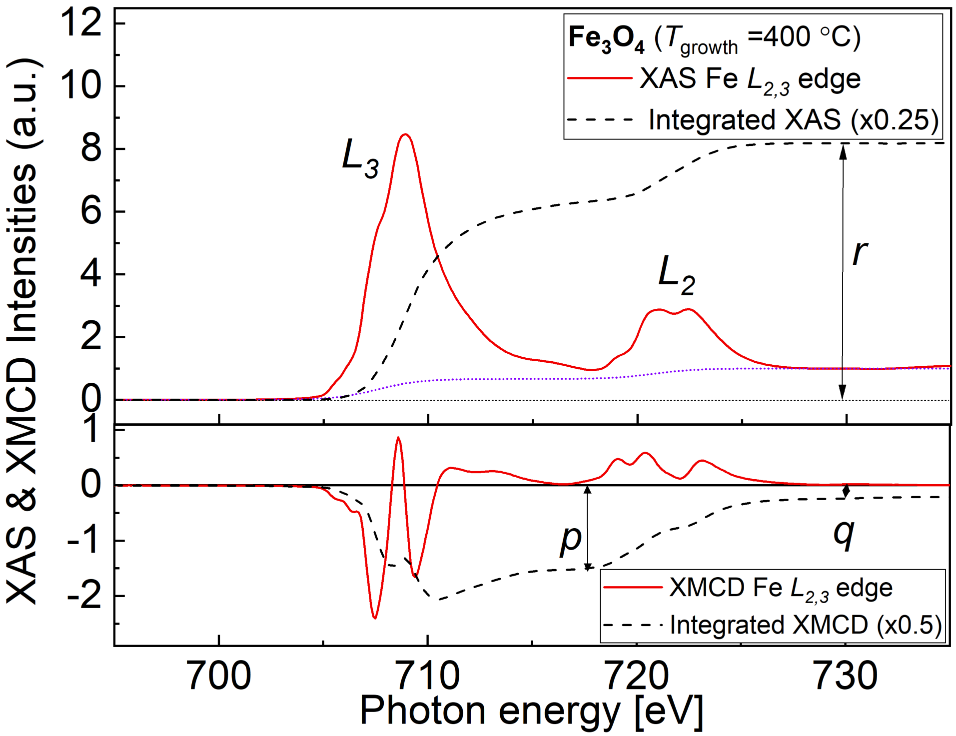

Figure 4.10: Top: average XAS of the Fe $L_{2,3}$-edge (solid line) and its integration (dashed line) after the subtraction of the step function background. Bottom: XMCD (solid line) and its integration (dashed line), of the Fe_3O_4 film grown at 400 °C.

Figure 4.11: Spin and orbital magnetic moments calculated (black solid and blue doted lines, respectively) from XMCD spectra of films grown at different temperature, compared to M_S measured by VSM (black dashed line).

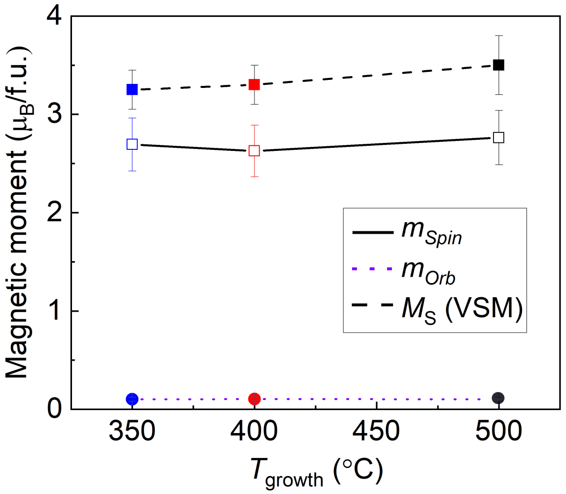

the L_2 edge. The step function is given by

$$\mu_{step} = \frac{2}{3}\frac{1}{1+e^{E_{L_3}-E}} + \frac{1}{3}\frac{1}{1+e^{E_{L_2}-E}} \quad . \tag{4.3.1}$$

Finally, the two-step function representing the background is subtracted and the integral below the average XAS spectrum is calculated.

The calculated spin and orbital magnetic moments as a function of the growth temperature are shown in Figure 4.11. The spin magnetic moment of the three films equals 2.6-2.8±0.3 μ_B/f.u., which makes them growth temperature independent. The orbital magnetic moment of all Fe_3O_4 films is less than 0.2 μ_B/f.u.. Thus, the total magnetic moment is dominated by the spin magnetic moment. However, the spin magnetic moment is 20 % lower than M_S determined by VSM. The VSM measurements will be discussed in the next section. Moreover, they are much lower than the theoretical bulk value of 4 μ_B/f.u.. The reduction of the spin moment can be explained as follows: (1) theoretical studies have shown that the sum rules on $3d^s$ systems can show up to 30 % error of the ground state properties [95]. (2) In recent studies on Fe_3O_4 films and nanoparticles [96, 97], m_{Spin} measured with an applied magnetic field of 1 T equals 75-80 % of the spin magnetic moment measured at a higher applied field. This means that the magnetic field of 1 T which was applied in our work is not enough to saturate (maximize) the magnetization[4]. Therefore, the XMCD and VSM measurements are consistent.

In summary, the HAXPES, XAS and XMCD spectra prove the stoichiometry of the Fe_3O_4 films which is independent of the growth temperature.

4.4 Magnetic characterization

In this section, we will discuss the effect of growth temperature on the magnetic properties of Fe_3O_4 films. Two important parameters determine the magnetic quality of the magnetite films: (1) the saturation magnetization and (2) the Verwey transition. Ideally, magnetite has a total magnetic moment of 4 μ_B/f.u. [98] and a Verwey transition of $T_V = 120$ K [33].

4.4.1 Experimental details

The magnetic properties of the samples are investigated with two complementary techniques: (1) the global magnetic properties of the entire films are detected by vibrating sample magnetometry (VSM). (2) The magnetic structure of the films is recorded by the elemental-selective X-ray magnetic circular dichroism (XMCD). In this section, we focus on the VSM measurements. The VSM is a module of the Quantum Design Dynacool physical property measurement system (PPMS). Hysteresis loops were recorded

---

[4] Detailed explanations for our XMCD experiment and calculations are given in Appendix A.2.

at different temperatures $T = 5$-$300\,K$ with a magnetic field of $H = \pm\,5\,T$, which was applied parallel to the in-plane [100]-axis. In addition, magnetization versus temperature ($M(T)$) curves were recorded in zero-field cooling (ZFC) mode with an applied field of $H = 500\,Oe$ parallel to the in-plane [100]-axis.

4.4.2 Saturation magnetization

In order to determine the saturation magnetization of the Fe_3O_4 films, hysteresis loops (magnetization versus magnetic field $M(H)$) have been measured. The diamagnetic contribution from the $SrTiO_3$ substrate has been corrected as we discussed in Section 3.2.3. In Figure 4.12 (a-c), the hysteresis loops with magnetic field of ±2500 Oe at several temperatures for the films grown at $T_{growth} = 500$, 400 and 350 °C are depicted. The hysteresis loops have been measured by applying the magnetic field parallel to the in-plane [100] axis of the films, as it is shown in the schematic Figure 4.12 (d). The hysteresis loops of the three films show different behavior. Three main differences can be observed: (1) the saturation magnetization, (2) the coercivity, and (3) the remanent magnetization. The magnetization of the films reaches saturation at a magnetic field of 1.2 T. The saturation magnetization of all films is identical within the respective errors throughout all the measured temperatures (3.3-3.4 μ_B/f.u.). The saturation magnetization of the films is reduced compared to the theoretical value of 4 μ_B/f.u. [98]. The film magnetization is probably affected by structural dislocations and the formation of antiferromagnetic anti-phase boundaries, which is a well-known phenomenon for Fe_3O_4 [47, 99, 100].

Although the saturation magnetization of the films is rather similar, the coercivity and remanent magnetization of the films show clear discrepancies. The coercivity and the remanent magnetization of ideal magnetite may be affected by three factors [101–104]:

- Crystal anisotropy:

  The cubic structure of bulk magnetite has a magnetic easy axis along the [111] direction [105]. However, for the monoclinic structure below the Verwey transition, the magnetic easy axis is [100] [106]. Furthermore, the coercivity is enhanced by two orders of magnitude below the Verwey transition T_V of 120 K.

- Shape anisotropy:

  The nearest in-plane magnetic easy axis of Fe_3O_4 is [110] for thin films instead of [111] for bulk crystal [107].

- Stress anisotropy:

  Below the Verwey transition, the transition from cubic to the lower symmetry monoclinic phase causes an increase in the coercivity and a decrease of the remanent magnetization [108].

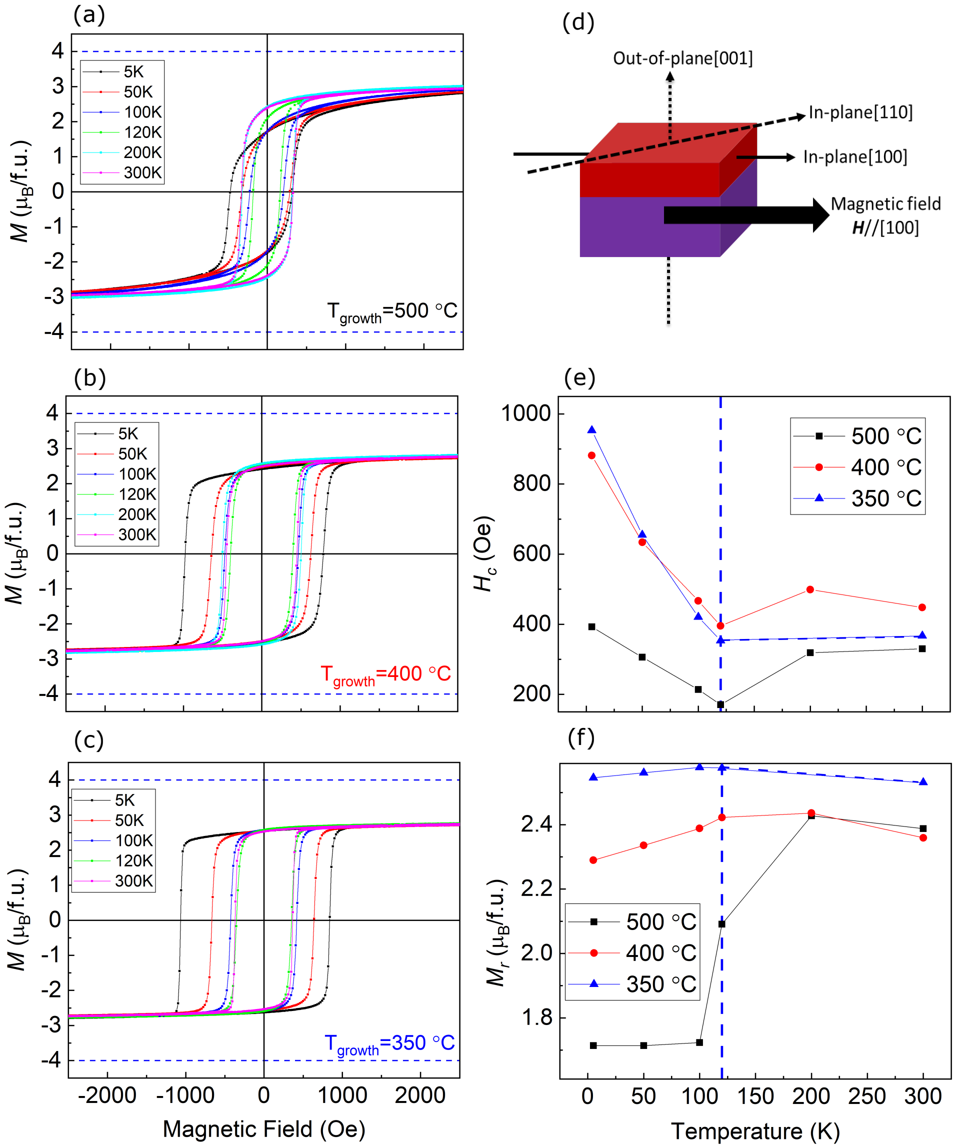

Figure 4.12: Hysteresis loops for Fe_3O_4 films grown at temperatures of (a) 500 °C, (b) 400 °C and (c) 350 °C, recorded at various temperatures. (d) Schematic showing the magnetic field direction parallel to the in-plane axis [100] of the sample. The calculated values of (e) coercivity H_c and (f) remanent magnetization M_r, for the Fe_3O_4 films grown at different growth temperatures. The blue dashed lines indicate the Fe_3O_4 bulk values of the saturation magnetization and Verwey transition.

4.4.3 Coercivity and remanent magnetization

Figure 4.12 (e) and (f) depict the coercivity H_c and remanent magnetization M_r of the three films as a function of the temperature. The coercivity is known to reflect the quality of the films. For ideal bulk magnetite, the coercivity is 100-400 Oe and increases at temperatures below the Verwey transition. As shown in Figure 4.12 (e), the coercivity of the three films behaves almost identical; it decreases slightly around Verwey transition (blue line) and increases again at low temperatures. We divide the curve into two regions, (1) T>120 K and (2) T<120 K.

(1) T>120 K:

The coercivities of the three films range between 330-448 Oe. They are slightly above the ideal bulk value of magnetite, which can be explained by the formation of dislocations and anti-phase boundaries.

(2) T<120 K:

The coercivity increases to 882 Oe and 953 Oe for the Fe_3O_4 films grown at temperatures of $T_{growth} = 400$ °C and $T_{growth} = 350$ °C, respectively. However, it increases only to 393 Oe for the Fe_3O_4 film grown at $T_{growth} = 500$ °C. On one hand, the coercivity increases due to the structural transition below the Verwey transition from cubic to monoclinic [108]. On the other hand, the differences between the coercivity of the films grown at $T_{growth} = 500$ °C and $T_{growth} = 350$ °C may be related to the tensile and compressive strain induced by the growth condition. The strain causes the deformation of the tetra and octahedral sites which may alter the magnetic easy axis directions, consequently the coercivity.

The alteration of the easy axis directions can be confirmed by the "squareness" of the hysteresis loops or in other words, the remanent magnetization. We calculated the remanent magnetization of the three films as a function of measured temperature as depicted in Figure 4.12 (f).

- For the Fe_3O_4 film grown at $T_{growth} = 500$ °C, the remanent magnetization decreases by 30 % around the Verwey transition ($T_V = 120$ K).

  The remanent magnetization decreases below the Verwey transition because of the structural transition from cubic to monoclinic [108]. This transition changes the easy axis direction from [110] to [100] [106].

- For the Fe_3O_4 films grown at $T_{growth} = 400$ °C and $T_{growth} = 350$ °C: the remanent magnetization decreases slightly by 4 %. Additionally, their hysteresis loops are perfectly square above and below the Verwey transition.

  This indicates unexpectedly that the magnetic easy axis is [100] above and below the Verwey transition which may be attributed to the strain effect induced by the growth conditions. Further experiments are needed to understand this unexpected behaviour as it will be discussed in Section 4.5.

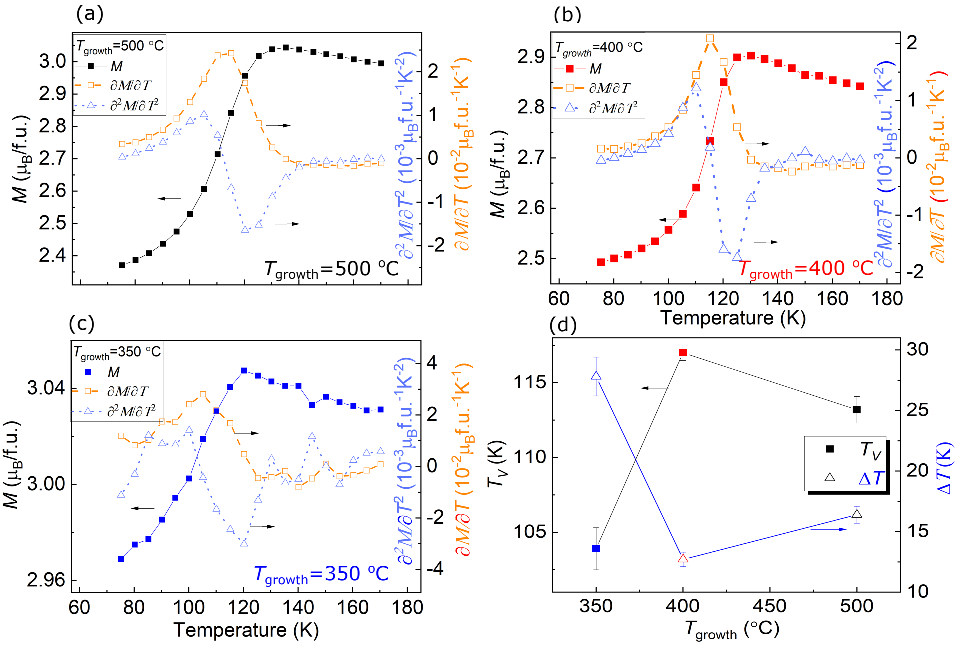

Figure 4.13: Magnetization vs. temperature (solid square), the first and second derivatives for the magnetization curve (open square and open triangle respectively) of films grown at temperatures (a) 500 °C, (b) 400 °C, and (c) 350 °C. (d) Verwey transition T_V and transition width ΔT as a function of growth temperature (solid square and open triangle, respectively).

To summarize, the coercivity and remanent magnetization of the different strained films indicate the alteration of the easy axis direction due to mainly the Verwey transition and additionally the crystal distortion.

4.4.4 Verwey transition

The Verwey transition T_V is considered as an indicator for the Fe_3O_4 stoichiometry. It is strongly influenced by the oxygen content [109, 110]. Moreover, the Fe_3O_4 magnetization decreases at T_V due to the decrease of the symmetry to a monoclinic structure [36]. For nonstoichiometric $Fe_{3\text{-}\delta}O_4$ single crystals, it is reported that the Verwey temperature decreases with increasing δ. However, if $\delta > 0.045$, no Verwey transition can be found [110]. Generally, T_V is influenced by the growth conditions [80, 111–113], substrate choices [111, 114, 115], and film thicknesses [111, 112, 116, 117].

We detect the Verwey transition by the magnetization measurements through the temperature scale ($M(T)$ curve), because the magnetization drops below the Verwey transition

Table 4.1: Magnetization parameters of $Fe_3O_4/SrTiO_3$ heterostructures grown at different growth temperatures determined from the MT curves.

T_{growth} (°C)	T_V (K)	ΔT_V (K)	**Magnetization drop** (%)
350	104±1.4	26.8±1.6	3
400	117±0.6	12±0.6	14
500	113±0.9	16.4±0.7	20

due to the structural transition. Figure 4.13 depicts the different $M(T)$ curves of the three Fe_3O_4 films grown at different growth temperatures measured in zero-field cooling mode with an applied field of 500 Oe. The magnetization as a function of temperature $M(T)$ of the films (solid square) drops around 120 K referring to the Verwey transition. To exactly determine the Verwey transition T_V, the maximum $\partial M/\partial T$ (open square) is calculated. To determine the transition width ΔT_V (the sharpness of the transition), the maximum of $\partial^2 M/\partial T^2$ (open triangle) is calculated. Three main observations are made:

- The decrease of the magnetization of the Fe_3O_4 film grown at $T_{growth} = 500$ °C is about 20 % below T_V, whereby it is only about 3 % for the Fe_3O_4 film grown at $T_{growth} = 350$ °C (Figure 4.14).

  The decrease of the magnetization is known to be affected by the measurement symmetry, i.e. whether the field is parallel to the easy axis or not [118]. We found that the decrease of the magnetization increases with increasing growth temperature. Since we did not change the field direction during the measurements, we conclude that the easy axis alters as a function of the growth temperature.

- The Verwey transition of the Fe_3O_4 film grown at $T_{growth} = 400$ °C appears at $T_V = 117 \pm 0.6$ K. It is close to the bulk value of 120 K. The T_V values of the Fe_3O_4 film grown at $T_{growth} = 350$ °C and 500 °C are significantly lower, see Table 4.1.

  As mentioned above, the value of the Verwey transition temperature is an indicator for the stoichiometry of the Fe_3O_4 film. Thus, we assume that the film grown at $T_{growth} = 400$ °C is stoichiometric. However, for the other two films, off-stoichiometry cannot be concluded just from the reduced Verwey transition temperature, as it may also be caused by strain [100, 111, 119–121]. It is shown in Section 4.3 via HAXPES and XMCD measurements that all three films are stoichiometric. Thus, it can be concluded that the reduced T_V is caused by strain.

- The sharpest transition is shown for the Fe_3O_4 film grown at $T_{growth} = 400$ °C with the smallest transition width of $\Delta T_V = 12 \pm 0.6$ K, which suggests a bulk-like stoichiometry of the Fe_3O_4 film, see Table 4.1.

In summary, we assume that the Verwey transition is influenced by (1) the stoichiometry of the Fe_3O_4 film which is confirmed by HAXPES and XMCD and (2) the strain induced

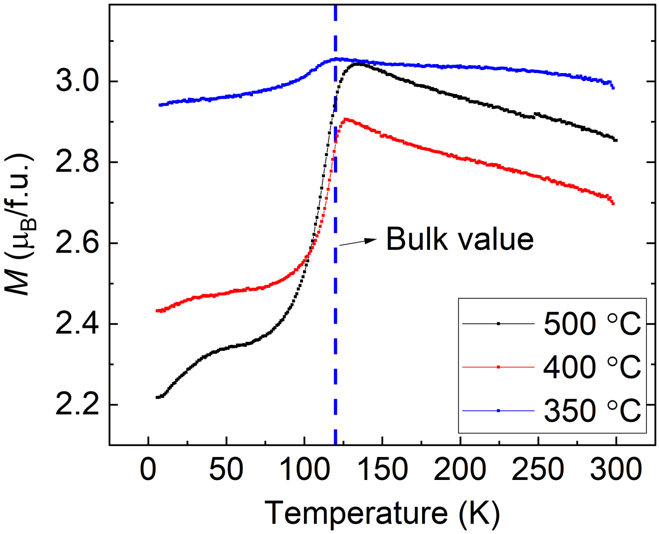

Figure 4.14: A summary of the magnetization vs. the temperature ($M(T)$ curve) of the Fe_3O_4 films grown at variant temperatures.

by the substrate and growth conditions which may alter the magnetic easy axis direction as we will discuss in the next section.

4.5 Growth-induced lattice strain versus magnetic easy axis?

After confirming the stoichiometry of the films, the next step is to understand the effect of the lattice distortion on the easy axis. In order to examine the effect of distortion (tensile and compressive strain), we compare the magnetic properties measured by the VSM of the films grown at temperatures $T_{growth} = 500\,°C$ and $350\,°C$. We applied a magnetic field parallel to the [100]- and [110]- direction. The [110] direction is expected to be the easy axis for the Fe_3O_4 films. However, the [100] direction is found to be the easy axis for the Fe_3O_4 films grown on $SrTiO_3$ (100) [122]. Not all previous studies on $Fe_3O_4/SrTiO_3$ heterostructures confirmed that the easy axis is [100] [123]. Some literature observed an easy axis of [110] for the $Fe_3O_4/SrTiO_3$ system [123]. There are no clear explanations about the alteration of the easy axis directions. In the next section, we explain the effect of strain induced by the STO substrates and growth conditions on the magnetic properties of Fe_3O_4 film, in particular, the magnetic easy axis.

4.5.1 Experimental details

Hysteresis loops were recorded at different temperatures $T = 5\text{-}300\,K$ with a magnetic field of $H = \pm 5\,T$, which was applied parallel to the in-plane [100] and in-plane [110]-axis.

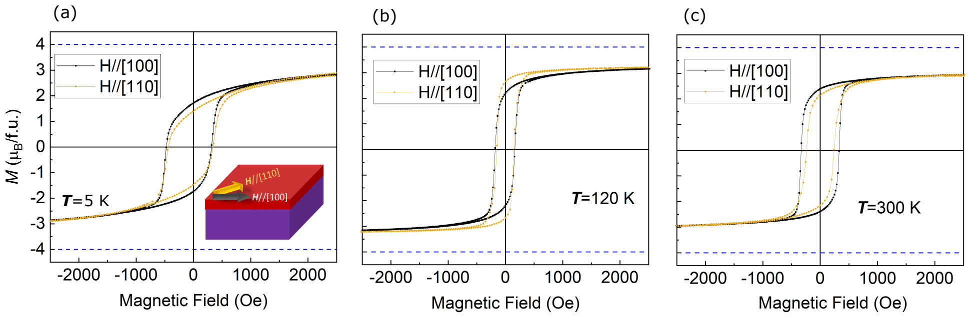

Figure 4.15: The hysteresis loops of the Fe_3O_4 film grown at $T_{growth} = 500\,°C$ measured with an external magnetic field applied along [100]- (black) and [110]- (gold) direction at temperatures (a) 5 K, (b) 120 K, and (c) 300 K.

In addition, magnetization versus temperature ($M(T)$) curves were recorded in zero-field cooling (ZFC) mode with an applied field of $H = 500$ Oe parallel to the in-plane [100]- and [110]-axis.

4.5.2 Tensile strain (500 °C)

The Fe_3O_4 film grown on a $SrTiO_3$ substrate at $T_{growth} = 500\,°C$ is supposed to possess a tensile strain as we discussed in Section 4.2.

Hysteresis loop and remanent magnetization

The hysteresis loops have been recorded at temperatures above, at and below the Verwey transition ($T = 5$, 120 and 300 K). Two hysteresis loops were recorded at each temperature: one with an external magnetic field applied along the [100] direction (i.e. parallel to the substrate edge, $\theta_H = 0°$), and another with a field along [110] ($\theta_H = 45°$) as shown in Figure 4.15. The measurements show two different behaviors:

- Figure 4.15 (a) and (c) show the hysteresis loops measured at 5 and 300 K. The remanent magnetization measured along the [100] direction is larger than the one measured along the [110] direction. This suggests that the [100] direction is the preferred easy axis direction.
- In contrast, the hysteresis loops measured at 120 K (Figure 4.15 (b)) show a higher remanent magnetization measured along the [110] direction than along the [100] direction. The [110] direction becomes the easy axis.

We extracted the remanent magnetization M_r of the tensile strained Fe_3O_4 film grown at $T_{growth} = 500\,°C$ as a function of temperature measured with an external magnetic field applied along the [100] and [110] axes (Figure 4.16). The remanent magnetization decreases around the Verwey transition ($T_V = 120$ K) for fields along the [100] and [110] axis. We divide Figure 4.16 into three regions according to the temperature:

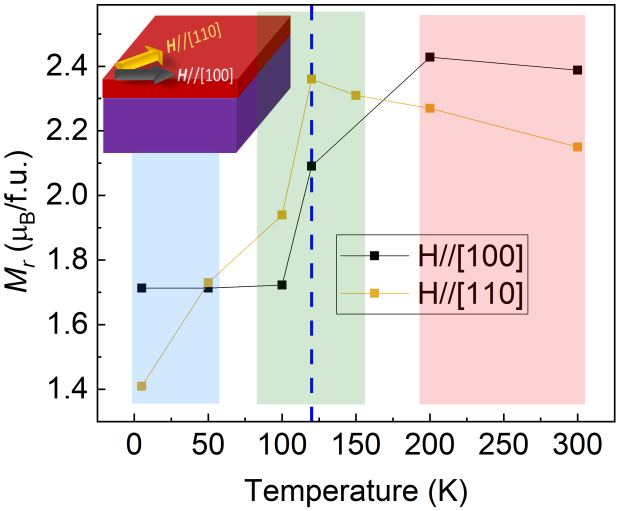

Figure 4.16: The remanent magnetization M_r of the tensile strained film ($T_{growth} =$ 500 °C) as a function of the temperature measured with an external magnetic field applied along the [100] (black) and [110] (gold) directions.

(1) 200 K< T <300 K:
The remanent magnetization measured along $H/\!/[100]$ is higher than the one measured along $H/\!/[110]$ which indicates that the easy axis is aligned along the [100] direction.

(2) 100 K< T <150 K:
In contrast to region (1), the remanent magnetization measured along $H/\!/[110]$ is higher which indicates the reorientation of the magnetic easy axis to the [110] direction. This switching of the easy axis is occurring around the Verwey transition ($T_V = 120$ K). This was also observed recently using MOKE [123].

(3) 5 K< T <50 K:
Additional switching is observed.The remanent magnetization measured with field of $H/\!/[100]$ is higher than $H/\!/[110]$. Now again the magnetic easy axis is [100].

At room temperature, the easy axis direction is switched by 45° to [100] in comparison to the bulk magnetite easy axis [110]. This observation was reported in the literature and was explained by a particular distribution of anti-phase boundaries (APBs), which leads to partial antiferromagnetic coupling. This may be responsible for the switching of the magnetic easy axis direction [122]. At $T < T_V = 120$ K, the easy axis is rotated by 45° to the [110] direction in comparison to the expected monoclinic magnetite easy axis [100]. This suggests that the [110] orientation of the magnetic easy axis at low temperatures is due to the antiferromagnetic coupling of APBs (Section 2.2.3). Thus, the APBs may not only cause switching of the easy axis direction at room temperature, but also in the low-temperature regime, which was claimed by a recent study using MOKE [123]. The MOKE study is not enough to confirm the particular distribution of APBs, and the emergent switching can also be attributed to the strain effect. Still, more experiments are needed to understand how the strain affects the magnetic behaviour of the Fe_3O_4/$SrTiO_3$ heterostructures.

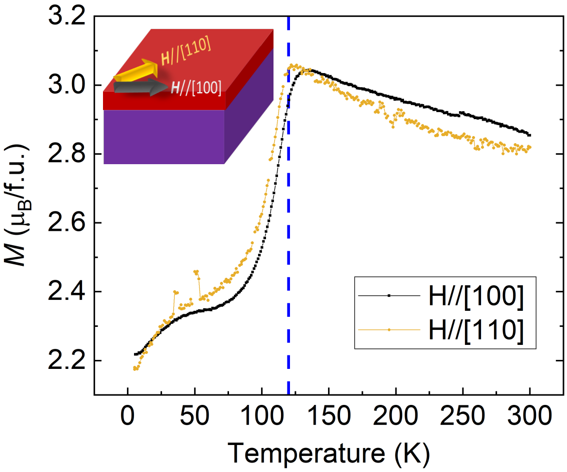

Figure 4.17: Magnetization vs. temperature of tensile strained Fe_3O_4 film ($T_{growth} =$ 500 °C) measured in ZFC mode with an external magnetic field applied along the [100] (black) and [110] (gold) directions.

Verwey transition

The $M(T)$ curve of the tensile strained Fe_3O_4 film ($T_{growth} = 500$ °C) is depicted in Figure 4.17. The magnetization measured along the [100] and [110] directions decreases around 120 K referring to the Verwey transition. The magnetization decreases by 20 % below T_V. This suggests that the in-plane easy axis direction switches along the temperature scale through the Verwey transition from [100] to [110].

4.5.3 Compressive strain (350 °C)

The Fe_3O_4 film grown on a $SrTiO_3$ substrate at $T_{growth} = 350$ °C possesses compressive strain as we discussed in Section 4.2.

Hysteresis loop and remanent magnetization

The hysteresis loops of compressive strained Fe_3O_4 film ($T_{growth} = 350$ °C) measured with an external magnetic field applied along [100]- and [110]- direction at temperatures below and above the Verwey transitions are depicted in Figure 4.18. The remanent magnetization measured along $H /\!/ [100]$ is higher than the one measured along $H /\!/ [110]$ for both temperatures ranges, below and above T_V (5 and 300 K). This suggests that the [100] direction is the preferred easy axis direction below and above T_V.

We determined the remanent magnetization M_r of the compressive strained Fe_3O_4 film ($T_{growth} = 350$ °C) as a function of temperature measured with an external magnetic field applied along the [100] and [110] axes (Figure 4.19). The remanent magnetization measured along the [110] axis decreases by 10 % below the Verwey transition ($T_V = 120$ K). However, the remanent magnetization measured along the [100] axis decreases by only 2 %. This observation confirms that the preferred easy axis above and below the Verwey

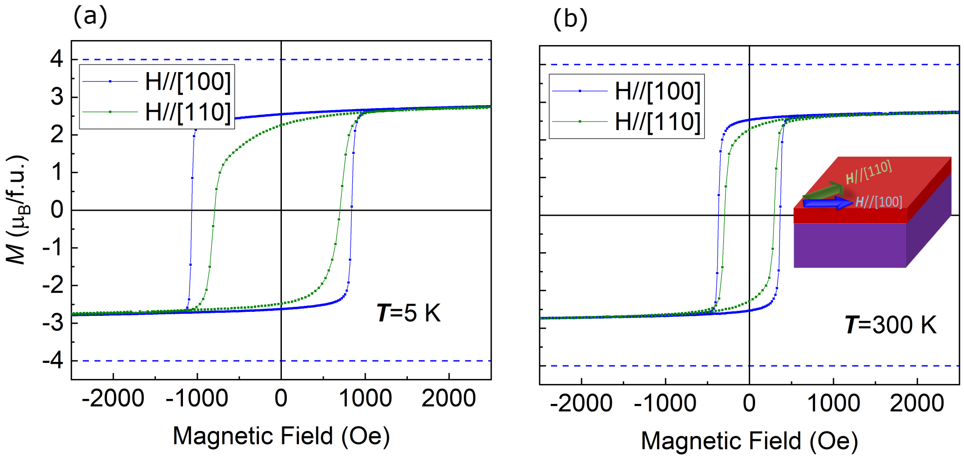

Figure 4.18: The hysteresis loops of compressive strained Fe_3O_4 film ($T_{growth} = 350\,°C$) measured with an external magnetic field applied along [100] (blue) and [110] (green) directions at different temperatures (a) 5 K and (b) 300 K.

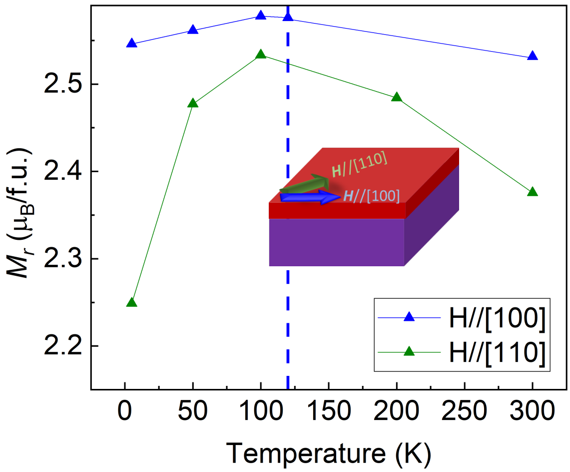

Figure 4.19: The remanent magnetization M_r for the compressively strained Fe_3O_4 film ($T_{growth} = 350\,°C$) as a function of the temperature measured with an external magnetic field applied along [100] (blue) and [110] (green).

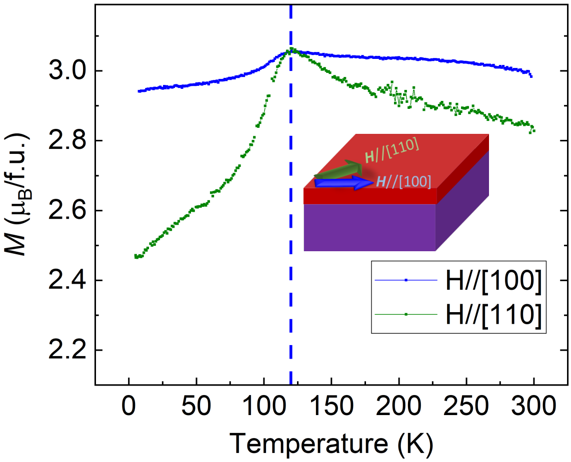

Figure 4.20: Magnetization vs. temperature of the compressively strained Fe_3O_4 film ($T_{growth} = 350\,°C$) measured in ZFC mode with an external magnetic field applied along the [100]- (blue) and [110]- (green) direction.

transition is [100]. In addition, the [110] axis is the hard axis above T_V and even harder below T_V (10 % suppressed magnetization).

At room temperature, the easy axis directions are switched by 45° to the [100] direction in comparison by the bulk magnetite easy axis [110]. This observation was explained by the particular distribution of anti-phase boundaries (APBs) and the antiferromagnetic coupling [122]. At $T < T_V = 120\,K$, the easy axis is along the [100] direction which is similar to the bulk monoclinic magnetite easy axis [100]. This suggests that either (1) the effect of the antiferromagnetic coupling of APBs is suppressed or (2) another contribution induced by the substrate, i.e. that the Fe_3O_4 lattice distortion (compressive strain) is dominant.

Verwey transition

The $M(T)$ curve of the compressively strained Fe_3O_4 film ($T_{growth} = 350\,°C$) measured in zero-field cooling mode with an applied field of 500 Oe along the [100]- and [110]-direction has been measured (Figure 4.20). The magnetization measured along the [100] decreases with 3 % below the $T_V = 120\,K$. However, the magnetization measured along the [110] decreases with 17 % below the T_V. This suggests that the in-plane easy axis direction is the [100] below and above the T_V.

4.5.4 Discussion

Ideally, the cubic Fe_3O_4 thin film has a magnetic easy axis direction along [110] at room temperature and the monoclinic Fe_3O_4 has a magnetic easy axis direction along [100] at a temperature below the Verwey transition.

Our Fe_3O_4 films grown on $SrTiO_3$ substrates are strained (tensile or compressive). At room temperature, all films show a switched easy axis direction by 45° to [100], which may be attributed to the particular arrangement of APBs caused by the $SrTiO_3$ substrate [122]. At temperature below the Verwey transition, we observe two different behaviors:

- For the tensile strained film, the magnetic easy axis is oriented along the [110] direction which suggests the extended effect of the antiferromagnetic coupling of the APBs at the low-temperature regime.
- For the compressively strained film, the magnetic easy axis remains along the [100]. Here, we have two aspects: (a) the reordering of the APBs; consequently, they do not affect the magnetic easy axis direction, and (b) the structural transition from the distorted cubic to distorted monoclinic, which results in an in-plane anisotropy along [100] direction above and below the Verwey transition (magnetostriction anisotropy).

The magnetic behaviour at the low temperature of the two films with tensile and compressive strain is different which can only be related to the strain effect, however, additional experiments are needed to prove this observation.

4.6 Conclusion

In this chapter, we discussed the effect of the growth temperature on the different properties of the Fe_3O_4 films grown on the $SrTiO_3$ substrates by pulsed laser deposition (PLD). The films were investigated by the lab facilities: AFM, XRR, XRD, and VSM, in addition to, the synchrotron techniques: HAXPES and XMCD. We observed the lowering of the surface roughness with increasing growth temperature, which indicates layer by layer growth. All the films grown at different temperatures have high crystallinity (XRD) and chemical stoichiometry (HAXPES and XMCD). However, they have different out-of-plane lattice constants: (I) tensile strain ($T_{growth} = 500\,°C$), (II) absence of strain (relaxed growth) ($T_{growth} = 400\,°C$) and (III) compressive strain ($T_{growth} = 350\,°C$). Therefore, their magnetic properties are influenced by the growth temperature. At room temperature, the magnetic easy axis is along the [100] direction and is strain independent. This does not coincide with the known thin film easy axis of magnetite [110]. It is attributed to the particular arrangement of the APBs caused by the $SrTiO_3$ substrate. At temperature below the Verwey transition T_V, the magnetic easy axis switches between [110] and [100] direction depending on the strain. For the tensile strained film ($T_{growth} = 500\,°C$), the easy axis is along [110]. However, for the compressive strained film ($T_{growth} = 350\,°C$), the easy axis is along [100]. The epitaxial strain distorts the tetrahedral and octahedral sites of the Fe_3O_4 thin films, which affects the magnetic anisotropy. This means that with careful optimization for growth temperature and substrate choices (Nb:STO), we can tune the magnetic anisotropy properties of the thin films.

So far, other aspects may affect the magnetic properties, in particular, the reduced dimensionality and the properties of the $Fe_3O_4/SrTiO_3$ interface. In the next step, we investigate the electronic and magnetic properties of films with reduced thicknesses down to 2 nm using bulk and surface-sensitive spectroscopic techniques, HAXPES and XMCD.

CHAPTER 5

Tunable ferri-magnetic phases at $Fe_3O_4/SrTiO_3$ oxide interfaces

> The presented results in this chapter are taken from the published paper *"Tunable Magnetic Phases at $Fe_3O_4/SrTiO_3$ Oxide Interfaces"*: Mai Hussein Hamed, Ronja Anika Hinz, Patrick Lömker, Marek Wilhelm, Andrei Gloskovskii, Peter Bencok, Carolin Schmitz-Antoniak, Hebatalla Elnaggar, Claus M. Schneider and Martina Müller, ACS Applied Materials & Interfaces, 2019, **11**, 7, 7576-7583 [124].

In Chapter 4, we investigated the effect of growth temperature on the surface morphology and the magnetic properties of $Fe_3O_4/SrTiO_3$ heterostructures. In this chapter, we focus on the influence of reduced film thicknesses down to 2 nm on the magnetic and electronic properties of $Fe_3O_4/SrTiO_3$ heterostructures. Previous studies suggested the formation of a reduced antiferromagnetic FeO phase at the interface of $Fe_3O_4/SrTiO_3$ heterostructures by investigating the magnetic and structural properties using vibrating sample magnetometer and transmission electron microscopy [79, 81]. However, in this chapter, we investigate the properties of the $Fe_3O_4/SrTiO_3$ heterostructures by several techniques. The magnetic properties of the $Fe_3O_4/SrTiO_3$ heterostructures are studied by a vibrating sample magnetometer (Section 5.2). Additionally, synchrotron-based spectroscopies have been used to precisely understand the interfacial properties (Sections 5.3 and 5.4). In contradiction to the literature [79, 81], using the chemical and magnetic structure techniques, HAXPES and XMCD, we observe a reduction of Fe^{2+} ions with decreasing film thickness, accompanied by an increase of Fe^{3+} ions in both tetrahedral and octahedral sites, and conclude on the formation of a magnetically active ferrimagnetic 2 u.c. γ-Fe_2O_3 intralayer. By understanding the properties of the interfaces and the mechanisms behind the intralayer formation, we find a route to control and tune the magnetic properties of the oxide interfaces (Section 5.6).

5.1 PLD growth conditions

Magnetite films with thicknesses between 2 and 38 nm have been grown on conductive 0.1 % Nb-doped $SrTiO_3$ (001) TiO_2-terminated substrates by pulsed laser deposition (PLD). The substrate temperature was kept at 400 °C, as we discussed in Chapter 4 that the films grown at this temperature are fully relaxed and bulk like Fe_3O_4 films. The oxygen partial pressure was kept at 2×10^{-6}mbar. The laser fluence was set to 1.5 J/cm^2 with a repetition rate of 5 Hz producing ionized particles from a Fe_2O_3 rotating target.

5.2 Structural and magnetic characterization

5.2.1 Experimental details

The film thicknesses and interface- and surface roughness were examined by X-ray reflectivity (XRR) using a Philips XPert MRD with CuK_α-radiation. Bulk magnetic properties were investigated by a vibrating sample magnetometer (VSM) using a Quantum Design Dynacool physical properties measurement system (PPMS). Magnetic moment versus temperature $M(T)$ was measured in zero-field cooling (ZFC) mode with 500 Oe applied field. Hysteresis loops were recorded at a magnetic field of $H = \pm 5$ T along the in-plane [100]-axis.

5.2.2 Structural properties

The structural properties of the thickness dependant Fe_3O_4/Nb:$SrTiO_3$ (001) heterostructures were investigated by X-ray diffraction (XRD). XRD surveys were measured with a range of $2\theta = 15°$-$110°$. All surveys show the four reflections of the $SrTiO_3$ (001) substrate. At $2\theta \approx 43°$ and $2\theta \approx 95°$, additional peaks appear, corresponding to the Fe_3O_4 (004) and (008) reflections. This indicates the epitaxial growth of Fe_3O_4 films along the (001) direction.

Detailed out-of-plane θ-2θ scans around the $SrTiO_3$ (002) and Fe_3O_4 (004) reflections were measured with a range of $2\theta = 40°$-$50°$. All XRD scans are normalized to their $SrTiO_3$ (002) reflection as shown in Figure 5.1. Three findings can be identified:

(1) The broadening of the peaks of Fe_3O_4 (004) reflections with decreasing film thickness. From Bragg's law, it can be extracted that the width is inversely proportional to the film thickness. Thus, the broadening is expected.

(2) The peak intensities of the Fe_3O_4 (004) reflections decrease with decreasing film thickness. This can be explained by the smaller amount of material that contributes to the coherent diffraction.

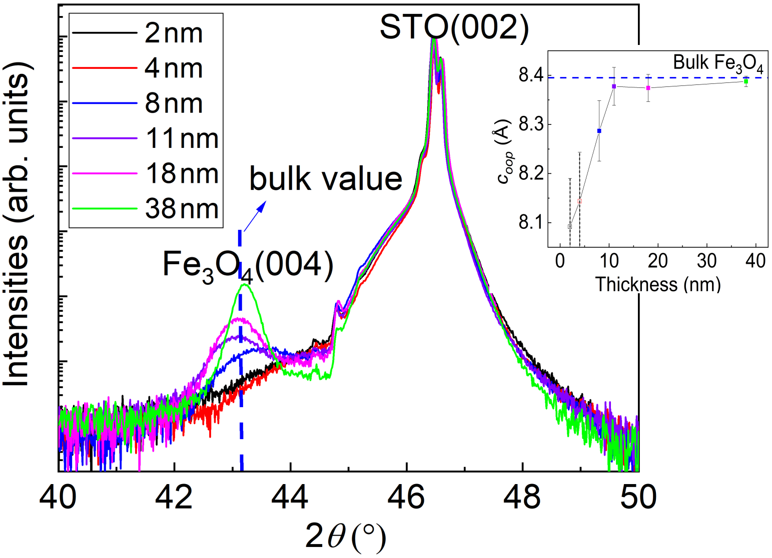

Figure 5.1: X-ray diffraction θ-2θ scans of the $SrTiO_3$ (002) and the Fe_3O_4 (004) reflections of films with varying thickness of 2-38 nm. In the inset, the out-of-plane lattice constant c_{oop} of the Fe_3O_4 films as a function of the film thickness.

(3) The peaks positions of Fe_3O_4 films are shifted to larger angles with decreasing the film thickness. The strongest shifts are detected for the peaks positions of 2 and 4 nm films.

In the inset of Figure 5.1, the out-of-plane lattice constant c_{oop} of the Fe_3O_4 films with thicknesses $d > 11$ nm is close to the bulk lattice constant of Fe_3O_4. Unexpectedly, the c_{oop} decreases to 8.287 Å for a Fe_3O_4 film with a thickness of $d = 8$ nm. This means that the in-plane-lattice constant is 8.4495 Å to preserve the unit cell size of Fe_3O_4. The $SrTiO_3$ substrate is expected to apply a compressive strain and thereby enlarge the out-of-plane lattice constant of the Fe_3O_4 films. As a result, the in-plane lattice constant is expected to decrease ideally to 7.81 Å (double $SrTiO_3$ unit cell), in particular for ultrathin films. This is not the case for our films. Explanations which support our results are:

(1) The Fe_3O_4 unit cell attempts to fit itself on three $SrTiO_3$ unit cells, not on two. Thus, the in-plane lattice constant of Fe_3O_4 increases and, consequently, the out-of-plane lattice constant decreases.

(2) Both the in-plane and out-of-plane lattice constants decrease with decreasing film thickness, which leads to the reduction of the unit cell volume. Thus, the films may show an auxetic behavior with a negative Poisson ratio (ν). This reduction in the unit cell size has been reported for different ferrites, $NiFe_2O_4$ [125] and $CoFe_2O_4$ [126] grown on $SrTiO_3$ substrates.

(3) Different iron oxide phases that emerge at the interface between the Fe_3O_4 films and the $SrTiO_3$ substrates. Those phases may have different structural properties which we study in the following by HAXPES experiments.

To give a precise explanation of the out-of-plane lattice constant changes of the ultrathin films, further studies are needed.

5.2.3 Saturation magnetization

In order to determine the saturation magnetization of the films, hysteresis loops (magnetization versus magnetic field $M(H)$) have been measured. Hysteresis loops were recorded at a temperature of 5 K. The diamagnetic contribution from the $SrTiO_3$ substrate has been corrected as we discussed in Section 3.2.3. The hysteresis loops for the films with different thicknesses are depicted in Figure 5.2 (a). The saturation magnetization decreases with decreasing film thickness (Figure 5.2 (b)), and the coercivity increases (Figure 5.2 (c)). The magnetization of the films is saturated at a magnetic field of 1.2 T. The saturation magnetizations of the films are decreasing from 3.3±0.2 μ_B/f.u. for 38 nm thick film to 1.03±0.05 μ_B/f.u. for 2 nm thick film. Furthermore, the coercivity increases to 1400 Oe for 2 nm thick film, which may indicate the structural dislocations and formation of antiferromagnetic anti-phase boundaries. On the other hand, decreasing the saturation magnetization of the films to 1 μ_B/f.u. cannot be explained by only the structural dislocations and formation of antiferromagnetic anti-phase boundaries. Instead, there must be a magnetic phase transition that occurs at the interfaces as we will discuss in Section 5.4.

5.2.4 Verwey transition

In order to determine the Verwey transition T_V of the Fe_3O_4 films grown with different thicknesses, $M(T)$ measurements of the films were performed in zero-field cooling (ZFC) mode with an applied field of 500 Oe. In Figure 5.3 (a), the normalized $M(T)$ curves of 2-38 nm thick Fe_3O_4 films are shown. For 38 nm thick film, the magnetization drops at a temperature of 117 K, which represents the Verwey transition T_V. This drop shifts towards lower temperatures when reducing the film thickness. We determine the values of T_V by extracting the maximum of $\partial M/\partial T$ shown in Figure 5.3 (b). The transition width ΔT_V is determined by the $\partial^2 M/\partial T^2$ (Figure 5.3 (c)).

For Fe_3O_4/MgO heterostructures with a 0.32 % lattice mismatch, many studies reported that T_V decreases with decreasing film thickness. However, it was hardly detected for magnetite films thinner than 10 nm [111, 112, 116, 117]. Studies on Fe_3O_4/STO with a −7.5 % lattice mismatch did not report a Verwey transition in films thinner than 17 nm [81, 111, 115]. For the Fe_3O_4 thickness series of $d = 2$-38 nm, T_V and $\Delta T(d)$ are depicted in Figure 5.3 (d). T_V decreases with film thickness as observed for Fe_3O_4/MgO [111, 112, 116, 117], yet the Verwey transition is still observable in our ultrathin Fe_3O_4 films of 2 and 4 nm thickness. The Verwey transition T_V of the Fe_3O_4 films with a thickness

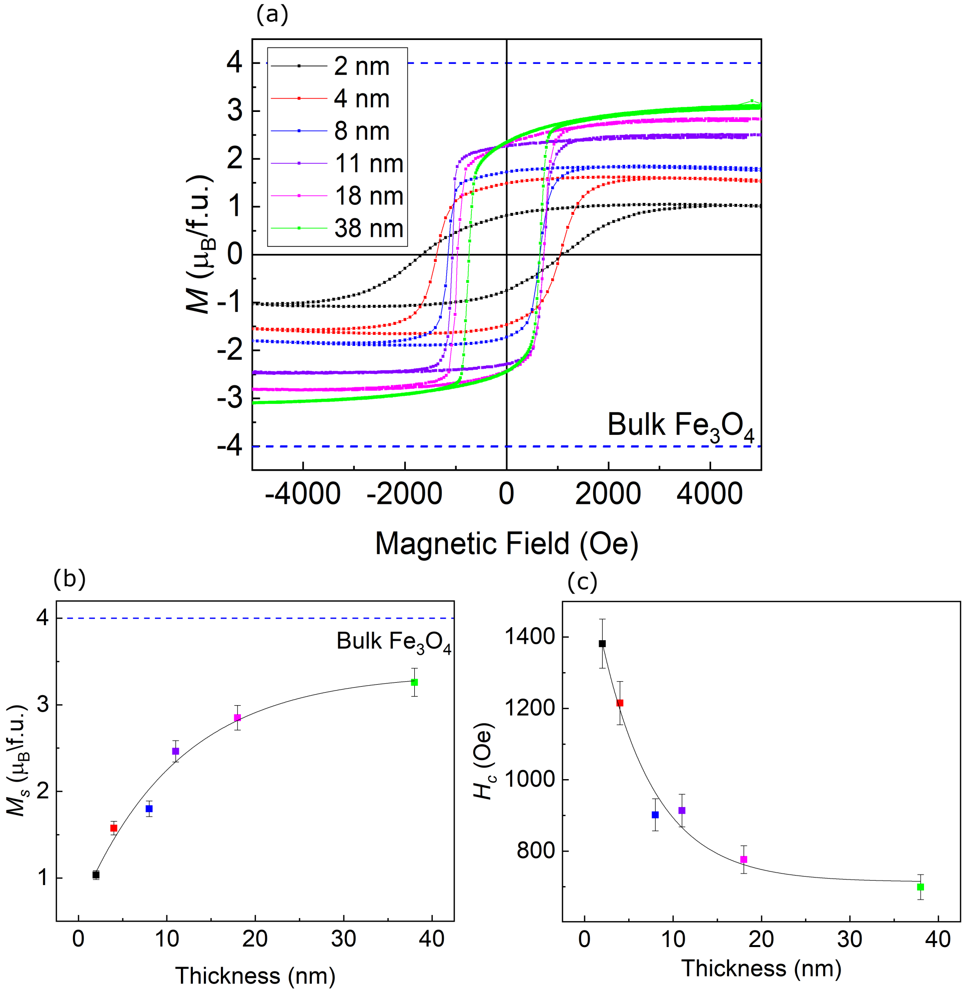

Figure 5.2: (a) Hysteresis loops for the Fe_3O_4 films with thickness $d = 2$-38 nm recorded at a temperature of 5 K. The calculated values of (b) the saturation magnetization M_S and (c) the coercivity H_c for the Fe_3O_4 films as a function of their thickness. The blue dashed lines indicate the bulk values for the saturation magnetization of $4\,\mu_B$/f.u..

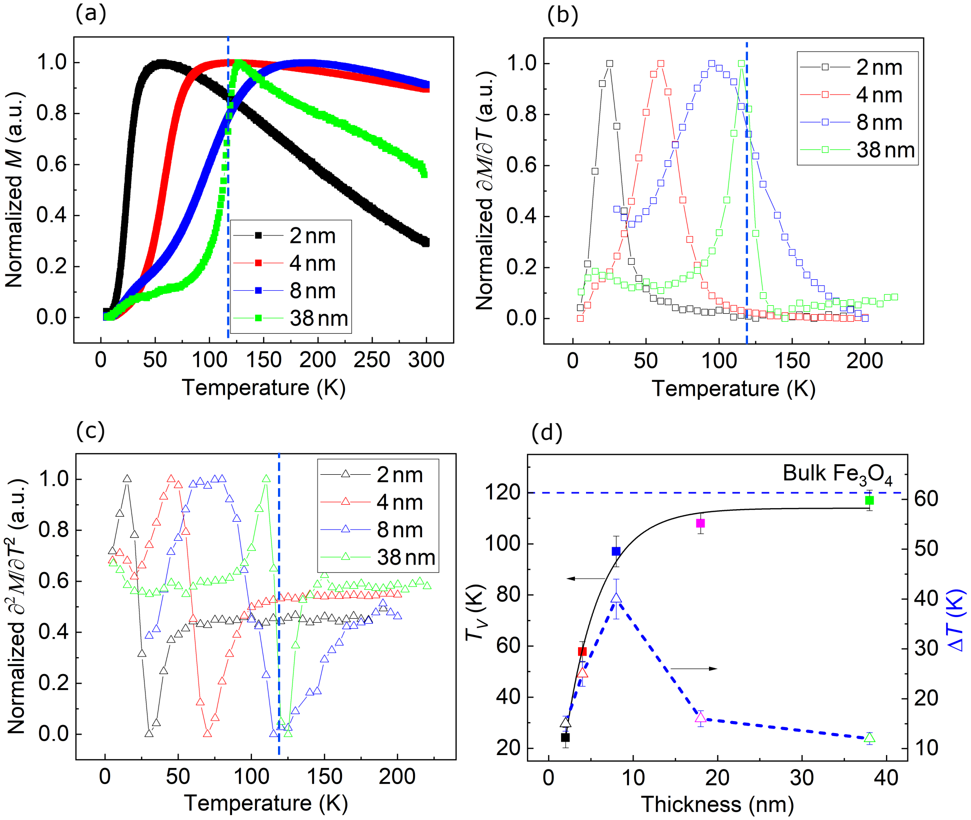

Figure 5.3: Magnetic detection of Verwey transition of Fe_3O_4 thin films grown with different thicknesses: (a) Magnetization vs. temperature $M(T)$. (b) The first and (c) second derivatives for the magnetization curve. (d) Verwey transition temperature T_V and transition width ΔT_V as a function of film thickness.

range from 38 nm to 8 nm decreases slowly. However, T_V of the Fe_3O_4 films with a thickness range from 8 nm to 2 nm decreases strongly to 25 K for a 2 nm thick film. The decrease of T_V may be caused by the reduction of domain sizes [111]. The transition width ΔT_V (dashed blue line) shows an inflection point at 8 nm Fe_3O_4 film thickness. The strain and growth defects may cause the broadening of the transition ΔT_V at lower film thicknesses [127]. However, the sharpness of the transition for the ultrathin films (2 and 4 nm) indicates an emergent phenomenon at the interfaces of $Fe_3O_4/SrTiO_3$ systems (for example, oxidized-reduced magnetic phase).

In summary, the saturation magnetization, as well as the Verwey transition are decreasing with decreasing Fe_3O_4 film thickness. This needs a further understanding of the interface properties. In order to investigate the impact of the interfaces of the $Fe_3O_4/SrTiO_3$ heterostructures on the chemical and magnetic properties, depth- and element-selective-magnetic studies will be discussed in the following sections.

5.3 Buried $Fe_3O_4/SrTiO_3$ interface

5.3.1 Experimental details

Element-selective and depth-dependent chemical information of the films and buried interfaces were analyzed by hard X-ray photoelectron spectroscopy (HAXPES) at PETRA III (DESY, Hamburg). The information depth depends on the photon energy and the inelastic mean free path λ. For Fe_3O_4 and a photon energy of $h\nu = 4\text{-}6\,\text{keV}$ the information depth is approximately 20-30 nm.

5.3.2 HAXPES

In this section, we identify the chemical structure of the ultrathin Fe_3O_4 films and the interfaces to the $SrTiO_3$ substrates using HAXPES. Figure 5.4 (a) shows Fe 2p core level spectra of the 2, 4, 8 and 38 nm thick Fe_3O_4 films. To identify the Fe_3O_4 films' chemical properties, the experimental spectra were compared to the reference spectra of FeO, Fe_2O_3 and Fe_3O_4 [61, 62]. A well-known feature to identify the particular Fe oxides is the satellite peak as shown in Figure 5.4 (a). For $Fe^{II}O$ and $Fe_2^{III}O_3$, the satellite's binding energies are 715.5 eV and 719 eV, respectively, which can be easily distinguished by lab-XPS (resolution: $\Delta E = 0.8\,\text{eV}$) and HAXPES ($\Delta E = 0.2\,\text{eV}$). For Fe_3O_4, which has a mixed oxidation state of Fe^{2+} and Fe^{3+}, the satellites of both states merge (Figure 5.4 (a)). For 38 nm thick Fe_3O_4, we find that the two satellites are indeed merged. Moreover, the Fe $2p_{3/2}$ core level depicted in Figure 5.4 (b) is composed of the Fe^{3+} peak and a shoulder that refers to Fe^{2+}. Consequently, we observe a bulk-like stoichiometry in 38 nm thick Fe_3O_4 films.

In order to investigate the buried $Fe_3O_4/SrTiO_3$ interfaces, HAXPES was conducted for $d = 2$, 4 and 8 nm films, shown in Figure 5.4 (a). We observe that the Fe^{3+} satellite peak

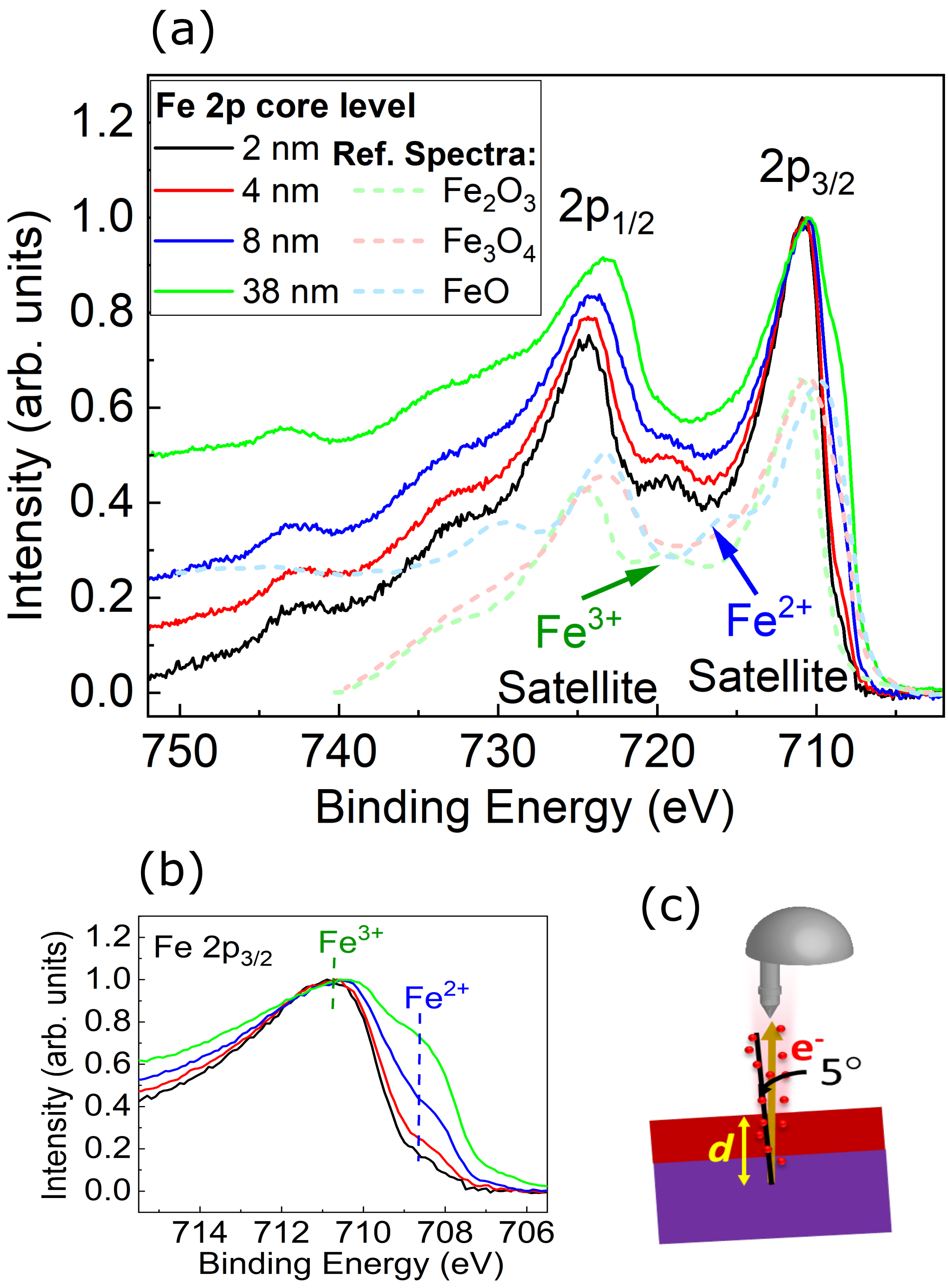

Figure 5.4: (a) Fe 2p core level spectra of Fe_3O_4 films with different thicknesses grown on $SrTiO_3$ substrates recorded using a photon energy of $h\nu = 6\,\mathrm{keV}$ and reference spectra [61, 62]. (b) Fe $2p_{3/2}$ core level. (c) Schematics of the experimental geometry.

appears for the 8 nm film and its intensity enhances with decreasing Fe_3O_4 thickness. This enhancement is accompanied by a decrease of the Fe $2p_{3/2}$ peak's shoulder, which is an indication for Fe^{2+}. Both observations imply the formation of the Fe_2O_3 phase in addition to Fe_3O_4. The fact that we do not observe these features for $d = 38$ nm suggests that the modification of the chemical properties from Fe_3O_4 to Fe_2O_3 occurs at the Fe_3O_4/$SrTiO_3$ interface. To clarify this hypothesis, angle-dependent HAXPES is performed.

5.3.3 Angle-dependent HAXPES

Figure 5.5 (a) and (b) illustrate the angle-dependent HAXPES experiment conducted on 8 nm thick film using both a normal emission $\theta = 5°$ (interface sensitive) and grazing emission $\theta = 60°$ (surface sensitive) geometry. The Fe^{3+} satellite peak intensity reduces at $\theta = 60°$ measurement, whereas the Fe^{2+} shoulder of Fe $2p_{3/2}$ core level peak is enhanced. In contrast to previous studies [79, 81], which claimed the formation of the interfacial FeO layer for the Fe_3O_4/$SrTiO_3$ heterostructures, our findings point toward the formation of an interfacial Fe_2O_3 phase. In particular, α-Fe_2O_3 crystallizes in a corundum structure with antiferromagnetic properties, whereas γ-Fe_2O_3 is a defected ferrimagnetic spinel with a saturation magnetization of $M_s = 2.5\,\mu_B$/f.u..

In order to reveal which interfacial Fe_2O_3 phase is likely formed, we apply XMCD to distinguish between ferrimagnetic and antiferromagnetic properties.

5.4 Interface magnetic properties

5.4.1 Experimental details

Element- and magnetic site-selective X-ray absorption spectroscopy (XAS) and X-ray magnetic circular dichroism (XMCD) were performed at Diamond Light Source (Didcot, UK) at beamline I10 (BLADE) with the photon energy ranging from 0.4 to 2 keV. A near-grazing emission geometry $\theta = 80°$ has been used, with 1 T magnetic field and 10K temperature. XAS spectra were recorded in total electron yield mode (TEY) by measuring the sample drain current. Four absorption spectra were taken for each sample using the left (+) and right (-) -handed circular polarization (+ - - +).

5.4.2 XAS and XMCD

In this section, we determine the element-specific magnetic properties of the Fe_3O_4/$SrTiO_3$ interface. The XAS fine structure strongly differs for α-Fe_2O_3 and γ-Fe_2O_3 [91]. The average XAS spectrum is calculated by averaging the four polarized absorption spectra (+ - - +). XAS spectra of Fe $L_{2,3}$-edge of Fe_3O_4 films with different thicknesses are shown

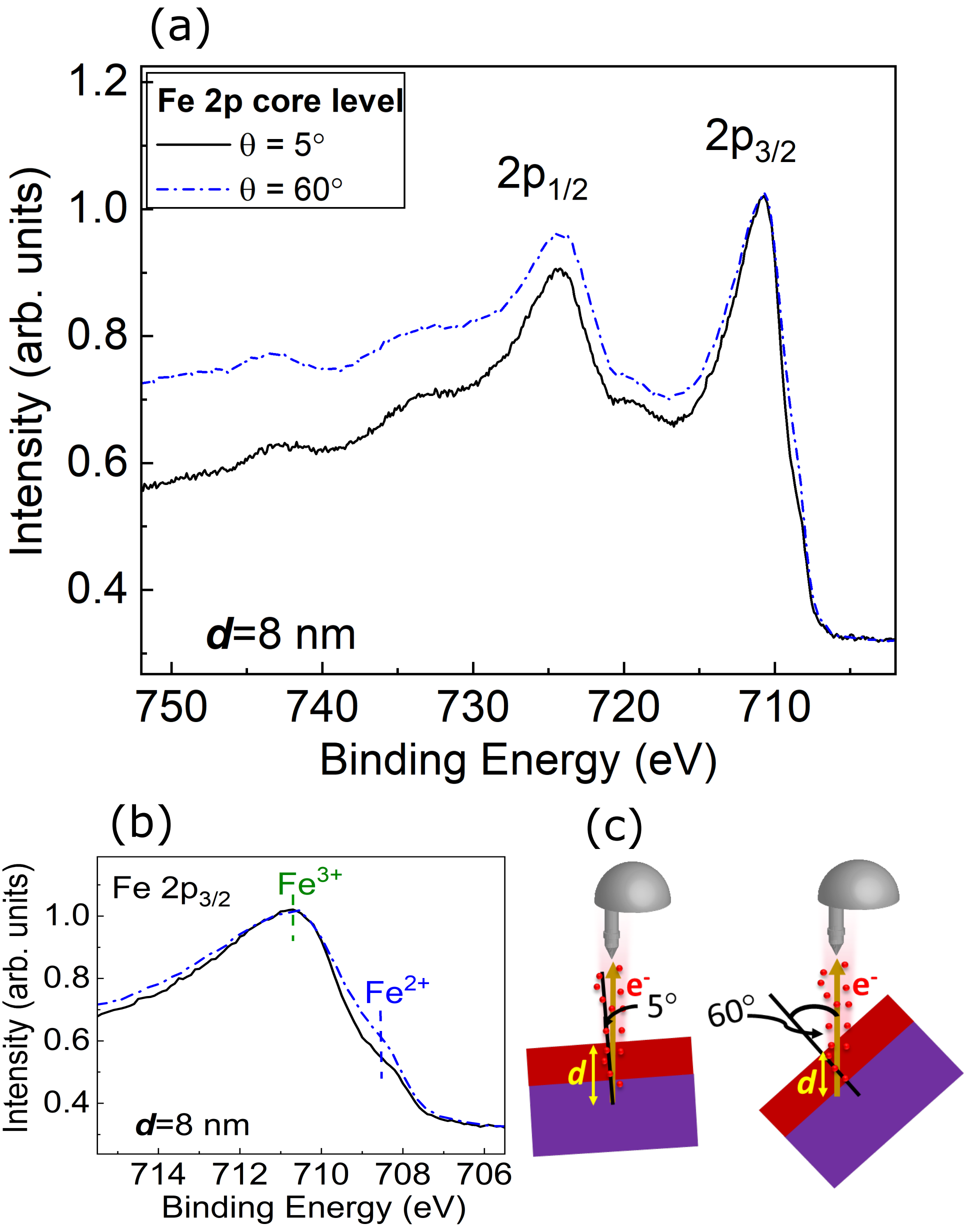

Figure 5.5: (a) Fe 2p core level of 8 nm thick Fe_3O_4 film, recorded using $\theta = 5°$- and 60°- emission geometry using a photon energy of $h\nu = 4\,\text{keV}$. (b) Fe $2p_{3/2}$ core level. (c) Schematics of the experimental geometry.

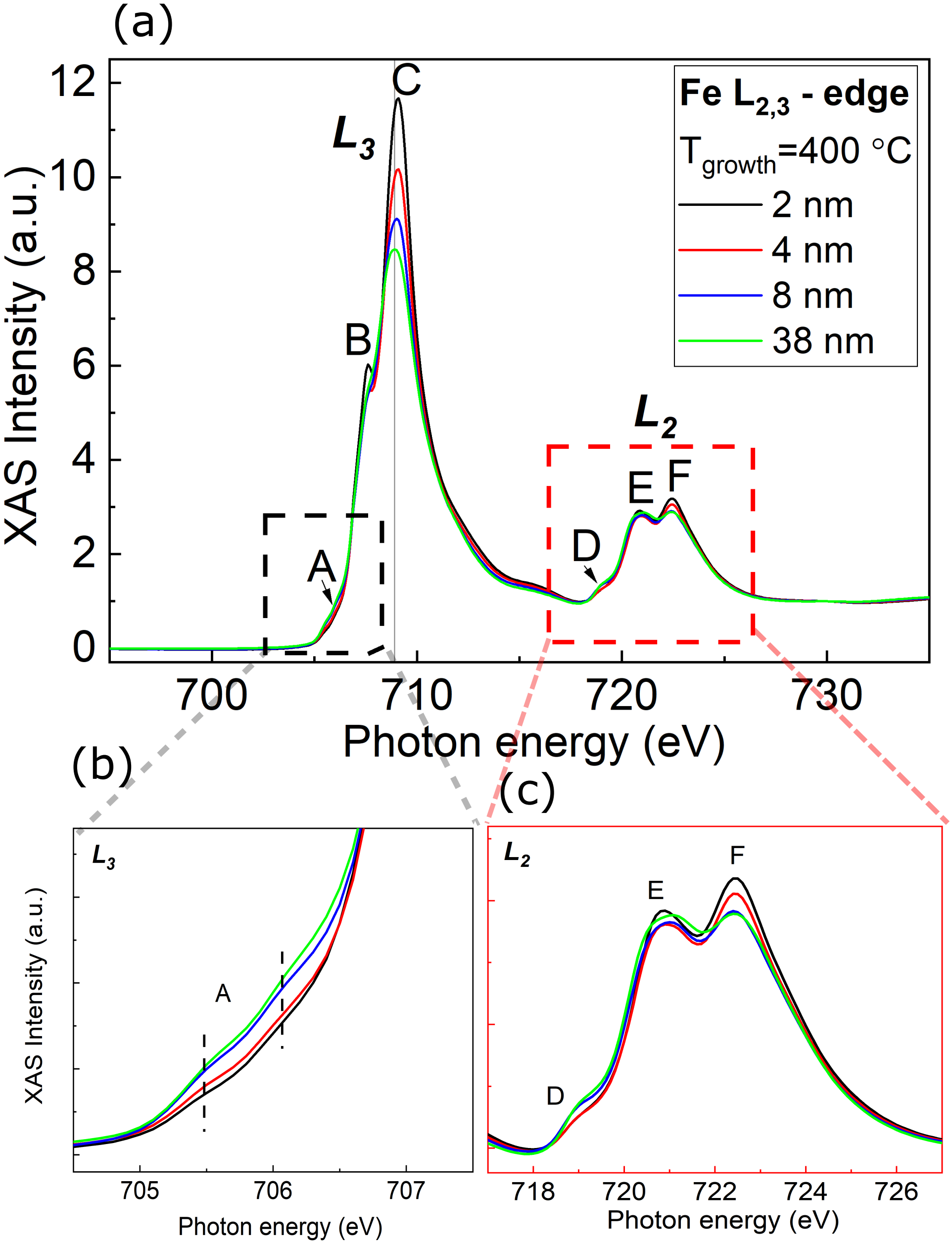

Figure 5.6: (a) Fe $L_{2,3}$-edge XAS spectra of Fe_3O_4 films with varying thicknesses, (b) L_3 edge XAS fine structure and (c) L_2 edge XAS fine structure.

in Figure 5.6. The pre-edge peaks A and D are mainly related to $Fe^{2+}_{O_h}$. The peak intensities reduce with decreasing film thickness. The peaks B, C, E and F originate from mixed contributions from $Fe^{2+}_{O_h}$, $Fe^{3+}_{T_d}$ and $Fe^{3+}_{O_h}$ sites. We observe that both altered intensity ratios and different energy positions indicate a change in the Fe^{2+} and Fe^{3+} ratios with film thickness. The observed alteration of their ratios confirms a redistribution of Fe cations. We conclude from these findings, that the absorption fine structure indicates the presence of Fe_2O_3 at the interface. To reveal which interfacial Fe_2O_3 phase is formed, i.e., the antiferromagnetic α-Fe_2O_3 or the ferrimagnetic γ-Fe_2O_3 phase, we apply XMCD to distinguish between the magnetic properties.

Figure 5.7 illustrates the Fe $L_{2,3}$-edge XMCD spectra of Fe_3O_4 films with different thicknesses. At the L_3 edge (Figure 5.7 (b)), the two pre-edge peaks, a and b, originate mainly from $Fe^{2+}_{O_h}$. Their peak intensities decrease with decreasing thickness. The peaks c, d and e are well-known fingerprints for distinguishing Fe_3O_4 from γ-Fe_2O_3 [92, 93]. The $Fe^{2+}_{O_h}$ (c peaks) and $Fe^{3+}_{O_h}$ (e peaks) are ferromagnetically coupled (negative XMCD L_3 edge) and antiferromagnetically coupled to $Fe^{3+}_{T_d}$ (d peaks) (positive XMCD L_3 edge). We explained in detail the reason for switching of XMCD sign between the tetrahedral and octahedral sites in Section 3.3.7. The intensity ratio between the c and e peaks I_c/I_e equals 1.5 and 0.4 for Fe_3O_4 and γ-Fe_2O_3, respectively [92]. For the 38 nm thick film, I_c/I_e nearly equals 1.5. The ratio decreases continuously with decreasing film thickness to $I_c/I_e = 0.6$ for a 2 nm thick film. The change in the XMCD L_3 edge indicates that there is a magnetic phase at the interface. This supports the formation of the ferrimagnetic γ-Fe_2O_3 phase, rather than the antiferromagnetic α-Fe_2O_3 phase. Furthermore, the L_2 edge XMCD (Figure 5.7 (c)) reflects the mixed state of Fe_3O_4 and γ-Fe_2O_3. The peak f corresponds to $Fe^{2+}_{O_h}$ and decreases with decreasing thickness. The peak g corresponds to $Fe^{2+}_{O_h}$, $Fe^{3+}_{T_d}$ and $Fe^{3+}_{O_h}$. It splits into two small peaks for the 2 nm thick film. The h peak corresponds to $Fe^{3+}_{T_d}$, and its intensity increases with decreasing thickness. The XMCD fine structure of the L_2 edge reflects the formation of γ-Fe_2O_3 at the $Fe_3O_4/SrTiO_3$ interface.

5.4.3 Spin and orbital moment: the sum rules

The sum rules are used to extract the spin m_{Spin} and orbital magnetic moment m_{Orb} of the interface. The spin and orbital magnetic moments are determined by the values of p, q and r according to Equations 3.3.13 and 3.3.14. The detailed procedure to extract the p, q and r from the experimental XAS and XMCD spectra is shown in Section 4.3. The spin and orbital magnetic moments as a function of the film thicknesses are given in Figure 5.8. For the 38 nm thick sample, the saturation magnetization M_S measured by VSM is of $3.3\pm0.2\,\mu_B$/f.u. (Section 5.2). However, this does not match the spin magnetic moment measured by the XMCD technique of $2.6\pm0.5\,\mu_B$/f.u., which is 80 % of M_S determined by VSM as we explained in Section 4.3. As shown in Figure 5.8, both m_{Spin} and M_S are decreasing with film thickness to $1.2\pm0.3\,\mu_B$/f.u. for 2 nm film. This is expected because γ-Fe_2O_3 has a lower ferrimagnetic magnetic moment $M_S = 2.5\,\mu_B$/f.u. than Fe_3O_4 ($M_S = 4\,\mu_B$/f.u.).

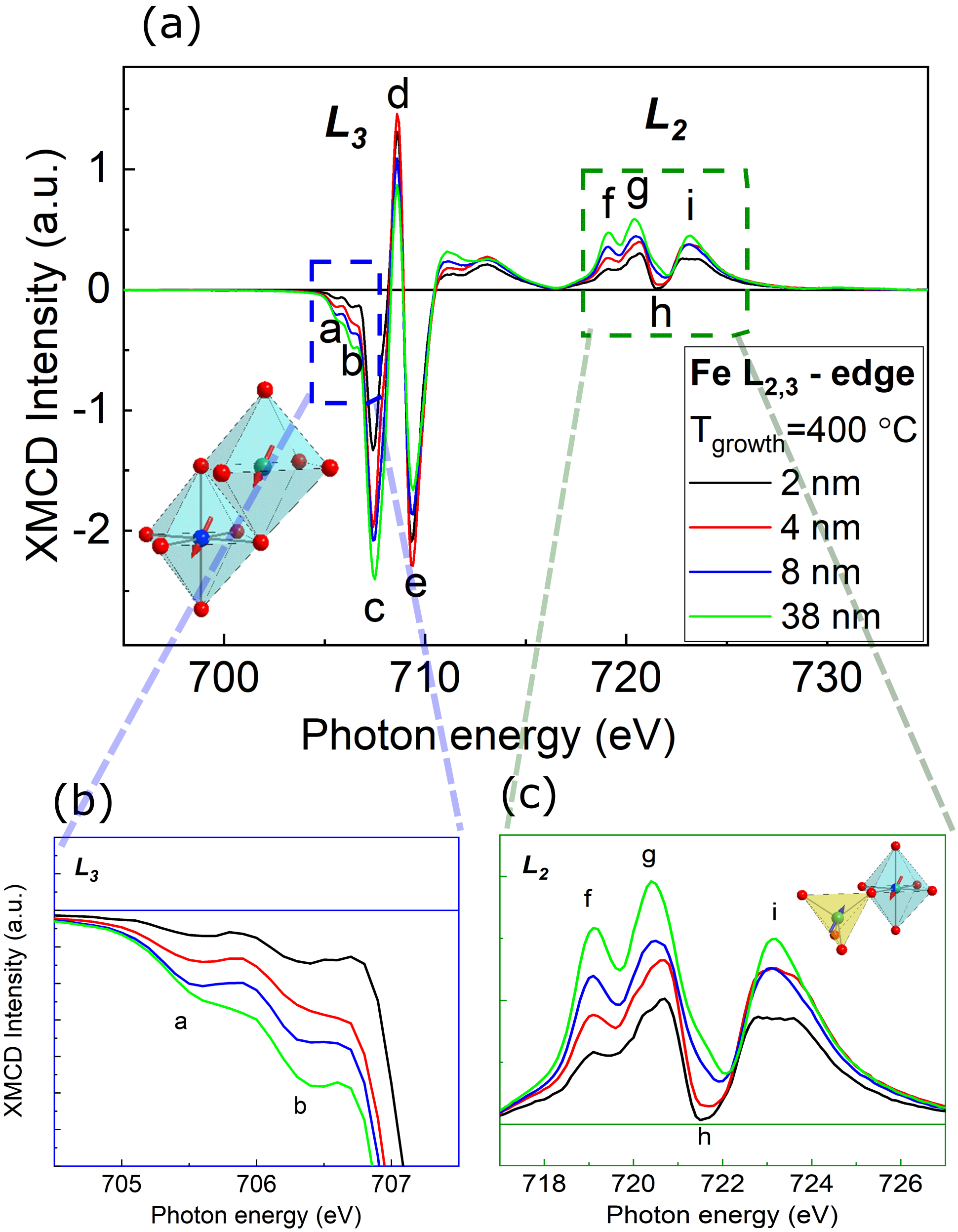

Figure 5.7: (a) Fe $L_{2,3}$-edge XMCD spectra of Fe_3O_4 films with varying thickness measured at a magnetic field of 1 T and temperature 10 K, (b) L_3 and (c) L_2 edge XMCD fine structure, respectively.

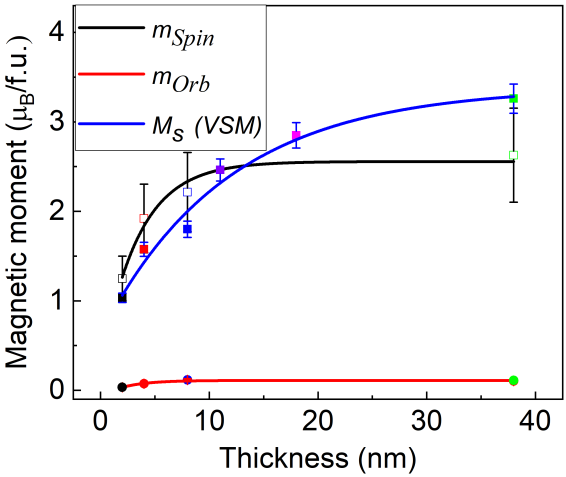

Figure 5.8: Spin and orbital magnetic moments calculated from XMCD spectrum compared to M_S measured by VSM for varying film thickness.

5.4.4 Interface magnetic thickness

To identify the magnetic thicknesses of γ-Fe_2O_3 and Fe_3O_4, XMCD calculations are performed. The XMCD calculations are divided into three steps. First, we calculate model spectra of Fe $L_{2,3}$ edge XAS and XMCD of $Fe^{2+}_{O_h}$, $Fe^{3+}_{O_h}$, and $Fe^{3+}_{T_d}$ using the CTM4XAS 5.5 software [75]. Second, we fit the model spectra to our spectra in order to determine the quantitative $Fe^{2+}_{O_h}$, $Fe^{3+}_{O_h}$, and $Fe^{3+}_{T_d}$ cation sites occupancy. Third, using the ratios between $Fe^{3+}_{T_d}$, $Fe^{2+}_{O_h}$ and $Fe^{3+}_{O_h}$ cations, we calculate the magnetic thickness of γ-Fe_2O_3 and Fe_3O_4 phases.

1 - Model spectra simulation

We used the quantum many-body program CTM4XAS to simulate the Fe $L_{2,3}$ edge XAS and XMCD of $Fe^{2+}_{O_h}$, $Fe^{3+}_{O_h}$, and $Fe^{3+}_{T_d}$ in a crystal field approximation. They are shown in Figure 5.9. Three independent cluster calculations were done for the $Fe^{2+}_{O_h}$, $Fe^{3+}_{O_h}$, and $Fe^{3+}_{T_d}$ sites. The Hamiltonian used for the calculations has four terms: (i) Coulomb interaction, (ii) crystal field potential, (iii) spin-orbit coupling, and (iv) magnetic exchange. The main parameters used for the calculations are tabulated in Table 5.1. These parameters are obtained from previously published work on $L_{2,3}$ Fe edge of magnetite [128–130].

Table 5.1: Main parameters used for crystal field multiplet calculations.

Parameter (eV)	Fe^{2+} O_h	Fe^{3+} O_h	Fe^{3+} T_d
$10D_q$	1.26	1.26	-0.77
Exchange field	0.09	0.09	-0.09
Slater integrals (F^2_{dd},F^4_{dd})	7.68, 4.77	7.67, 5.13	7.67, 5.13

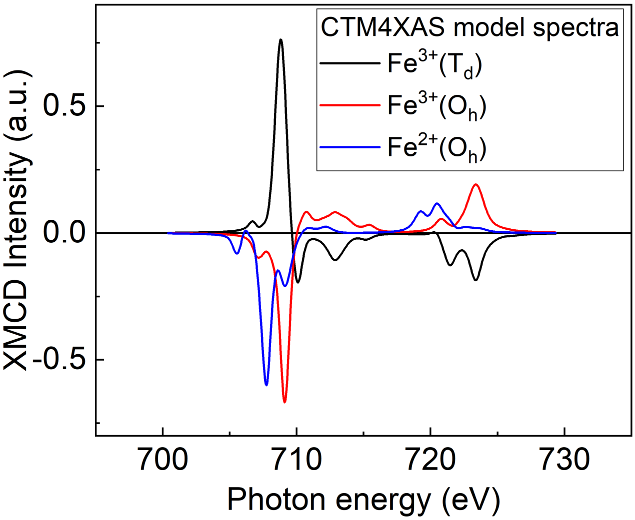

Figure 5.9: The model spectra calculated for Fe^{2+} and Fe^{3+} in both T_d and O_h sites.

2 - Fitting the experimental spectra to the model spectra

We fitted our XMCD spectra using linear combinations of the model spectra of the $Fe^{2+}_{O_h}$, $Fe^{3+}_{O_h}$, and $Fe^{3+}_{T_d}$ sites. Figure 5.10 (a-d) shows the XMCD spectra of the films with different thicknesses (blue dotted lines) in comparison with the best fit (red solid lines). From the best fit, we extract the quantitative cation sites occupancy in the films.

3 - Magnetic thickness calculations

The inverse spinel structure can be written in the form of $Fe^{3+}[Fe^{2+}_{1-3\delta}Fe^{3+}_{1+2\delta}V^{\bullet\bullet}_{O\delta}]O_4$, where $V^{\bullet\bullet}_{O}$ indicates the vacancies in O_h sites, for magnetite $\delta = 0$ and maghemite $\delta = 0.33$, respectively [93]. The thickness of Fe_3O_4 and γ-Fe_2O_3 can be calculated using the cation ratio obtained by XMCD

$$\frac{Fe^{2+}}{Fe^{3+}} = \frac{1-3\delta}{2+2\delta}. \tag{5.4.1}$$

If fractions (x) of Fe_3O_4 and $(1-x)$ of γ-Fe_2O_3 are present, they can be related as

$$(Fe_3O_4)_x + (\gamma\text{-}Fe_2O_3)_{(1-x)} = Fe_{3-\delta}O_4. \tag{5.4.2}$$

From the fractions of Fe_3O_4 and γ-Fe_2O_3, we can calculate the estimated magnetic thickness of each phase with our films.

Discussion

Accordingly, the $Fe^{2+}_{O_h}$, $Fe^{3+}_{O_h}$, and $Fe^{3+}_{T_d}$ ratios are calculated and shown in Figure 5.11 (a). Starting from the 38 nm film, the ratios for $Fe^{3+}_{T_d}$, $Fe^{2+}_{O_h}$ and $Fe^{3+}_{O_h}$ are 33.3 %, in agreement with stoichiometric Fe_3O_4, which has 1:1:1 ratio for $Fe^{3+}_{T_d}$:$Fe^{2+}_{O_h}$:$Fe^{3+}_{O_h}$. By decreasing the

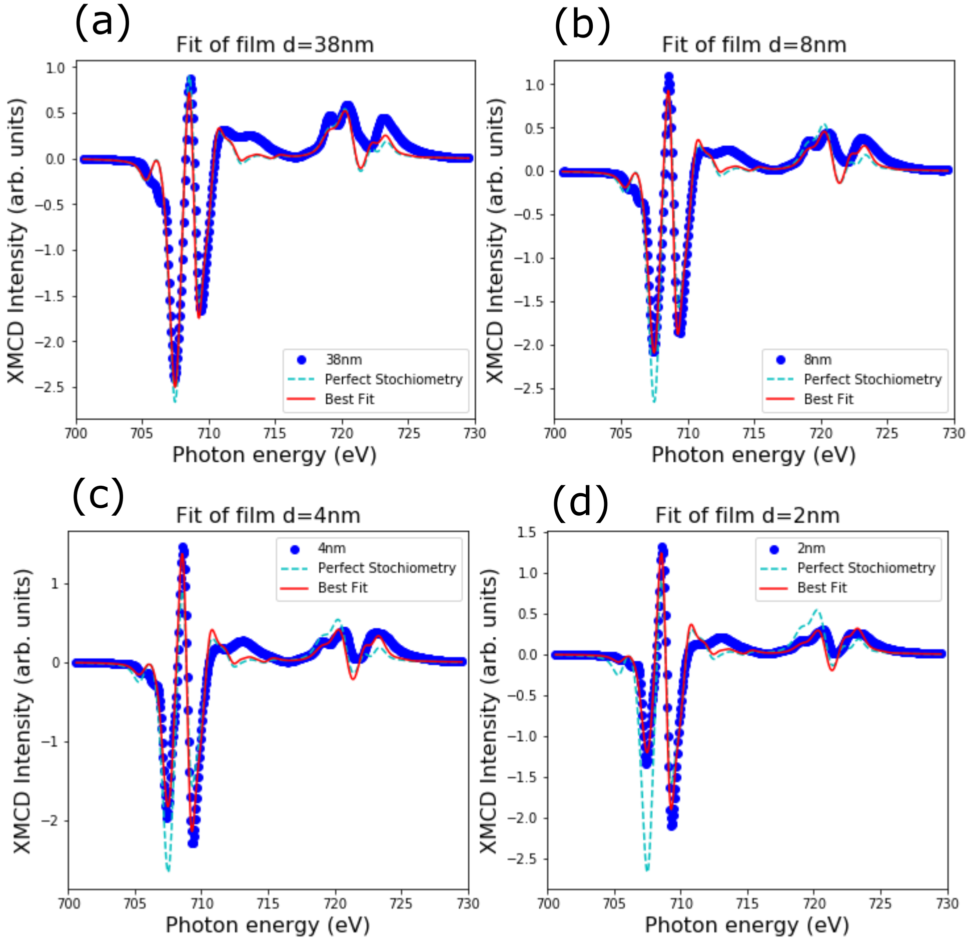

Figure 5.10: Fe $L_{2,3}$-edge XMCD spectra of Fe_3O_4 films (doted lines) and their best fit using the model spectra calculated for $Fe^{2+}_{O_h}$, $Fe^{3+}_{O_h}$, and $Fe^{3+}_{T_d}$ sites. Film thickness a) 38 nm, (b) 8 nm, (c) 4 nm and (d) 2 nm.

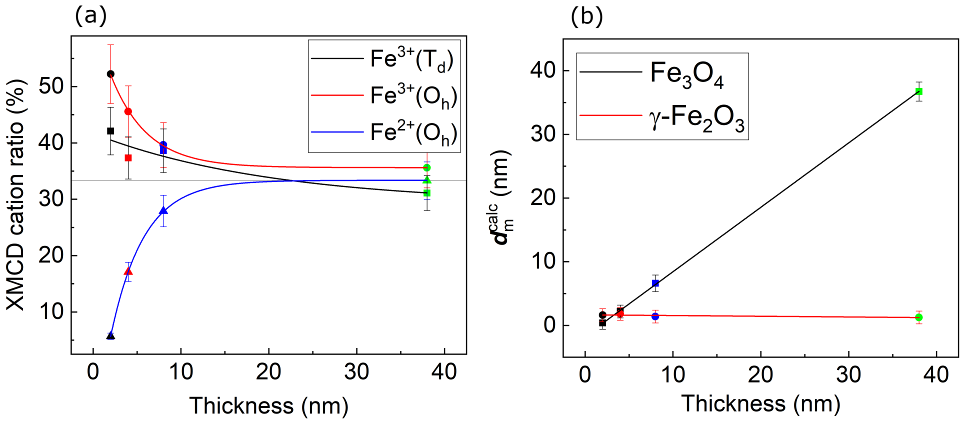

Figure 5.11: (a) Calculated $Fe^{2+}_{O_h}$, $Fe^{3+}_{O_h}$, and $Fe^{3+}_{T_d}$ XMCD cation ratios for various film thicknesses. (b) Calculated magnetic thicknesses of Fe_3O_4 and the interfacial γ-Fe_2O_3 intralayer.

Fe_3O_4 thickness, the cation ratios change. The $Fe^{2+}_{O_h}$ ratio decreases to 6 % for a 2 nm thick film, accompanied by an increase of the $Fe^{3+}_{T_d}$ and $Fe^{3+}_{O_h}$ ratios to 42 % and 52 %, respectively. Using Equations 5.4.1 and 5.4.2, we calculate the magnetic thickness d_m of the interfacial γ-Fe_2O_3 layer and Fe_3O_4, as shown in Figure 5.11 (b). On one hand, the magnetic thickness of Fe_3O_4 phase decreases with film thickness. On the other hand, the magnetic thickness of γ-Fe_2O_3 is constant. We determine a γ-Fe_2O_3 intralayer of 1.3 ± 0.3 nm which is independent of the overlaying Fe_3O_4 thickness.

5.5 Substrate-induced interface oxidation

The previously discussed characterization of the magnetic and electronic structure indicates the formation of γ-Fe_2O_3 at the interface. However, the mechanism for the formation of the interfacial γ-Fe_2O_3 phase between Fe_3O_4 film and STO substrate remains to be discussed. Taking into account the thermodynamic properties of all constituents, $SrTiO_3$ has lower Gibbs free energy of formation $\Delta G^o_F = -1500$ kJ/mol than Fe_3O_4 with $\Delta G^o_F = -1164$ kJ/mol [48]. Therefore STO is not expected to oxidize Fe_3O_4. However, oxygen vacancies perturb the formation energy of TiO_2-terminated STO [131, 132]. The Gibbs free energy of TiO_2-terminated STO with vacancies is -900 or -1039 kJ/mol [49]. Consequently, the formation of an oxidized γ-Fe_2O_3 intralayer may be explained by the oxygen diffusion from the STO substrate. The interfacial redox reactions can be considered as a reduction of the $SrTiO_3$ substrate

$$SrTiO_3 \rightleftharpoons SrTiO_{3\text{-x}} + \frac{x}{2}O_2 \quad , \tag{5.5.1}$$

and the oxidation of the Fe_3O_4 film to form an interfacial γ-Fe_2O_3 intralayer

$$Fe_3O_4 + \frac{1}{2}O_2 \rightleftharpoons \frac{3}{2}Fe_2O_3 \quad . \tag{5.5.2}$$

We note, that the reduced TiO_2-terminated $SrTiO_3$ may also indicate the reduction of Ti^{4+} at the surface. Thus, the redox mechanism may simultaneously lead to the formation of reduced Ti^{3+} at the STO interface, which is the key prerequisite for the formation of a redox 2DEG [133].

In addition to the oxygen diffusion, the cation interdiffusion during the growth may affect the interfacial redox reaction. However, in our case, the cation interdiffusion does not play a major role, because the interdiffusion of, e.g. Ti into the Fe_3O_4 matrix is expected to be negligibly small at the times and temperatures we used. For example, the diffusion coefficient of Ti in Fe_3O_4 at T=1000 °C was found to be $\approx 10^{-25}$ cm^2/ sec [134], resulting in diffusion lengths of (few pm) during the typical experiment times (12 h). With the temperatures used in this study, the diffusion length is even lower.

5.6 Towards stable $Fe_3O_4/SrTiO_3$ interfaces via annealing

In this section, we investigate how to grow Fe_3O_4 ultrathin films free from γ-Fe_2O_3 on STO substrates. In the literature, α-Fe_2O_3 is reduced to Fe_3O_4 by annealing in low oxygen pressure $< 10^{-7}$mbar and high temperature >800 °C, which has been shown for Fe_3O_4 films grown on Al_2O_3 [135]. However, in our case with the active STO substrate, these annealing conditions maybe not suitable. Thus, we study the annealing effect on the physical properties of the $Fe_3O_4/SrTiO_3$ heterostructures. We chose films with a thickness of $d = 4$ nm, as we expect that they are composed of 50 % γ-Fe_2O_3 and 50 % Fe_3O_4. Two films were prepared in the same environment. Subsequently, the first film was annealed at $T = 400$ °C for 90 min in $p_{O_2} = 2 \times 10^{-6}$mbar, whereas the second sample was annealed at $T = 700$ °C in $p_{O_2} = 2 \times 10^{-6}$mbar.

5.6.1 Surface morphology

The surface morphology of the films is studied by AFM. 3D-AFM images of the 400 °C-annealed, and the 700 °C-annealed films in comparison with the Nb:$SrTiO_3$ substrate, are shown in Figure 5.12. For 400 °C-annealed film, the surface properties (terrace structure) of the underlying STO are still visible (Figure 4.2 (b)). The 400 °C-annealed film shows a low surface roughness of 0.6±0.1 nm. In contrast, for the 700 °C-annealed film, the terrace structure of the underlying STO substrate disappears. Furthermore, the surface roughness increases to 1.7±0.2 nm. This indicates the island formation of Fe_3O_4 films.

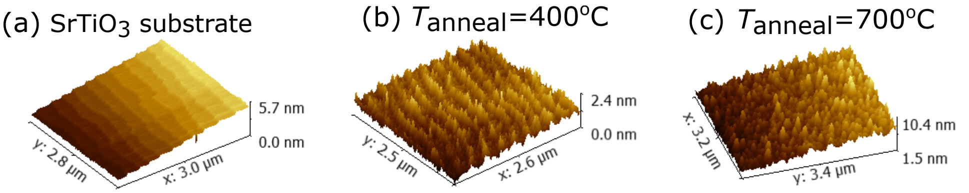

Figure 5.12: The AFM 3D images of (a) TiO_2-terminated Nb:$SrTiO_3$ substrate. 4 nm thick Fe_3O_4 films annealed in oxygen pressure of $p_{O_2} = 2 \times 10^{-6}$mbar at (b) 400 °C and (c) 700 °C, respectively.

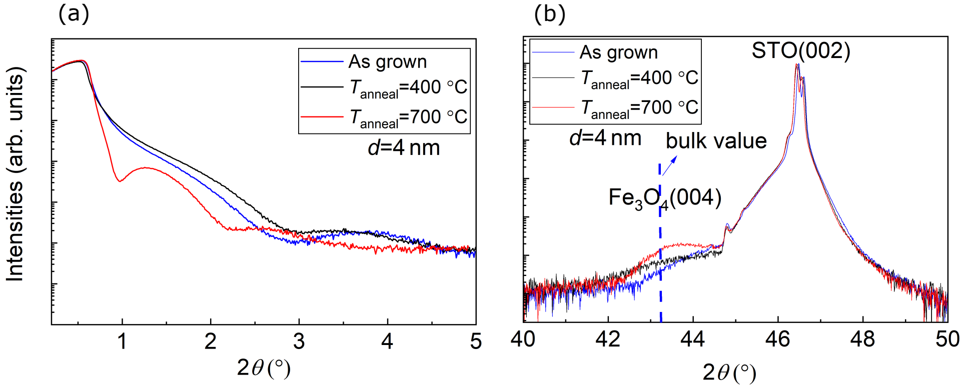

Figure 5.13: (a) X-ray reflectivity and (b) $\theta - 2\theta$ scans of the Fe_3O_4 (004) reflections for the as-grown and annealed in oxygen pressure of $p_{O_2} = 2 \times 10^{-6}$mbar at 400 °C and 700 °C Fe_3O_4 films.

5.6.2 Structural properties

XRR and XRD are used to investigate the structural changes due to the annealing procedure. Figure 5.13 (a) shows the X-ray reflectivity of the as-grown, 400 °C-annealed and 700 °C-annealed films. The as-grown and 400 °C-annealed films show a similar trend. However, the XRR intensity of the 700 °C-annealed film, drops faster, indicating the higher roughness of the film. Thus, the AFM and XRR measurements show a similar dependency. Figure 5.13 (b) illustrates the out-of-plane $\theta - 2\theta$ scans of the Fe_3O_4 (004) and $SrTiO_3$ (002) reflections of the three films. All XRD scans show peaks corresponding to the Fe_3O_4 (004) reflections, however:

(1) For the as-grown film, a weak peak related to Fe_3O_4 (004) reflections is observed.

(2) For the 400 °C-annealed film, the intensity of the Fe_3O_4 (004) peak is slightly enhanced.

(1) and (2) can be explained by the formation of two different phases: Fe_3O_4 and

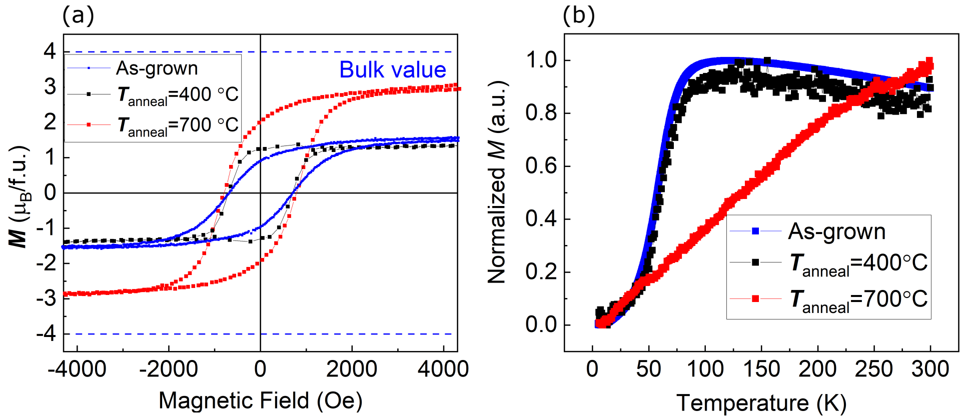

Figure 5.14: 4 nm Fe_3O_4 films grown on $SrTiO_3$ (001): as-grown, 400 °C-annealed and 700 °C-annealed films (a) Hysteresis loops and (b) Magnetization vs. temperature $M(T)$ to detect Verwey transition.

the intralayer γ-Fe_2O_3. They have a cubic inverse spinel structure, however, their lattice constant differs slightly. Accordingly, the (004) reflections differ slightly in peak position. Therefore, the XRD peaks show intensity-reduced and broadened peaks.

(3) For the 700 °C-annealed film, the Fe_3O_4 (004) peak shows a clear enhancement in the intensity which may be attributed to either an improved crystallinity of the film or the formation of only one phase.

5.6.3 Saturation magnetization

To investigate the saturation magnetization of the films (Figure 5.14 (a)), hysteresis loops have been measured by VSM. The saturation magnetization M_S for the 400 °C-annealed film is $1.4\pm0.2\,\mu_B$/f.u., which equals within the error an as-grown film without annealing ($M_S = 1.5\pm0.2\,\mu_B$/f.u.). This suggests that a γ-Fe_2O_3 phase is still at the interface of the 400 °C-annealed film. However, for the 700 °C-annealed film, M_S enhances to $3.1\pm0.3\,\mu_B$/f.u.. This value of the annealed 4 nm is close to the value measured for as-grown 38 nm films, which is dominated by the Fe_3O_4 phase. We, therefore, may have succeeded in obtaining the Fe_3O_4 phase by post-annealing at $T = 700$ °C.

5.6.4 Verwey transition

Next, we analyze the Verwey transition of the annealed films by measuring the $M(T)$ curve. Figure 5.14 (b) depicts the $M(T)$ curve and thus the Verwey transition of the

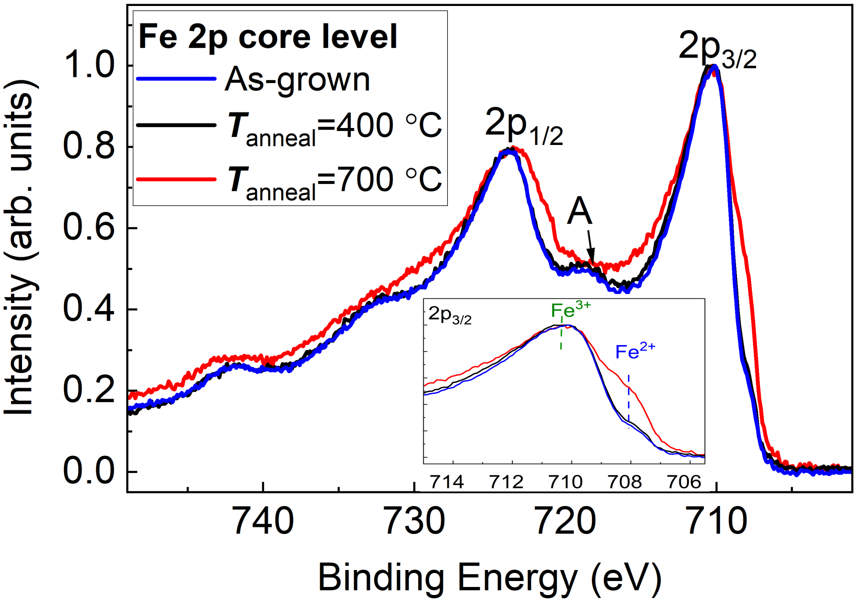

Figure 5.15: Fe 2p core level HAXPES spectra of 4 nm Fe_3O_4 films:as-grown, 400 °C-annealed and 400 °C-annealed. Inset shows Fe $2p_{3/2}$ core level.

films. The 400 °C-annealed film has a Verwey transition around 58 K identical to the as-grown film. However, the $M(T)$ curve of the 700 °C-annealed film shows a straight line without any transitions around the Verwey transition. Thus, it is not possible to detect the Verwey transition. This can either indicate the non-stoichiometric Fe_3O_4 phase or it is related to the enormous increase of the surface roughness. The surface roughness causes the discontinuity of the unit cells, which prevents the electron hopping. This leads to the disappearance of the Verwey transition.

5.6.5 HAXPES

To check the chemical stoichiometry of the annealed films, HAXPES experiments were conducted as shown in Figure 5.15. The appearance of satellite peak A for the sample annealed at 400 °C refers to the formation of a Fe_2O_3 phase, in agreement with the magnetization measurements. Moreover, the satellite peak A of the sample annealed at 700 °C disappears, whereas the shoulder of the Fe $2p_{3/2}$ enhances. This indicates the presence of Fe_3O_4 and disappearance of γ-Fe_2O_3 phase. We hereby demonstrated the tuning between two ferrimagnetic phases of iron oxide by taking control of the redox chemical processes at the $Fe_3O_4/SrTiO_3$ interface.

5.7 Conclusion

In summary, we grew Fe_3O_4 (100) on TiO_2-terminated Nb:$SrTiO_3$ (100) substrate with thicknesses in the range of $d = 2$-38 nm by PLD. We investigated the structural and magnetic properties of the $Fe_3O_4/SrTiO_3$ heterostructures using various techniques. Surprisingly, we observed by XRD a reduction of the out-of-plane Fe_3O_4 lattice constant with decreasing film thickness, despite the expected compressive strain induced by the $SrTiO_3$ substrate. The Verwey transition, which is an indicator for the Fe_3O_4 stoichiometry, decreases to 25 K for the film of thickness $d = 2$ nm. Despite the strong decrease in T_V for the 2 nm thick film, it is still detectable which has not been reported before. The HAXPES and XMCD measurements reveal the formation of an interfacial ferrimagnetic γ-Fe_2O_3 layer of 2 u.c. in the $Fe_3O_4/SrTiO_3$ heterostructures, independent of the total film thickness. This contradicts the literature [79, 81], which reported FeO at the interface between Fe_3O_4 and $SrTiO_3$. However, the γ-Fe_2O_3 intralayer formation is favored in our study because of the oxygen vacancies on the TiO_2-terminated $SrTiO_3$ surface, which change the surface Gibbs free energy of the $SrTiO_3$. We succeed in reducing the oxidized interfacial phase γ-Fe_2O_3 by post-annealing at high temperatures of 700 °C and oxygen pressure of 2×10^{-6}mbar. Our results open the exciting perspective of enabling the continuous tuning of the spin-dependent properties of Fe_3O_4-based heterostructures, depending on Fe_3O_4 film thickness and redox process parameters.

So far, we claim that the redox process at the interfaces is highly dependent on the oxygen supply of the underlying $SrTiO_3$ substrate. In the next step, we will compare the growth of the Fe_3O_4 phase on another oxide substrate which is believed to be mostly inert; yttrium stabilized zirconia (YSZ), in Chapter 6.

CHAPTER 6

Growth of Fe_3O_4 on "inert" YSZ oxide substrates

Along with the particular growth conditions, the properties of iron oxides ultrathin films are strongly determined by the choice of its substrate counterpart [136, 137]. Often, the (mostly unintentional) formation of reduced [79, 138] or oxidized (Chapter 5) phases at the interfaces have been observed. In Chapter 4 and 5, we showed the effect of the $SrTiO_3$ substrates on the properties of Fe_3O_4 films. In particular, we observed the formation of 2 u.c. interfacial ferrimagnetic insulator γ-Fe_2O_3 layers, which are formed by the diffusion of oxygen ions from the $SrTiO_3$ substrate towards Fe_3O_4. Therefore, the redox process at the interfaces is highly dependent on the oxygen supply of the underlying oxide substrates. Thus, we choose another oxide substrate, the YSZ(100) that has less oxygen diffusivity than the $SrTiO_3$ substrates.

In this Chapter, special attention is paid on the impact of the growth temperature and thickness on the chemical and magnetic properties of the Fe_3O_4 films and interfaces grown on YSZ (100) substrates. Two important results are found: (1) the Fe_3O_4 films grown parallel to the (111) plane, and (2) the formation of a Fe_2O_3 phase at the interface is observed for ultrathin films. The formation of the oxidized phase at the interface between Fe_3O_4 and YSZ is not expected, because YSZ is much less prone to reduction than Nb:$SrTiO_3$. On the other hand, YSZ is a very good oxygen conductor. Therefore, oxygen could easily diffuse from the outer atmosphere through the YSZ substrate and thereby may cause the formation of an Fe_2O_3 intralayer as it will be shown in this chapter.

6.1 PLD growth conditions

A series of Fe_3O_4 thin films were grown by PLD on yttria-stabilized zirconia (001) (YSZ) with 9.5 % Y_2O_3 doping level. We used the same growth parameters as for the Fe_3O_4/$SrTiO_3$ (100) heterostructures. In particular, the oxygen partial pressure was kept at 2×10^{-6}mbar. Furthermore, the laser fluence was set to 1.5 J/cm^2 with a repetition rate of 5 Hz producing ionized particles from a Fe_2O_3 rotating target. Here, we vary two growth parameters: the growth temperature ($T_{growth} = 300\,°C$-$500\,°C$) and the film thickness ($d = 4$-38 nm).

6.2 Growth temperature: structural and magnetic characterization

The growth temperature is an important growth parameter that influences the structure and magnetic properties of the films grown on $SrTiO_3$ as we discussed in Chapter 4. Thus, a series of Fe_3O_4/YSZ heterostructures was grown at growth temperatures of $T_{growth} = 300\,°C$-$500\,°C$, while, the thickness of the films was kept at 38 nm. To assure the quality of the films, we investigate the structure and magnetic properties of the films. The structure crystallinity of the films is investigated by XRD. Additionally, we examine two magnetic parameters by VSM that indicate the quality of the magnetite films: (1) the saturation magnetization and (2) the Verwey transition.

6.2.1 Experimental details

The crystalline structure, film thickness and surface roughness of the grown films were examined using X-ray diffraction (XRD) and X-ray reflectivity (XRR). Both, XRR and XRD experiments were performed at room temperature on a Philips XPert MRD using Cu-K_α-radiation. Magnetic properties of the heterostructures were investigated by a vibrating sample magnetometer (VSM) using a Quantum Design Dynacool physical properties measurement system (PPMS). Magnetic moment versus temperature $M(T)$ was measured in zero-field cooling (ZFC) mode with 500 Oe applied field. Hysteresis loops were recorded at a magnetic field of $H = \pm 5$ T along the in-plane [100]-axis.

6.2.2 Structural properties

The crystallinity and structural properties of the Fe_3O_4 films grown on YSZ (001) were investigated by XRD. To confirm the epitaxial growth of the films, out-of-plane θ-2θ scans within a 2θ range from 15° to 110° were measured. All XRD scans are normalized to their YSZ (002) reflection. All scans show two peaks corresponding to the YSZ (002) and (004) reflections. Furthermore, four additional peaks appear, corresponding to the

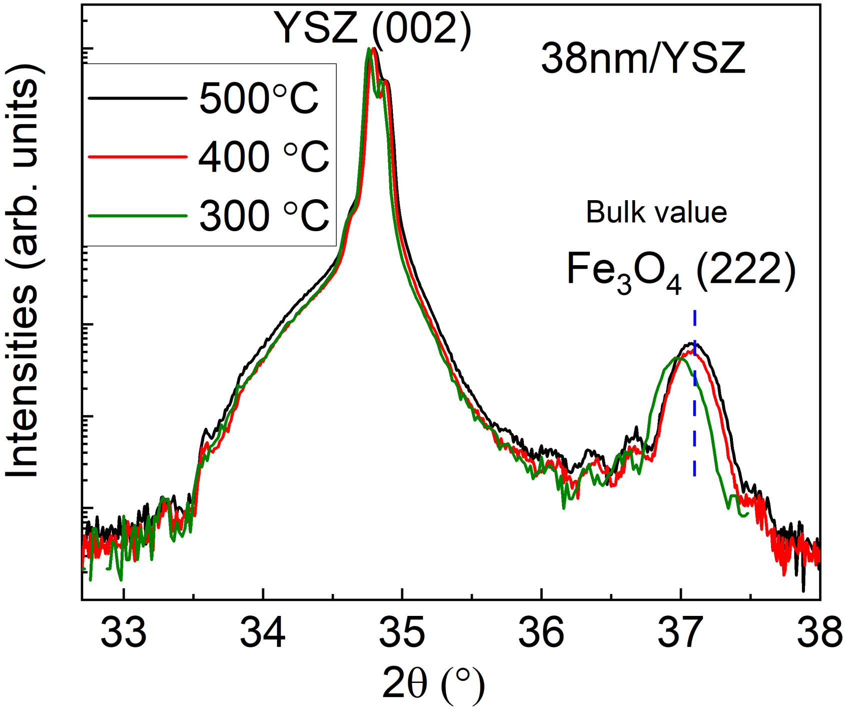

Figure 6.1: The out-of-plane $\theta - 2\theta$ scans of the Fe$_3$O$_4$ (222) and the YSZ (002) reflections for 38 nm thick films grown at different growth temperatures of $T_{growth} = 500$ °C, 400 °C and 300 °C.

Fe$_3$O$_4$ (111), (222), (333) and (444) reflections. The lattice constant of Fe$_3$O$_4$ is 8.395 Å and of YSZ equals 5.16 Å. Thus, the mismatch between the film and the substrate is larger than 30 %. On the other hand, the interplanar spacing $d_{(111)}$ of Fe$_3$O$_4$ is 4.846 Å. Therefore, the mismatch between the YSZ (100) and Fe$_3$O$_4$ (111) is 6 %. Accordingly, the Fe$_3$O$_4$ unit cell prefers to grow parallel to the (111) planes on the YSZ (100).

The out-of-plane θ-2θ scans around the Fe$_3$O$_4$ (222) and YSZ (002) reflections are shown in Figure 6.1. The Fe$_3$O$_4$ (222) peak positions of the films grown at temperatures of 500 °C and 400 °C are very close to the bulk position of Fe$_3$O$_4$ (blue dashed line). However, the peak of the film grown at a temperature of 300 °C is shifted towards slightly smaller angles. This implies that the out-of-plane lattice constant c_{oop} of the films is close to the Fe$_3$O$_4$ bulk value. Thus, all the films are fully relaxed on the YSZ substrates.

Three main differences have been noticed between the Fe$_3$O$_4$/YSZ and Fe$_3$O$_4$/SrTiO$_3$ XRD scans:

(1) The Fe$_3$O$_4$ films are epitaxially grown along the (111) planes on YSZ (100), but

along the (100) planes on STO (100).

(2) The Fe_3O_4 films grown on YSZ are completely relaxed, however, the Fe_3O_4 films grown on STO are strained.

(3) The Laue oscillations of the (222) Fe_3O_4 reflections appear for all the films grown on YSZ. However, for all the films grown on $SrTiO_3$, the Laue oscillations vanish. These Laue oscillations reflect the structural homogeneity of the films, low density of defects and the high crystalline order.

6.2.3 Saturation magnetization

In order to determine the saturation magnetization of the Fe_3O_4 films grown at different temperatures, hysteresis loops were measured and recorded at temperatures between 5 K and room temperature. The diamagnetic contribution from the YSZ substrate has been corrected with the identical procedure discussed for STO substrates in Section 3.2.3. In Figure 6.2 (a-c), the hysteresis loops for the Fe_3O_4 films grown at different temperatures are depicted. The hysteresis loops of all Fe_3O_4 films show identical behavior. The saturation magnetization of all Fe_3O_4 films is identical within the respective errors (3.3-3.4 μ_B/f.u.), which is equal to the one of the $Fe_3O_4/SrTiO_3$ heterostructures with the same thickness of 38 nm. However, the saturation magnetization is less than the ideal theoretical bulk Fe_3O_4 value of 4 μ_B/f.u. [98], because of the formation of antiferromagnetic anti-phase boundaries and structural dislocations.

6.2.4 Verwey transition

Figure 6.2 (d-f) depicts the $M(T)$ curve of the films grown at different temperatures measured in zero-field cooling mode with an applied field of 500 Oe. The magnetization as a function of temperature $M(T)$ of the films (solid square) drops around 120 K referring to the Verwey transition. To exactly determine the Verwey transition T_V, the maximum $\partial M/\partial T$ (open square) is calculated. To determine the transition width ΔT_V (the sharpness of the transition), the maximum of $\partial^2 M/\partial T^2$ (open triangle) is calculated. All Fe_3O_4 films show almost identical magnetic behavior. However, the magnetic properties of the Fe_3O_4 film grown at $T_{growth} = 400\,°C$ is the closest to the ideal bulk properties. The magnetization of this Fe_3O_4 film drops by 17 % below $T_V = 117 \pm 0.6$ K and the transition width ΔT_V equals 14 ± 0.7 K. The values of T_V and ΔT_V of the Fe_3O_4 films grown at different temperatures are depicted in Table 6.1.

6.2.5 Summary

In summary, the structural and magnetic properties of Fe_3O_4 films grown on YSZ with a thickness of 38 nm are growth temperature independent. All the films are grown parallel to the (111) plan on the YSZ (100) and show Laue oscillations indicating the high

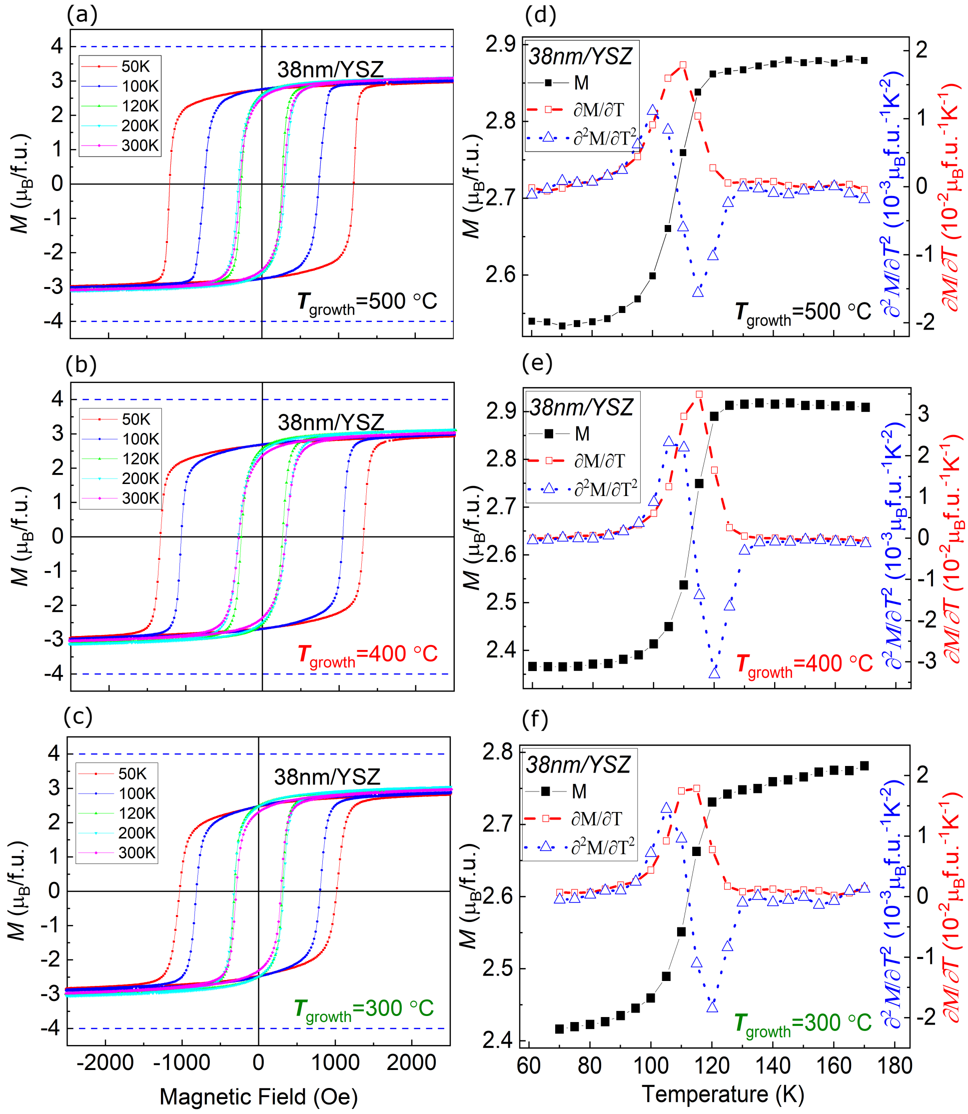

Figure 6.2: Hysteresis loops for 38 nm thick Fe_3O_4 films grown at different growth temperatures of (a) 500 °C, (b) 400 °C, and (c) 300 °C. Magnetization vs. temperature (solid square), the first and second derivatives for the magnetization curve (open square and open triangle respectively) of Fe_3O_4 films grown at temperatures (d) 500 °C, (e) 400 °C, and (f) 300 °C.

Table 6.1: Magnetization parameters of Fe_3O_4/YSZ heterostructures grown at different growth temperatures determined from the MT curves.

T_{growth} (°C)	T_V (K)	ΔT_V (K)	**Magnetization drop** (%)
300	115±0.8	15±0.9	12
400	117±0.6	14±0.7	17
500	113±0.8	16±0.8	13

crystalline quality of the films. Additionally, the saturation magnetization of the films is identical. However, the Fe_3O_4 film grown at $T_{growth} = 400\,°C$ has the closest T_V to the ideal bulk value of 120 K. Thus, the chosen growth temperature for the thickness study is $T_{growth} = 400\,°C$.

6.3 Thickness dependent: HAXPES

In the next step, we emphasize the influence of reduced film thickness down to 4 nm on the chemical properties of Fe_3O_4/YSZ heterostructures. The bulk element-sensitive HAXPES has been used to precisely understand the stoichiometry of the films. Therefore, we grew films of thicknesses between 4 and 38 nm at a growth temperature of 400 °C.

6.3.1 Experimental details

Element-selective and depth-dependent chemical information of the films and buried interfaces were analyzed by hard X-ray photoelectron spectroscopy (HAXPES) at the KMC-1 beamline at BESSY II (Berlin, Germany) using the HIKE endstation. The photon energy used in this study is $h\nu = 4\,\mathrm{keV}$ which results in an information depth of $\lambda = 20$-$25\,\mathrm{nm}$ for Fe_3O_4. The samples are adjusted to normal emission geometry.

6.3.2 HAXPES

Figure 6.3 (a) shows Fe 2p core level spectra of the 4, 12 and 38 nm thick films. For the 38 nm thick Fe_3O_4 film, we find that the two satellites of the Fe^{2+} and Fe^{3+} cations are merged. Moreover, the Fe $2p_{3/2}$ core level, which is depicted in Figure 6.3 (b), is composed of the Fe^{3+} peak and a shoulder that refers to Fe^{2+}. Consequently, we observe a Fe_3O_4 bulk-like stoichiometry of the 38 nm thick Fe_3O_4 film.

In order to investigate the buried Fe_3O_4/YSZ interfaces, HAXPES was conducted for the $d = 4$ nm and 12 nm films, shown in Figure 6.3 (a). We observe that the Fe^{3+} satellite peak appears for the 4 nm film. Moreover, the Fe $2p_{3/2}$ peak's shoulder intensity decreases with

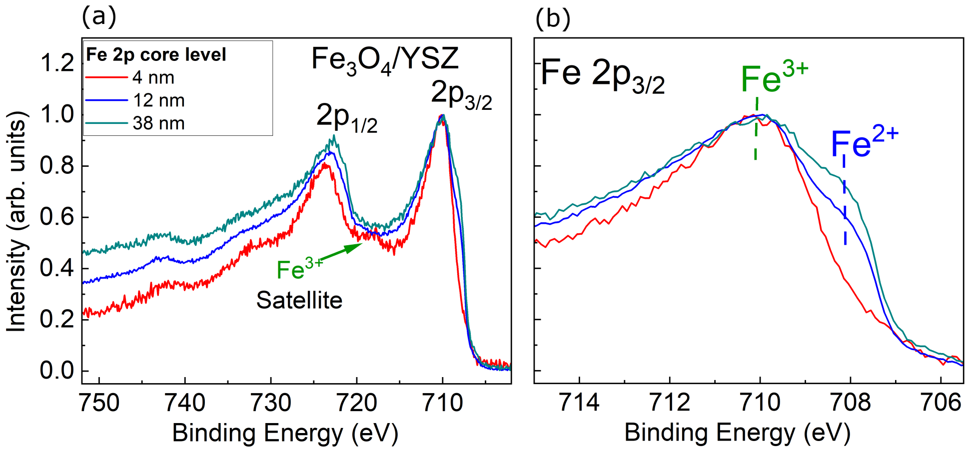

Figure 6.3: (a) Fe 2p core level spectra of Fe_3O_4 (111)/YSZ(001) for varying film thickness recorded using $h\nu = 4\,\text{keV}$. (b) Fe $2p_{3/2}$ core level.

decreasing film thickness, which is indicative of the decreasing of the Fe^{2+} contribution. Both observations suggest the formation of the Fe_2O_3 phase in addition to the Fe_3O_4 phase for ultrathin films grown on YSZ substrates.

6.3.3 Discussion

The observation of the Fe_2O_3 phase may indicate an oxygen supply from the underlying YSZ substrate which refers to possible redox reactions at the interface. For the films grown on Nb:$SrTiO_3$, we previously (Chapter 5) explained the formation of the oxidized γ-Fe_2O_3 phase at the interface by the reduction of the TiO_2-terminated $SrTiO_3$ substrate, which in turn provides the oxygen causing the formation of the γ-Fe_2O_3 intralayer. For films grown on YSZ, the reducibility of the YSZ substrate is much lower compared to $SrTiO_3$ and depends on the doping percentage [139, 140]. Again, thermodynamics play an important role as we discuss in the next section.

6.4 Substrate-assisted interface oxidation

First, as discussed in Chapter 2 Section 2.3, from the thermodynamics point of view, the Gibbs free energy ΔG_F^o of YSZ with Y_2O_3 doping level of 10 % equals $-1200\,\text{kJ/mol}$. It is lower than the ΔG_F^o of Fe_3O_4 with $-1164\,\text{kJ/mol}$. Therefore, YSZ is not expected to oxidize Fe_3O_4. On the other hand, the ΔG_F^o of ZrO_2 equals $-1112.1\,\text{kJ/mol}$, which is higher than the ΔG_F^o of Fe_3O_4. This indicates the possible reduction of YSZ surfaces by the Fe_3O_4 films. Thus, the doping level of ZrO_2 with Y_2O_3 may perturb the formation energy of YSZ. Additionally, the YSZ is known to be a good electrolyte because of its

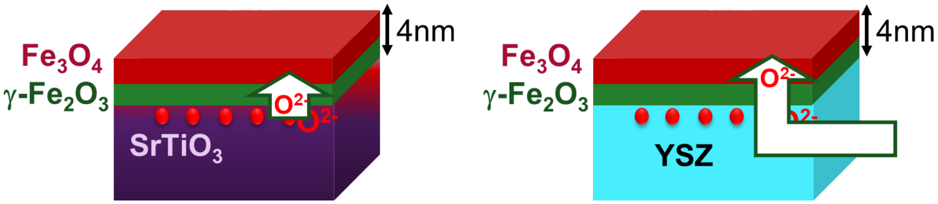

Figure 6.4: The formation process of Fe_2O_3 at the interfaces between the oxides substrates ($SrTiO_3$ and YSZ) and Fe_3O_4 films has different mechanisms: (1) redox process at the interfaces $Fe_3O_4/SrTiO_3$ and (2) oxygen diffusion through the substrate from the outer atmosphere Fe_3O_4/YSZ.

high oxygen conductivity [141] which may be influenced by the doping level as well. Therefore, oxygen can diffuse from the outer atmosphere through the YSZ substrate and causes the formation of Fe_2O_3 intralayer (Figure 6.4). Therefore, either surface reduction through thermodynamics perturbation or oxygen diffusion through YSZ from the outer atmosphere may explain the oxidation of Fe_3O_4 to Fe_2O_3.

6.5 Conclusion

In summary, we grew Fe_3O_4 on YSZ at different growth temperature $T_{growth} = 300\text{-}500\,°C$ and with different thicknesses $d = 4\text{-}38\,nm$. We investigated the quality of the film (structural and magnetic properties) by XRD and VSM. The Fe_3O_4 thin films have been grown epitaxially parallel to the (111) plan on the YSZ (100). All the Fe_3O_4 films grown at different growth temperatures show Laue oscillations, which indicates the high crystalline order of the films. By detecting the Verwey transition of all the Fe_3O_4 films grown at different growth temperatures, we found that the film grown at $T_{growth} = 400\,°C$ has a Verwey transition of $T_V = 117 \pm 0.6\,K$, which is the closest to the bulk Fe_3O_4 value. The chemical structure of the films grown with different thicknesses was investigated by HAXPES. The formation of Fe_2O_3 was detected for the ultrathin film of $d = 4\,nm$. The formation of an oxidized intralayer can be explained by either (1) an interfacial redox reaction that arises at some particular level of doping of Y_2O_3 or (2) diffusion of oxygen through the substrate from the outside atmosphere.

We assume that the origin of the formation of an interfacial oxidized phase of Fe_2O_3 on $SrTiO_3$ and YSZ is different. Thus, in the next step, we compare the thermally-induced phase transitions of the Fe_3O_4 films grown on both $SrTiO_3$ and YSZ (Chapter 7).

CHAPTER 7

Thermally induced magnetic phase transition of iron oxides

The presented results in this chapter are taken from the published paper *"Thermal phase design of ultrathin magnetic iron oxide films: from Fe_3O_4 to γ-Fe_2O_3 and FeO"*: Mai Hussein Hamed, David N. Mueller and Martina Müller, Journal of Materials Chemistry C, 2020, **8**, 1335-1343 [142].

7.1 Introduction

We discussed in Chapter 5 and 6 that the redox process is highly dependent on the oxygen supply of the underlying oxide substrates and the outside atmosphere. The oxygen supply of a substrate reflects directly the oxygen mobility, which can be increased by a small annealing step. Consequently, many aspects are still ambiguous and require further investigation: (1) the effect of the annealing in UHV atmosphere on the efficiency of the oxygen diffusion from the substrates to the film, (2) the influence of the different oxide substrates on the redox reactions at the interfaces and (3) the effect of the surface terminations on the redox reactions.

The phase transformations between Fe_3O_4, γ-Fe_2O_3 and FeO by thermal annealing have mostly been studied on Fe_xO_y thin films grown on metal substrates, particularly Pt [143, 144] and Ag [145]. Here, the main control parameters are temperature and ambient oxygen pressure. For all-oxide heterostructures, i.e. Fe_xO_y on oxide substrates, however, the redox reactions at the interfaces are also driven by thermally activated oxygen diffusion. The interfacial thermodynamic properties of Fe_xO_y films grown on "active" oxide substrates are inherently different from the known bulk behavior and not well understood in the literature. Thus, a systematic annealing study of the physical and chemical

Figure 7.1: Schematics indicating the heterostructures $Fe_xO_y/SrTiO_3$ with the possible oxygen diffusion through the three relevant interfaces: (A) the outside atmosphere/Fe_xO_y film interface, (B) the interface between phase-transformed Fe_xO_y/Fe_xO_y intralayers and (C) the Fe_xO_y/substrate interface.

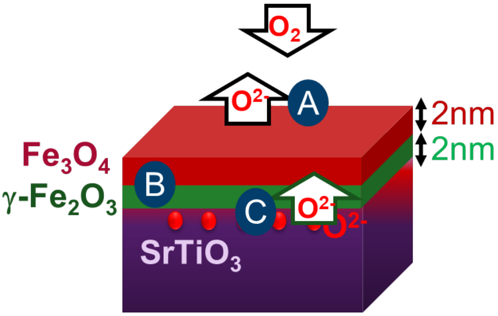

properties of Fe_xO_y/oxide heterostructures compared to bulk-like Fe_xO_y phases is still missing.

In this chapter, we demonstrate the thermally induced phase transformations between Fe_3O_4, γ-Fe_2O_3 and FeO ultrathin iron oxide films. Special attention is paid to the understanding of the thermodynamics of the interactions through the interfaces and the influence of oxide substrates in particular $SrTiO_3$ and YSZ on the interfacial redox process. The redox process within the oxide heterostructures occurs at three relevant interfaces, i.e. (A) the outside atmosphere/Fe_xO_y film interface, (B) the interface between phase-transformed Fe_xO_y/Fe_xO_y intralayer and (C) the Fe_xO_y/substrate interface shown in Figure 7.1. After a comprehensive thermodynamic analysis of the interfacial redox process, we find that the thermal phase transformations of the iron oxides films significantly differ from what is predicted via the standard iron oxides phase diagram. We thereby reveal the essential – but mostly underrated – role of oxide substrates as additional oxygen suppliers or scavengers, which can completely alter the standard Fe_xO_y temperature-pressure phase diagram. We introduce an adjusted phase diagram specifically for Fe_xO_y/ Nb:$SrTiO_3$ and Fe_xO_y / YSZ heterostructures based on total effective oxygen activity.

7.2 Experimental setup

Iron oxide (Fe_xO_y) films were deposited by pulsed laser deposition (PLD) on two different substrates, 0.1 % Nb-doped TiO_2-terminated $SrTiO_3$ (001) (NSTO) and yttria-stabilized zirconia (001) (YSZ) with a 9.5 % Y_2O_3 doping level. The film thicknesses are 2, 4 and 38 nm. The deposition was performed using a Fe_2O_3 rotating target and substrates held at a temperature $T = 400\,°C$. During growth, the oxygen background pressure was kept at 2×10^{-6} mbar. The laser fluence and repetition rate were set to $1.5\,J/cm^2$ and 5 Hz, respectively.

The depth-dependent chemical properties of the heterostructures were investigated by hard X-ray photoelectron spectroscopy (HAXPES) at the KMC-1 beamline at BESSY II (Berlin, Germany) using the HIKE endstation. HAXPES measurements have been done using a photon energy of 4 keV and in normal emission geometry. We monitored the thermally induced chemical changes using HAXPES as follows: In the HAXPES UHV chamber the temperature of the samples was enhanced step-wise from 25 °C to 700 °C. At each step, the temperature first had to stabilize for 20 min. Then the Fe 2p core level spectra were recorded at the stabilized temperature.

7.3 HAXPES fitting routine

In order to extract the Fe^0, Fe^{2+} and Fe^{3+} cation ratios, a quantitative HAXPES analysis has to be performed. Several physical aspects have to be considered in order to obtain a consistent fit for the Fe 2p core level, most important:

- Subtraction of the background is the first challenge. The background originates from inelastic photoelectron scattering. This inelastic scattering depends on the film thickness. Thus, the background fitting has to be done for each film separately. The background fitting has to be performed very carefully so as not to lose important information about our system (here: on stochiometry).
- For each oxide phase, its own set of the Fe^0, Fe^{2+} and Fe^{3+} cation reference Fe 2p core level has to be modeled. Many complex models have been used to calculate these sets of Fe 2p cation reference spectra for the different oxide phases [146, 147].

Covering all these aspects is very time consuming and thus not applicable to the data in this chapter. Therefore, we fit each spectrum of one sample by the linear combination of two chosen spectra:

(1) The first spectrum represents the γ-Fe_2O_3 and Fe_3O_4 phases. This spectrum measured at room temperature for the specific film thickness. The Fe^{2+} and Fe^{3+} cations ratios are taken from Chapter 5

(2) The second spectra represents the FeO phase. This spectrum is measured at annealing temperature for the specific film thickness where the Fe^{2+} cations ratio is 100 %.

Examples for the fitted HAXPES spectra of films with thicknesses of 2 nm and 38 nm are shown in Figure 7.2. The calculated spectrum (dotted line) is the fit of the experimental Fe 2p core level (solid line). The difference between the fitted and experimental spectrum is shown by the yellow line. The yellow line indicates that most of the calculated spectra fit well to the experimental spectra, which indicate the proper calculated ratios for the Fe, Fe^{2+} and Fe^{3+} cations. However, this does not hold for some spectra: For example, Figure 7.2 (a) shows the HAXPES measurements of 2 nm film annealed at a temperature of 300 °C. The shape of the calculated peaks around 710 eV does not match the experimental spectra. This is a result of the rather rough approach of linear combination. The different crystalline structure of Fe_3O_4, Fe_2O_3 and FeO is not taken into account as well as hybridization effects and complex d-d multiplet splitting caused by the partially filled 3d states. All these parameters contribute to the peak structure. Thus, we cannot

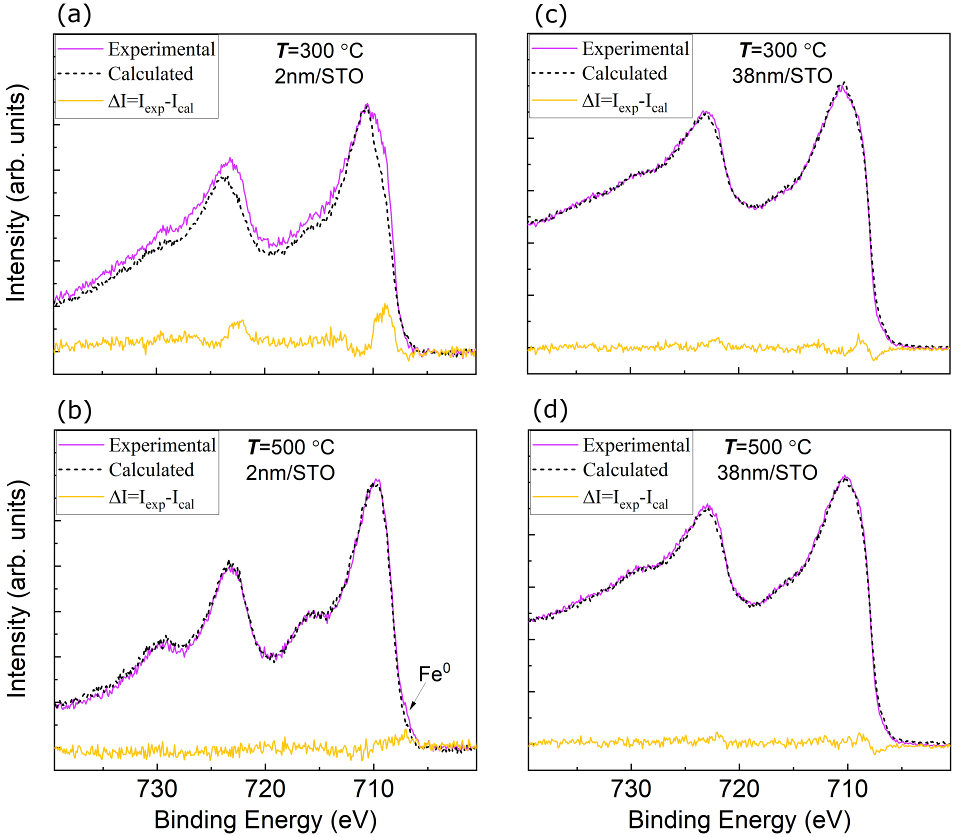

Figure 7.2: Fitting example for films annealed at (a) and (c) 300 °C and (b) and (d) 500 °C of thickness 2 nm and 38 nm, respectively.

always simply fit the spectra by linear combination. However, we fitted the spectra to have the same intensity and shape of the satellite peaks, which gives very close cation ratios compared to reality.

7.4 Annealing of ultrathin iron oxide films in UHV and in oxygen

7.4.1 HAXPES

First, we monitor the change of chemical properties of Fe_xO_y ultrathin films due to thermal annealing in different oxygen atmospheres via HAXPES. We examine two ultrathin films with a thickness of $d = 4\,\text{nm}$ each, which are composed of 42% Fe_3O_4 and 58% γ-Fe_2O_3 grown on NSTO(001). One film was annealed in the UHV chamber (base pressure 10^{-8} mbar, hence $p_{O_2} \ll 10^{-8}$ mbar) at two temperatures of $T_{anneal} = 400\,°\text{C}$ and $T_{anneal} = 700\,°\text{C}$. The second film was annealed in an oxygen gas atmosphere of $p_{O_2} = 10^{-6}$ mbar at the same two temperatures. The Fe 2p core levels of the films are shown in Figure 7.3.

From the standard phase diagram of bulk iron oxides (Figure 7.4), we would expect the following reduction-oxidation conditions:

(1) An oxygen pressure $p_{O_2} = 10^{-6}$ mbar and a temperature $T_{anneal} > 750\,°\text{C}$ is needed to reduce Fe_2O_3 to Fe_3O_4, whereas the reduction to the binary FeO phase is not possible at this pressure.

(2) Decreasing the oxygen pressure to $p_{O_2} < 10^{-8}$mbar reduces the temperature necessary for the reduction of Fe_2O_3 to Fe_3O_4 to $T_{anneal} = 650\,°\text{C}$. The reduction to FeO, which is a very narrow region in the phase diagram, could be achieved by annealing at very high temperatures of $T_{anneal} > 1000\,°\text{C}$. Above a temperature of about 1200 °C, the reduction to Fe metal already sets in.

(3) In order to stabilize the FeO phase at lower temperatures, e.g. $T_{anneal} = 700\,°\text{C}$, annealing in an extremely low pressure $p_{O_2} = 10^{-18}$ mbar – not accessible by conventional means – would have to be feasible. Also at this low pressure the temperature, window of FeO formation is extremely small (20 K).

Figure 7.3 (a) depicts the HAXPES spectra of the one film annealed at $T_{anneal} = 400\,°\text{C}$ in UHV-atmosphere and the other film annealed at $T_{anneal} = 400\,°\text{C}$ in oxygen atmosphere. The latter shows the appearance of a satellite peak at $E_B = 719\,\text{eV}$, which is characteristic for the Fe_2O_3 phase [61]. We determined an iron oxide ratio of 58 % γ-Fe_2O_3 and 42 % Fe_3O_4, which is similar to the as-grown film. In contrast, the HAXPES spectrum of the film annealed at $T_{anneal} = 400\,°\text{C}$ in UHV-atmosphere reveals a satellite peak at $E_B = 715.5\,\text{eV}$ indicating the formation of FeO [62]. Moreover, the Fe $2p_{3/2}$ core level, which is composed of the Fe^{3+} peak and a shoulder that refers to Fe^{2+}, shows a clear

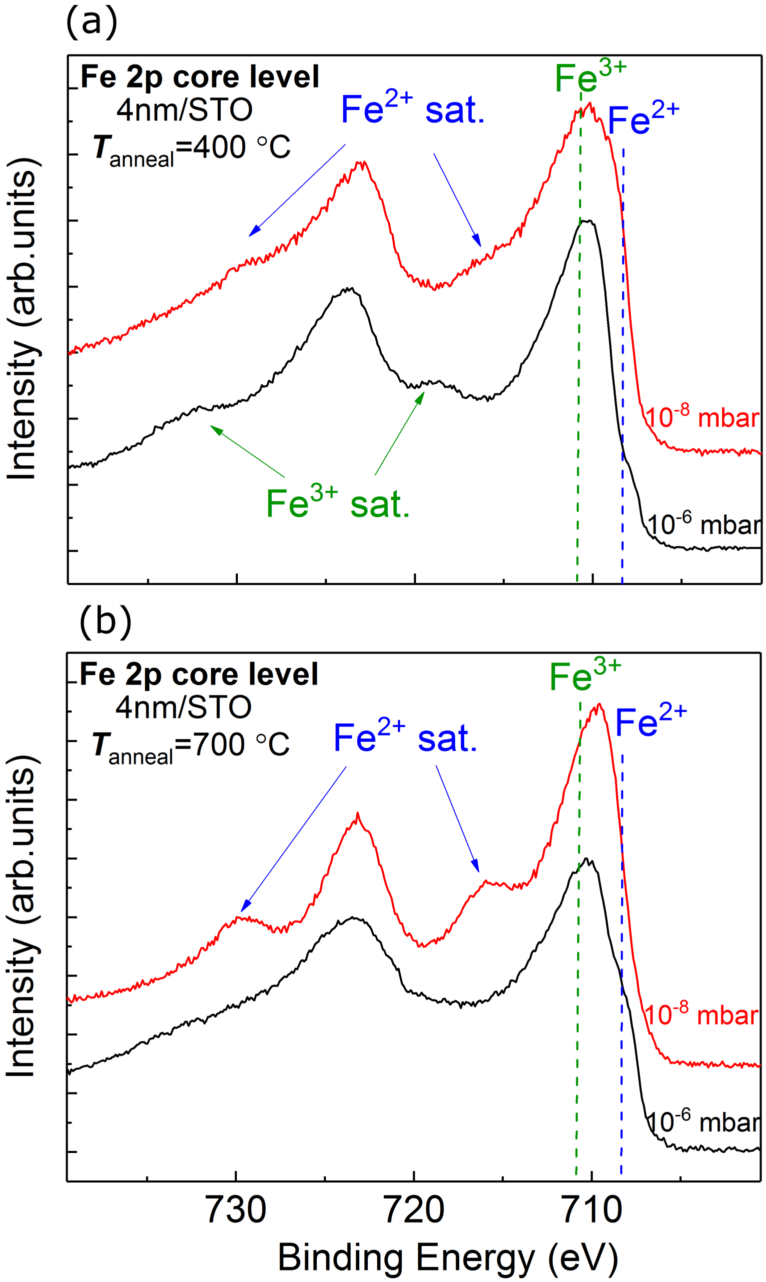

Figure 7.3: Fe 2p core level spectra recorded at annealing temperatures of $T_{anneal} = 400\,°C$ and $T_{anneal} = 700\,°C$, respectively, (a) in UHV-atmosphere and (b) in an O_2 background pressure of $p_{O_2} = 2 \times 10^{-6}$ mbar.

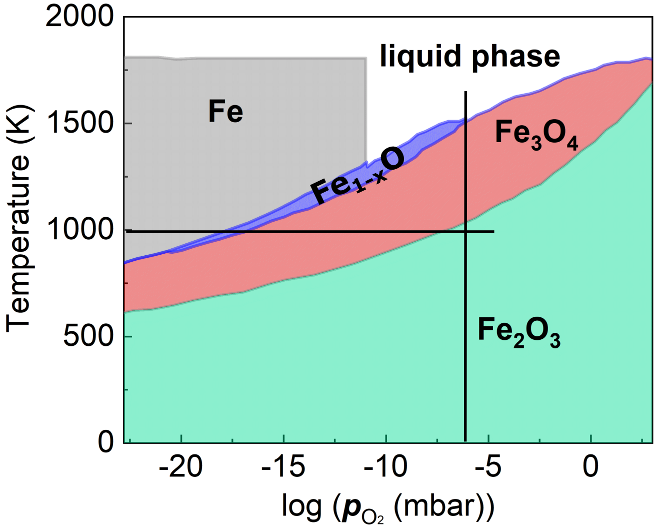

Figure 7.4: The standard temperature-pressure phase diagram of (freestanding) iron oxides [148] with guide lines indicating the pressure 10^{-6} mbar and the temperature 700 °C.

enhancement of the Fe^{2+} intensity. Quantitatively, we find a composition of 12 % FeO and 88 % Fe_3O_4.

In the second experiment, as shown in Figure 7.3 (b), we increase the annealing temperature to $T_{anneal} = 700\,°C$ both in UHV and oxygen atmosphere. The Fe 2p core level for the film annealed in oxygen atmosphere reveals the formation of approximately 100 % Fe_3O_4, as deduced from the merged satellite peaks and enhanced Fe^{2+} shoulder of the Fe $2p_{3/2}$ core level peak. For the film annealed in UHV, the high intensity of the satellite peak at $E_B = 715.5$ eV and peak shape of the Fe $2p_{3/2}$ core level indicate the formation of a 100 % FeO phase.

7.4.2 Discussion

Figure 7.5 shows schematics for the reduction process from γ-Fe_2O_3 and Fe_3O_4 to FeO by increasing the annealing temperature and decreasing the oxygen pressure. According to the standard phase diagram (Figure 7.4), an annealing temperature of 400 °C in $p_{O_2} = 2 \times 10^{-6}$mbar shall not be sufficient to reduce Fe_2O_3 to Fe_3O_4. Even annealing at very low oxygen pressure $<10^{-22}$mbar requires temperatures higher than 400 °C to reduce to Fe_3O_4, and it is not possible to further reduce to the FeO phase. Our findings strongly deviate from the theoretical thermodynamic predictions for bulk iron oxides. Once more, comparing the results for films annealed at 700 °C to the standard phase diagram fails

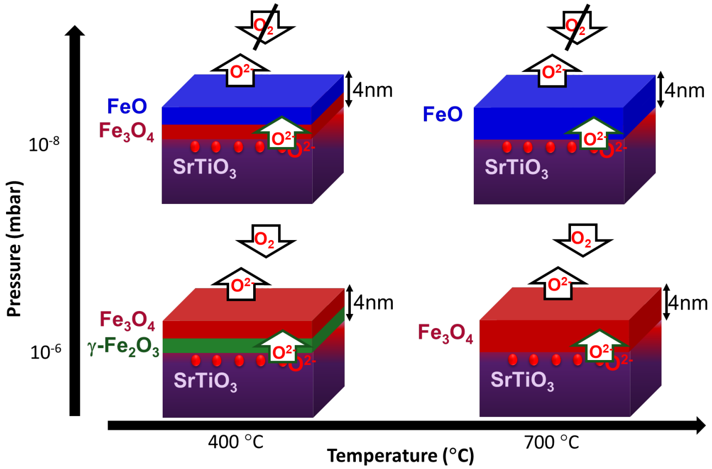

Figure 7.5: Schematics of iron oxide heterostructures of films with thickness $d = 4\,\mathrm{nm}$ of 50 % γ-Fe_2O_3 and 50 % Fe_3O_4 on Nb:$SrTiO_3$ substrates, annealed at two different temperatures $T_{anneal} = 400\,°\mathrm{C}$ and $T_{anneal} = 700\,°\mathrm{C}$ either in UHV-atmosphere or in an O_2 background pressure of $p_{O_2} = 2 \times 10^{-6}\,\mathrm{mbar}$.

for the film annealed in UHV as well as the film annealed in the oxygen atmosphere. In particular, the calculated temperature window of a (freestanding) FeO phase is limited to around 200 °C, which is not consistent with our experimental observations ranging from 400 °C to 700 °C in Fe_xO_y/NSTO heterostructures.

The temperature-dependent redox process is dependent on the oxygen supply of the chamber atmosphere, and, in case of a heterostructure, on the oxygen supply of the underlying substrate. By increasing the annealing temperature, the mobility of oxygen increases within the heterostructure and allows exchange with the atmosphere. Two scenarios have to be distinguished:

(1) During the annealing in an oxygen atmosphere, the thermally released oxygen in the film and the substrate are refilled.

(2) For annealing in UHV, in contrast, any released oxygen will not be refilled. If the substrate simply supplies oxygen to the film, the oxidation of the film will be expected. However, the processes involved are much more complex.

The fact that our findings strongly deviate from theoretical thermodynamic predictions is probably due to two major differences: (i) the downscaled dimensionality of ultrathin films compared to bulk Fe_xO_y and (ii) presence of an oxide substrate, which plays a twofold role:

(1) On the one hand, thermally activated oxygen diffuses from the substrate to the film, explaining the formation of γ-Fe_2O_3 at the interface. Furthermore, this oxygen

diffusion slows down the reduction process of the FeO phase. This may be the reason for the larger temperature window for a reduction of 300 °C compared to the standard phase diagram.

(2) On the other hand, the thermodynamic properties of the STO substrate may even enhance the reduction process to the FeO phase, which explains that $T_{anneal} = 400$ °C is sufficient to reduce to the FeO phase.

A quantitative description of the thermodynamically-induced redox behavior will be given in Sections 7.7.

At this point, we can conclude, that ultrathin iron oxides films which are part of an oxide heterostructure behave thermodynamically very differently compared to bulk iron oxide. The altered parameters p_{O_2} and T_{anneal} of the phase transitions reflect the specific thermodynamic stability criteria, which are strongly affected by the substrate properties and the film thickness. Hence, we investigate the impact of the iron oxide film dimensionality (Section 7.5) and the oxide substrate (Section 7.6) on the reduction-oxidation processes in the following.

7.5 Annealing of ultrathin and bulk-like iron oxide films in UHV

Next, the effect of film dimensionality on the thermally-induced iron oxide phase formations will be evaluated. For this experiment, we chose two complementary iron oxide film thicknesses, ultrathin 2 nm and bulk-like 38 nm, both grown on Nb:$SrTiO_3$ (001) substrates. The thermal annealing was performed in UHV atmosphere, and the temperature was increased incrementally from RT to 700 °C.

7.5.1 HAXPES

Figure 7.6 (a) and (b) show the Fe 2p core levels at each annealing step of the 2 nm and 38 nm iron oxide films, respectively. Their spectral shapes are strongly altered with increasing T_{anneal}, which reflects the continuous reduction of the iron oxides films. Two major trends are notable: First, the alteration of the Fe satellite peak binding energy positions and intensities and, second, the intensity redistribution within the Fe $2p_{3/2}$ core level peaks.

For the ultrathin 2 nm film, as shown in Figure 7.6 (a), the Fe^{3+} satellite peaks at RT are attributed to the γ-Fe_2O_3 phase. With increasing $T_{anneal} = 200$-250 °C, the satellite peak merges into a mixed Fe^{3+}/Fe^{2+} feature, which indicates the – theoretically unexpected – reduction of γ-Fe_2O_3 to the Fe_3O_4 phase. For $T_{anneal} > 300$ °C, the pure Fe^{2+} satellite peak arises and indicates the formation of the FeO phase. If the annealing temperature T_{anneal} is higher than 500 °C, the Fe $2p_{3/2}$ core level peaks reveal the reduction of γ-Fe_2O_3 not

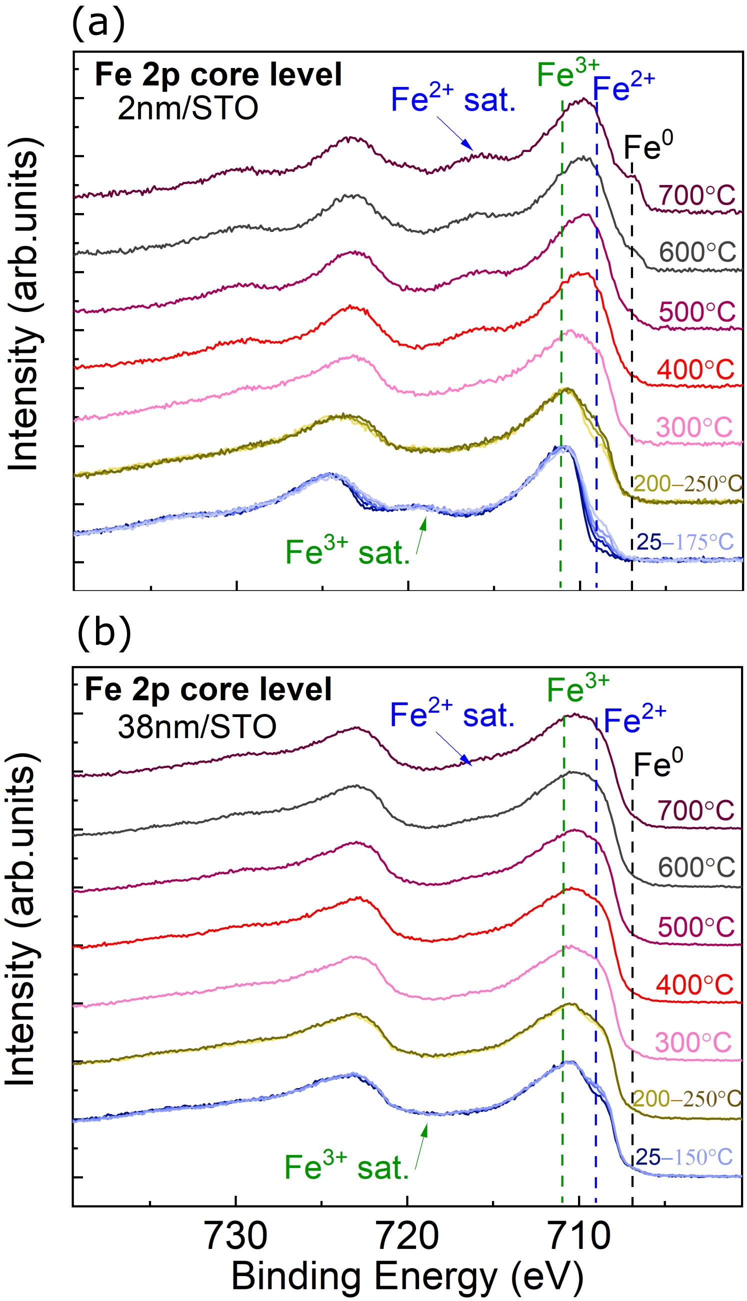

Figure 7.6: Fe 2p core level measured for films annealed at different temperature in UHV-atmosphere of thickness (a) 2 nm and (b) 38 nm.

only to FeO, but even to the Fe metal. In contrast, the spectra of the bulk-like film shown in Figure 7.6 (b) indicate the total reduction of Fe_3O_4 to FeO at the highest annealing temperature. Taking into account that the information depth is 25 nm, only the film itself, but not the buried substrate interface is probed by the HAXPES experiment.

7.5.2 Relative iron-compositions

By linear combination fitting (Section 7.3) of the Fe 2p spectra, we calculate the iron oxides phase ratio in both, the 2 nm and 38 nm, films and plot it as a function of the annealing temperature. As shown in Figure 7.7 (a), we find a continuous reduction from Fe_3O_4 to Fe metal with increasing temperature from RT to $T_{anneal} = 700\,°C$. The as grown 2 nm film at RT consists of a mixed iron oxide phase of 85 % γ-Fe_2O_3 and 15 % Fe_3O_4. By increasing the annealing temperature, a 100 % Fe_3O_4 phase is formed at $T_{anneal} = 200\,°C$. A further continuous reduction is observed by increasing T_{anneal}, and the film is totally reduced to FeO at $T_{anneal} = 400\,°C$. At $T_{anneal} > 500\,°C$, the Fe metal phase arises to achieve a 32 % ratio of the film annealed at $T_{anneal} = 700\,°C$. For the 38 nm film, in contrast, a much slower reduction of the iron oxides is observable, as shown in Figure 7.7 (b). At RT and not probing the substrate interface, we observe a 100 % Fe_3O_4 phase. By increasing T_{anneal}, the ratio of FeO increases gradually to 100 % at $T_{anneal} = 700\,°C$. We note, however, that no Fe metal phase formation is observed for the bulk-like sample.

7.5.3 Discussion

As we mentioned in the introduction of this chapter, the redox process within the oxide heterostructures occur at three relevant interfaces, i.e. (A) the outside atmosphere/Fe_xO_y film interface, (B) the interface between the phase-transformed Fe_xO_y/Fe_xO_y intralayer and (C) the Fe_xO_y/substrate interface. In this section, the experiment is chosen so that the first interface (A) is fixed (annealing in UHV) and the third interface (C) is chosen so that it is constant by using an identical substrate, $SrTiO_3$. Therefore, the main difference is in the interface (B). The two films with different thicknesses 2 and 38 nm have different internal oxygen diffusion strengths which can explain the slower iron oxide reduction observed for the 38 nm thick film as shown in Figure 7.8. As found in the previous section, the redox process is driven by two factors: the oxygen diffusion from the substrate to the film and from the film to the atmosphere. We find an additional factor in the film dimensionality itself, which reduces the oxygen diffusion through the film and thereby slows down the reduction process. Furthermore, the 38 nm thick film is much more bulk-like and thus less influenced by the substrate which puts the phase reactions much more closely to the bulk Fe/O phase diagram. Hence it is less reduced.

In the following, we need further understanding of the mechanism of thermally-activated oxygen diffusion from/to the substrate. We therefore compare the redox processes of iron oxide grown both on NSTO and on YSZ substrates, which strongly differ in their affinity

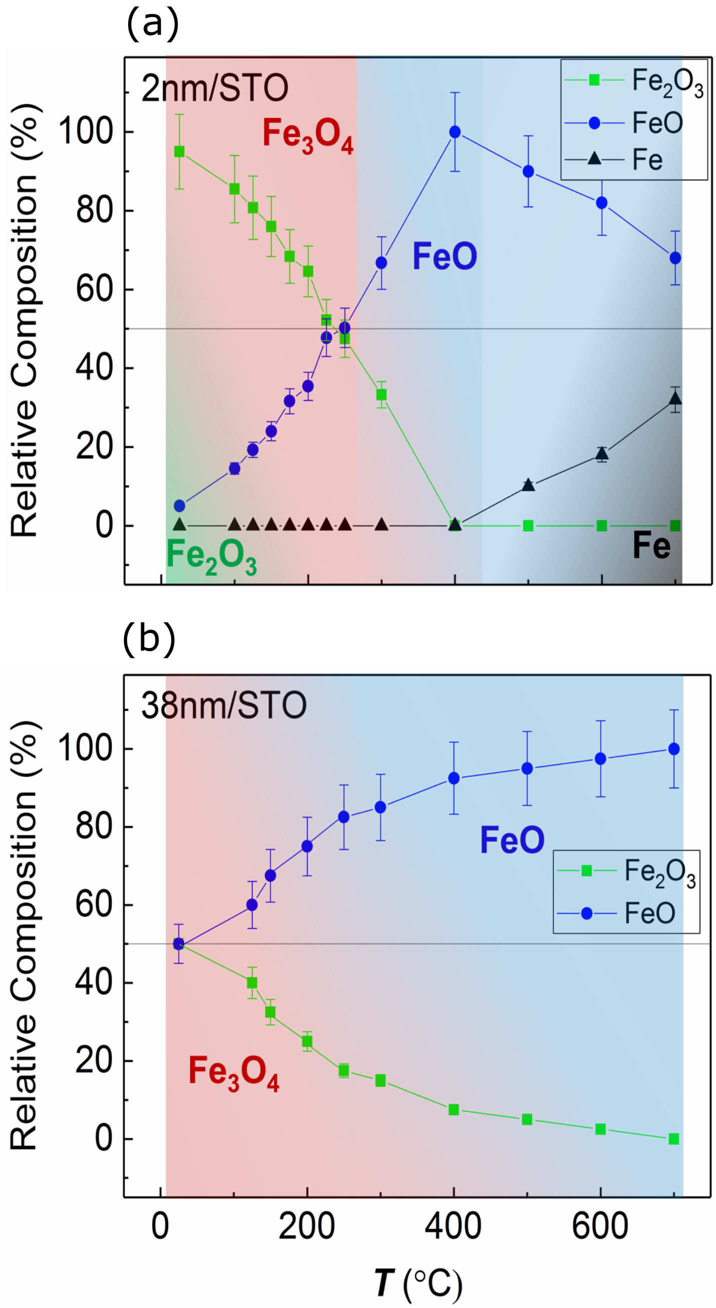

Figure 7.7: Iron oxides ratio vs. annealing temperature of films thicknesses (a) 2 nm and (b) 38 nm.

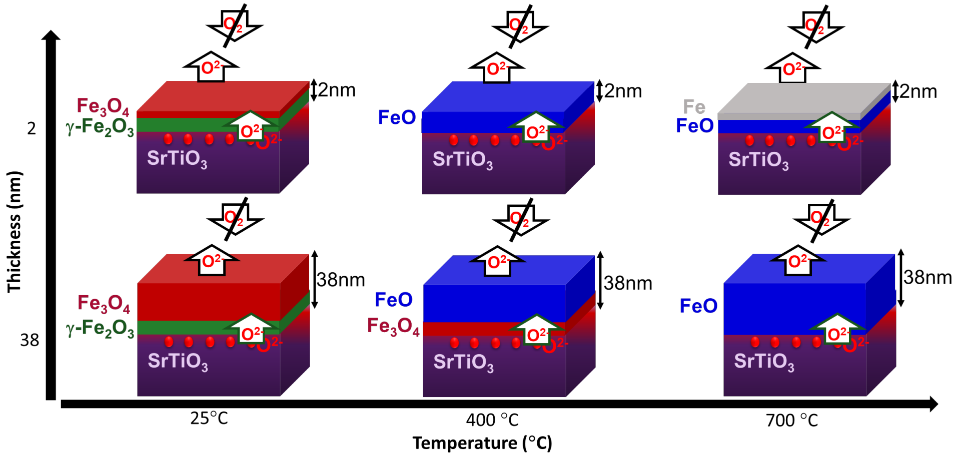

Figure 7.8: Schematics for 2 and 38 nm thick films grown on Nb:$SrTiO_3$ indicating the reduction of iron oxides after the annealing.

for chemical reduction as we discussed in Chapter 5 and Chapter 6. Hence, NSTO and YSZ substrates are expected to influence the oxidation of the overlaying iron oxide films differently.

7.6 Annealing of ultrathin iron oxides films on NSTO and YSZ substrates

To draw a comprehensive picture of the redox process in iron oxide heterostructures, the specific thermodynamic properties of the interface between substrate and Fe_xO_y are essential. Surprisingly, only very few growth and annealing studies of iron oxides on oxide substrates are available, and so far the focus has not been put on the substrate properties. X. Zhang et. al. [135] studied the effect of annealing on bulk-like iron oxides films grown on the Al_2O_3 substrate. The reduction and oxidation of iron oxides were found to essentially follow the standard iron oxides phase diagram [148]. On the other hand, the reduction of iron oxides grown on MgO substrates was found to not follow the standard iron oxides phase diagram [149]. Both observations suggest the strong impact of the oxide substrates on the interfacial redox process.

7.6.1 HAXPES

YSZ is known to be much less prone to reduction than Nb:$SrTiO_3$, thus, we expect that different interfacial iron oxide redox processes occur. Therefore, we compare two films of the same thickness (4 nm) grown on different oxide substrates, Nb:$SrTiO_3$ and YSZ.

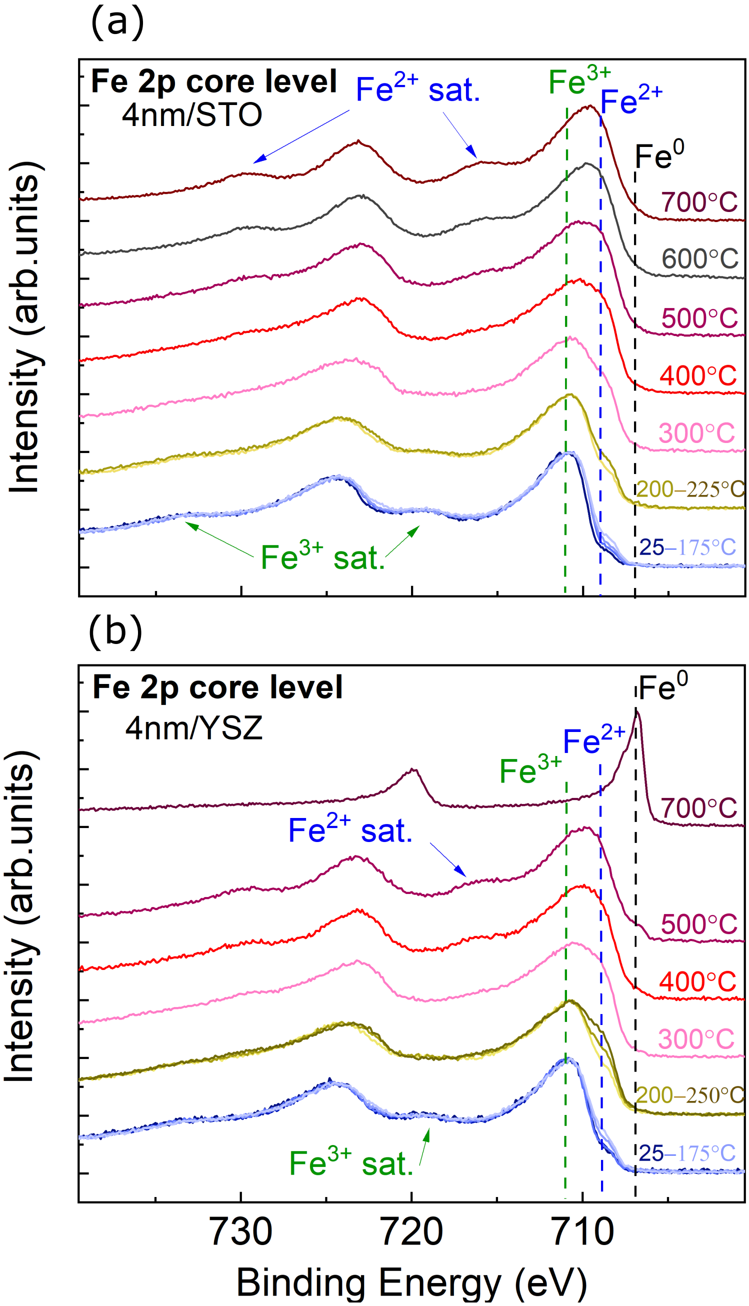

Figure 7.9: Fe 2p core level measured for films annealed at different temperature in UHV-atmosphere of thickness 4 nm grown on (a) Nb:$SrTiO_3$ and (b) YSZ.

Figure 7.9 (a) and (b) show the Fe 2p core levels of both samples measured during stepwise annealing in the UHV-atmosphere. Both Fe 2p spectra of the as-grown films at RT are quite similar, which was not expected as we discussed in Chapter 6. We now follow the positions of the satellite and Fe $2p_{3/2}$ core level peaks in Figure 7.9 (a) and (b) with continuous annealing from RT to $T_{anneal} = 700\,°C$:

(1) The Fe^{3+} satellite peak, which represents the formation of Fe_2O_3 phase, disappeared at $T_{anneal} = 300\,°C$ –indicating the formation of Fe_3O_4 phase– for the film grown on NSTO. However, it disappeared at a lower annealing temperature of $T_{anneal} = 200\,°C$ for the film grown on YSZ.

(2) The Fe^{2+} satellite peak, which represents the formation of FeO phase, appeared and enlarged with increasing annealing temperature up to $T_{anneal} = 700\,°C$ for the film grown on NSTO and $T_{anneal} = 400\,°C$ for the film grown on YSZ.

(3) Only for the film grown on YSZ, a complete reduction to the Fe metal phase is observed, which is detected by the strong shift of the Fe $2p_{3/2}$ core level peaks from 710 eV at RT to 707 eV at $T_{anneal} = 700\,°C$.

7.6.2 Relative iron-compositions

The quantitative linear combination analysis of temperature-induced iron phase transitions is summarized in Figure 7.10 (a) and (b). For the film grown on the NSTO substrate, we find the formation of a 100 % Fe_3O_4 phase at $T_{anneal} = 300\,°C$. For the film grown on the YSZ substrate, in contrast, a lower annealing temperature of 200 °C is sufficient to form 100 % Fe_3O_4, which is the temperature required for the reduction of a 2 nm iron oxide film grown on Nb:$SrTiO_3$, as shown in Section 7.5.

Following the transition line of reduction of the FeO phase in Figure 7.10 (a), $T_{anneal} = 700\,°C$ is needed to fully reduce γ-Fe_2O_3 and Fe_3O_4 to form 100 % FeO on NSTO substrates. For YSZ substrates, a lower temperature $T_{anneal} = 400\,°C$ is sufficient to form the 100 % reduced 4 nm FeO/YSZ as shown in Figure 7.10 (b). Surprisingly, we find a fully reduced Fe metal phase for YSZ substrates at $T_{anneal} = 700\,°C$, which is not achieved even for 2 nm film grown on NSTO (only 32 % Fe metal content).

7.6.3 Discussion

As summarized in the schematics in Figure 7.11, the iron oxides phase transition induced by annealing is strongly influenced by the oxide substrates, NSTO and YSZ. The film grown on YSZ is reduced quickly to FeO and even to Fe metal which was not even achieved by the annealing of 2 nm/NSTO at 700 °C. Thereby, our findings provide strong evidence for an active participation of the oxide substrates in the redox process – which behave far from being inert. To understand the role of the oxide substrates as additional oxygen supplier or scavenger, we need to consider the thermodynamic aspects of the

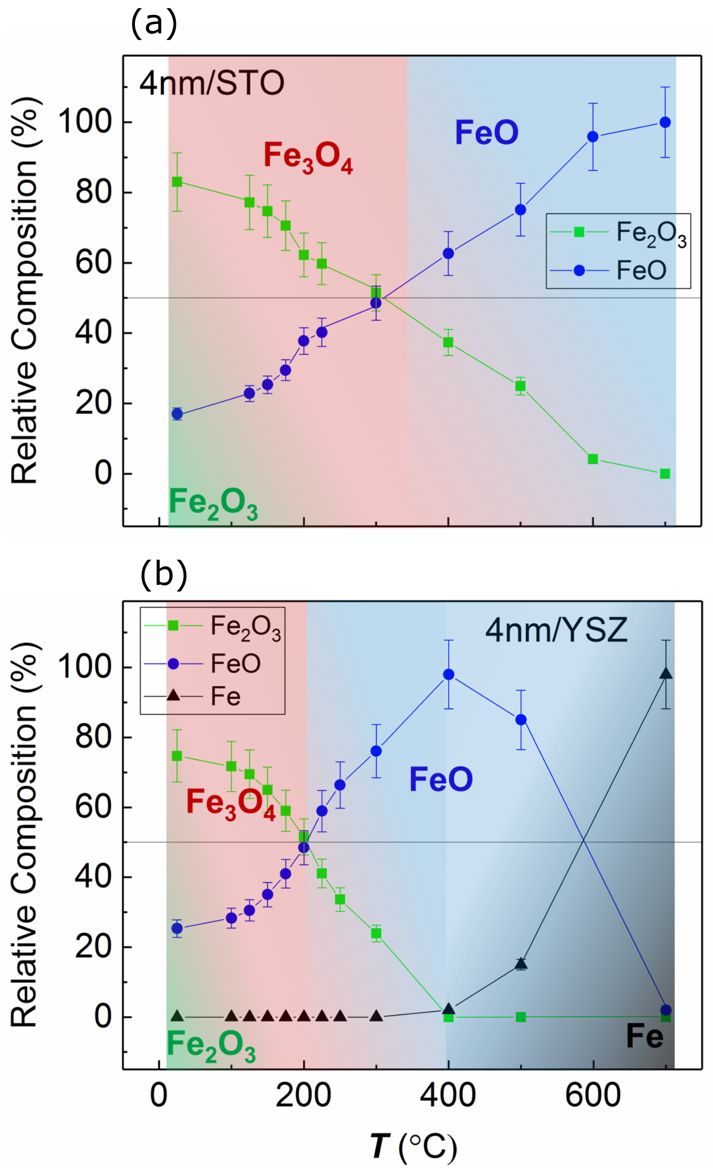

Figure 7.10: Iron oxides ratio vs. annealing temperature of films grown on (a) Nb:$SrTiO_3$ and (b) YSZ.

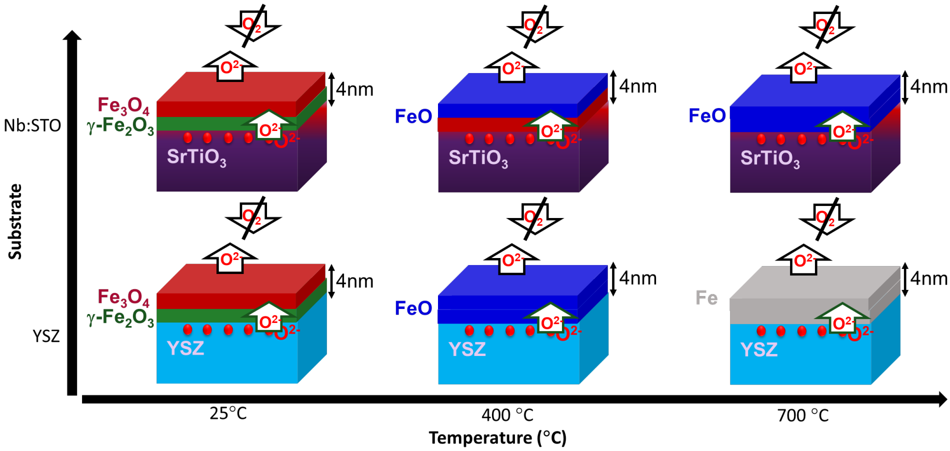

Figure 7.11: Schematics for 4 nm thick iron oxides films grown on Nb:SrTiO$_3$ and YSZ substrates indicating the reduction of iron oxides by annealing.

interfacial redox processes in the iron oxide heterostructures as we will discuss in the next Section 7.7.

7.7 Thermodynamics analysis

In order to understand the thermally driven phase transitions from γ-$Fe_2O_3 \rightarrow Fe_3O_4 \rightarrow FeO \rightarrow Fe$, we perform a thermodynamic analysis to determine the different emerging phase equilibria. The (opposing) reduction-oxidation reactions allow for three different possible phase equilibria

$$\text{①}\ 3Fe_2O_3 \rightleftharpoons 2Fe_3O_4 + \frac{1}{2}O_2 \tag{7.7.1}$$

$$\text{②}\ Fe_3O_4 \rightleftharpoons 3FeO + \frac{1}{2}O_2 \tag{7.7.2}$$

$$\text{③}\ FeO \rightleftharpoons Fe + \frac{1}{2}O_2. \tag{7.7.3}$$

7.7.1 The van ’t Hoff analysis

We use the classical van ’t Hoff analysis to identify the effect of the oxide substrate on the redox processes and emerging iron oxide phases. The change of Gibbs free energy

ΔG^0, and thus of the enthalpy ΔH as well as entropy ΔS is calculated by the van 't Hoff equation,

$$\ln(K) = -\frac{\Delta G^0}{RT} = -\frac{\Delta H}{RT} + \frac{\Delta S}{R} \quad , \tag{7.7.4}$$

whereby R is the gas constant and K denotes the equilibrium constant of the equilibria 7.7.1, 7.7.2 and 7.7.3, respectively. Therefore, K is directly related to the Fe, Fe^{2+} and Fe^{3+} cation ratios, which we determined from the HAXPES peak fitting analysis as we explained in Section 7.3.

From the first equilibrium 7.7.1,

$$3[2Fe^{3+} + 3O^{2-}] \rightleftharpoons 2[Fe^{2+} + 2Fe^{3+} + 4O^{2-}] + \frac{1}{2}O_2 \quad , \tag{7.7.5}$$

we derive

$$K_{①} = \frac{[Fe^{3+}]^4\,[Fe^{2+}]^2\,[O^{2-}]^8}{[Fe^{3+}]^6\,[O^{2-}]^9}\; p_{O_2eff}^{\frac{1}{2}} \quad , \tag{7.7.6}$$

where, p_{O_2eff} is the effective oxygen pressure of the heterostructure, i.e substrate, film and atmosphere. We reorganize the equation to

$$K_{①} = \left[\frac{Fe^{2+}}{Fe^{3+}}\right]^2 p_{O_2eff}^{\frac{1}{2}} = K_{red①} \times p_{O_2eff}^{\frac{1}{2}} \quad . \tag{7.7.7}$$

For the second equilibrium 7.7.2 we derive

$$Fe^{2+} + 2Fe^{3+} + 4O^{2-} \rightleftharpoons 3[Fe^{2+} + 3O^{2-}] + \frac{1}{2}O_2 \quad , \tag{7.7.8}$$

$$K_{②} = \frac{[Fe^{2+}]^3\,[O^{2-}]^3}{[Fe^{2+}]\,[Fe^{3+}]^2\,[O^{2-}]^4}\; p_{O_2eff}^{\frac{1}{2}} \quad , \tag{7.7.9}$$

$$K_{②} = \left[\frac{Fe^{2+}}{Fe^{3+}}\right]^2 p_{O_2eff}^{\frac{1}{2}} = K_{red②} \times p_{O_2eff}^{\frac{1}{2}} \quad . \tag{7.7.10}$$

For the third equilibrium 7.7.3 we derive

$$Fe^{2+} + O^{2-} \rightleftharpoons Fe^0 + \frac{1}{2}O_2 \quad , \tag{7.7.11}$$

$$K_{③} = \frac{[Fe^0]}{[Fe^{2+}]\,[O^{2-}]}\; p_{O_2eff}^{\frac{1}{2}} \quad , \tag{7.7.12}$$

$$K_{③} = \left[\frac{Fe^0}{Fe^{2+}}\right] p_{O_2eff}^{\frac{1}{2}} = K_{red③} \times p_{O_2eff}^{\frac{1}{2}} \quad . \tag{7.7.13}$$

In order to calculate K for the different reactions, we proceed by determining the effective pressure $p_{O_{2eff}}$ as an important system parameter. The effective pressure $p_{O_{2eff}}$ consists not only of the supplied external oxygen background pressure, but also of the contributions of oxide substrate. If we assume for a moment that the effect of the substrate and

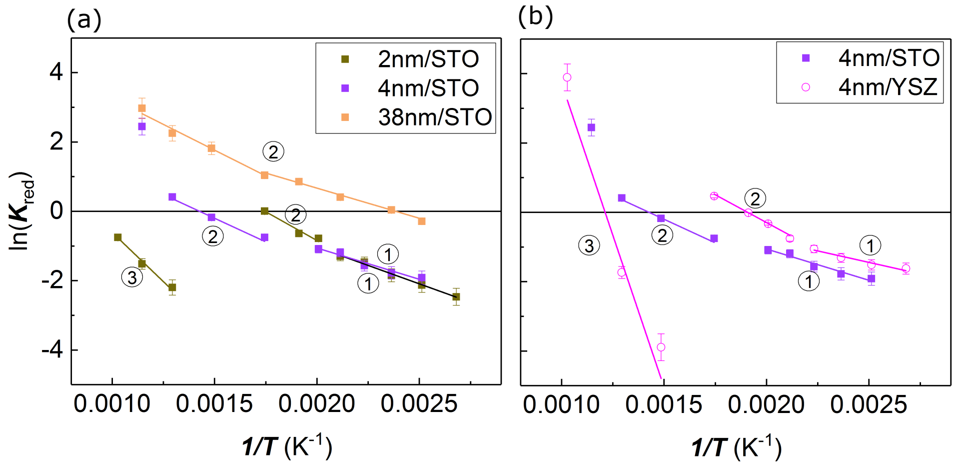

Figure 7.12: Van 't Hoff plot of thermal phase equilibrium for (a) 2 nm, 4 nm and 38 nm thick iron oxide films grown on Nb:$SrTiO_3$ and (b) 4 nm thick iron oxide films grown on Nb:$SrTiO_3$ and YSZ substrates.

film is negligible, we have a constant effective oxygen atmospheric background pressure, which drives the redox reactions. If we attribute it to unity, we can compare the general behavior of the van 't Hoff plot $\ln(K_{red})$ vs. $1/T$ as it is depicted in Figure 7.12, where,

$$K_{red①②} = \left[\frac{Fe^{2+}}{Fe^{3+}}\right]^2 \text{ and } K_{red③} = \left[\frac{Fe^{0}}{Fe^{2+}}\right] \quad . \tag{7.7.14}$$

A negative slope is observed for all three reactions, which is indicative of an endothermic reaction ($\Delta H > 0$).

In Figure 7.12, we can identify two or three different slopes, each of which suggests that the respective reactions 1,2 and 3 undergo different energetics. For example, the van 't Hoff plot of a 2 nm film grown on NSTO (Figure 7.12 (a)) comprises of three different slopes, which refer to the three reduction reactions for which the respective iron oxide phase is in equilibrium. In contrast, the van 't Hoff plot of a 38 nm film grown on NSTO has two different slopes, but only one reduction reaction 7.7.2 is present. Two different reasons can explain the occurrence of these two slopes: first, the different energetic reduction equilibria may slow down at high temperatures and second, the chemical behavior of the interface is not accessible by HAXPES, if we consider the depth information of 25 nm.

7.7.2 Thermodynamics parameters with unity effective oxygen pressure

As a first approximation we set the effective oxygen pressure to unity and calculate K_{red}. Then, we calculated the enthalpy ΔH and the entropy ΔS according to Equation 7.7.4 for all the samples, as shown in Table 7.1. The calculated values of the enthalpy and the entropy are far away from the theoretical values: for the reaction ①, 242.5 kJ/mol and 132.7 J/molK, for the reaction ②, 316.2 kJ/mol and 118.4 J/molK, and for the last reaction ③ −258.7 kJ/mol and 84.4 J/molK, respectively. The deviation of the thermodynamics parameters from the theoretical values may be caused by the effective oxygen pressure, which we set to unity.

Table 7.1: Thermodynamics parameters calculated from $ln(K_{red})$ vs. $1/T$.

Film	Reaction	Enthalpy Δ H (kJ/mol)	Entropy Δ S (J/molK)
2 nm/STO	①	35.32±1.9	53.5±4.5
2 nm/STO	②	55.11±6.8	96.2±11.9
2 nm/STO	③	47.19±4.3	42.1±4.7
4 nm/STO	①	25.64±2.1	32.6±4.2
4 nm/STO	②	57.52±22.97	82.5±33.5
4 nm/STO	③	....	....
4 nm/YSZ	①	22.02±3.3	31.1±7.98
4 nm/YSZ	②	53.29±3.9	101.7±7.6
4 nm/YSZ	③	145.8±33.4	176.8±43.1
38 nm/STO	①	....	....
38 nm/STO	②	31.16±2	74.2±3.8
38 nm/STO	③	....	....

7.7.3 Thermodynamics parameters considering the effective oxygen pressure

The effective oxygen pressure $p_{O_{2eff}}$ – reflecting the total O_2 contribution from substrate, film and atmosphere – cannot be measured directly. Obviously, additional $p_{O_{2eff}}$ provided by the oxide substrate enhances the externally provided gaseous oxygen p_{O_2}, and thus significantly alters the thermodynamics of the heterostructure. To elaborate this situation, we calculated $p_{O_{2eff}}$ for our samples from the Equations 7.7.4, 7.7.5 and 7.7.6,

$$p^{\frac{1}{2}}_{O_{2eff}} = \frac{exp\left(-\frac{\Delta G^0}{RT}\right)}{K_{red}} \tag{7.7.15}$$

with ΔG^0 being a function of temperature. For the three possible phase equilibria ①, ② and ③, we calculated ΔG^0 as follows

$$\Delta G^0_{①}(T) = 2\,G^0_{Fe_3O_4}(T) + \frac{1}{2}\,G^0_{O_2} - 3\,G^0_{Fe_2O_3}(T) \quad , \tag{7.7.16}$$

$$\Delta G^0_{②}(T) = 3\,G^0_{FeO}(T) + \frac{1}{2}\,G^0_{O_2} - G^0_{Fe_3O_4}(T) \quad , \tag{7.7.17}$$

$$\Delta G^0_{③}(T) = G^0_{Fe}(T) + \frac{1}{2}\,G^0_{O_2} - G^0_{FeO}(T) \quad . \tag{7.7.18}$$

The Gibbs free energies $G^0_{Fe_2O_3}(T)$, $G^0_{Fe_3O_4}(T)$, $G^0_{FeO}(T)$, $G^0_{Fe}(T)$ and $G^0_{O_2}$ are calculated from the NIST database [48]. Table 7.2 shows the standard values for the Gibbs formation energy, enthalpy, and entropy of the different iron oxides calculated at room temperature. The respective Gibbs formation energy for each equilibrium as a function of temperature and the values at room temperature are given in Table 7.3. Subsequently, we calculated the effective oxygen pressure and compare it to the standard phase diagram as we will discuss in the following Section.

Table 7.2: Standard thermodynamics parameters calculated from the NIST database [48] at room temperature.

	G^0 (kJ/mol)	$\Delta_f H^0$ (kJ/mol)	S^0 (J/molK)
Fe_2O_3	-851.55	-863.21	87.28
Fe_3O_4	-1164.21	-1163.34	145.17
FeO	-290.15	-286.74	60.72
Fe	-20.54	-12.4	27.31

Table 7.3: The calculated Gibbs formation energy of the three equilibria at room temperature.

$\Delta G^0_{①}$ (kJ/mol)	$\Delta G^0_{②}$ (kJ/mol)	$\Delta G^0_{③}$ (kJ/mol)
256.996	324.513	300.356

7.7.4 The calculated effective oxygen pressure and the standard phase diagram: adjusted phase diagram

As we explained in the previous sections, the thermodynamics parameters for the different iron oxide phase transitions are not in line with the standard phase diagram for freestanding bulk iron oxides (Figure 7.13 (a)). The only independent variable is the effective oxygen pressure $p_{O_{2eff}}$. In the next step, we compare the results discussed in the previous section with the standard phase diagram of iron oxides shown in Figure 7.13 (a). We find that the effective oxygen pressure determined by Equation 7.7.15 can be as low as 10^{-48} mbar, which means the standard phase diagram needs to be extended.

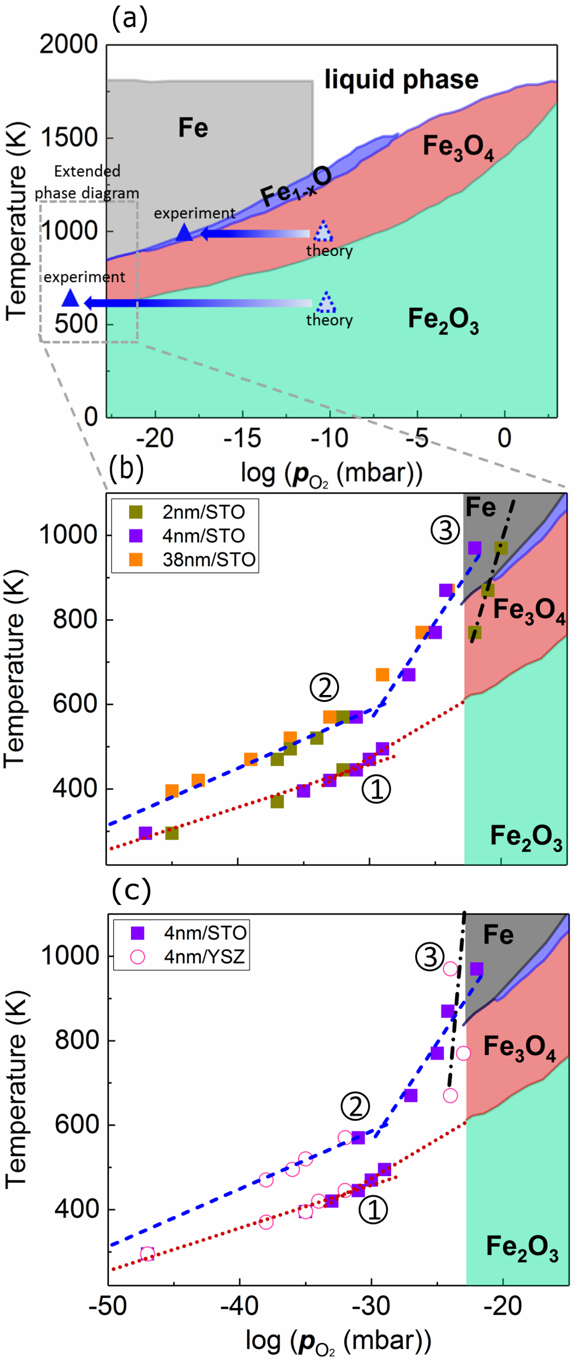

Figure 7.13: (a) The standard temperature-pressure phase diagram of (freestanding) iron oxides [148]. Triangles show exemplariliy the deviation from experimental results for the system 4 nm/NSTO (see Section 7.4). (b) and (c) Adjusted phase diagram for Fe_xO_y/Nb:$SrTiO_3$ and Fe_xO_y/YSZ heterostructures: Effective oxygen pressure $p_{O_{2eff}}$ calculated from Equation 7.7.15 – reflecting the total O_2 supply from substrate, film and atmosphere – set into relation to the standard phase diagram (shaded areas) for the systems 2 nm Fe_xO_y/Nb:$SrTiO_3$, 4 nm Fe_xO_y/Nb:$SrTiO_3$, 38 nm Fe_xO_y/Nb:$SrTiO_3$ and 4 nm Fe_xO_y/YSZ.

The calculated effective oxygen partial pressure for all systems is depicted in Figure 7.13 (b-c) and set into relation to the standard phase diagram (shaded areas). We notice that the effective oxygen pressure for each system is changing with temperature, which is not possible if we attribute the effective oxygen pressure to the atmosphere only. This gives another proof for the significant contribution of the substrates to $p_{\mathrm{O}_{2eff}}$.

For the sample 2 nm Fe_xO_y/Nb:$SrTiO_3$ annealed in UHV atmosphere, we find a partial reduction from γ-Fe_2O_3 and Fe_3O_4 phases to Fe metal at an annealing temperature of 700 °C (Figure 7.13 (b)). The calculated effective oxygen pressure ranges from 10^{-45} to 10^{-20} mbar with increasing the temperature from room temperature to 700 °C, respectively. We also calculated the effective oxygen pressure for the 4 nm and 38 nm Fe_xO_y/Nb:$SrTiO_3$ samples annealed in UHV, as shown in Figure 7.13 (b). We can fit three lines to the data indicating all the three possible phase equilibria ①, ② and ③.

As a major result, we find that the stability regions for the three different iron oxide phases reveal a very consistent trend for all samples 2 nm Fe_xO_y/Nb:$SrTiO_3$, 4 nm Fe_xO_y/Nb:$SrTiO_3$ and 38 nm Fe_xO_y/Nb:$SrTiO_3$. This finding strongly underlines that the NSTO substrate alters the oxygen contents of the heterostructure during the annealing process: Firstly, the phase transition stability is scaling linearly with temperature and secondly, such a low $p_{\mathrm{O}_{2eff}}$ is not accessible by the typical experimental means.

As shown in Figure 7.13 (c), we find a complete reduction to Fe metal at an annealing temperature of 700 °C for the second system, 4 nm Fe_xO_y/YSZ annealed in UHV atmosphere. The effective oxygen pressure at 700 °C is $p_{\mathrm{O}_{2eff}} = 10^{-23}$ mbar, which is even lower than the one for the Nb:$SrTiO_3$ substrates. As expected, the YSZ substrate is not supplying oxygen to the heterostructure during annealing in UHV (even though being a good oxygen conductor) - in contrast to the NSTO substrate, which readily supplies oxygen during annealing.

Our findings of a specific phase diagram for the all-oxide systems Fe_xO_y interfaced to Nb:$SrTiO_3$ and YSZ open up the door for investigations of a multitude of further all-oxide heterostructures, and for theoretical temperature-pressure calculations of material-specific phase diagrams.

7.8 Conclusion

We study the thermally induced phase transformation from Fe_3O_4 to γ-Fe_2O_3 and FeO ultrathin iron oxide films interfaced with Nb:$SrTiO_3$ and YSZ substrates.

The phase transitions strongly differ from the standard phase diagram of bulk-like free-standing iron oxides and are significantly modulated by reduction-oxidation processes within the all-oxide heterostructures.

We systematically investigated the redox processes i) under different ambient conditions during annealing in an external oxygen supply and UHV, ii) for different iron oxide film thicknesses and iii) for two complementary oxide substrates, Nb:SrTiO$_3$ and YSZ to identify the specific role of the substrates, in terms of oxygen reducibility.

In particular, we show that the redox processes occur at three relevant interfaces, i.e. (A) the outside atmosphere/Fe$_x$O$_y$ film interface, (B) the interface between phase-transformed Fe$_x$O$_y$/Fe$_x$O$_y$ intralayer and (C) the Fe$_x$O$_y$/substrate interface.

As the most important system parameter, we identify as the effective oxygen pressure, which reflects the total oxygen supply including the oxide substrate, the iron oxide film itself and the externally supplied oxygen. By analyzing depth-dependent HAXPES spectra in a comprehensive thermodynamic analysis, we could calculate the temperature-pressure dependence of the ion oxide phase transitions as part of oxide heterostructures.

We reveal an almost complete deviation from the standard Fe$_x$O$_y$ temperature-pressure phase diagram, and present an altered and specific phase diagram for the all-oxide systems Fe$_x$O$_y$/Nb:SrTiO$_3$ and Fe$_x$O$_y$/YSZ. These results reveal convincingly that the "active" oxide substrates make the most important contribution to the redox process, and prove the need for many further studies on specific all-oxide systems and a theoretical backing.

CHAPTER 8

Conclusion and Outlook

Motivated by the interesting properties of the magnetite and the different iron oxides phases, the main goals of this thesis are (1) investigating the electronic and magnetic properties of the iron oxide/substrate interfaces, (2) understanding of the interfacial thermodynamic properties, (3) controlling the redox process and (4) tuning the electronic and magnetic properties of Fe_xO_y films grown on "active" oxide substrates. To accomplish these goals, we synthesized a series of Fe_3O_4 films by pulsed laser deposition (PLD) at different growth temperatures T_{growth} ranging from 200 up to 500 °C with film thicknesses d of 2-38 nm. The films are grown on two different oxide substrates YSZ and $SrTiO_3$. Many techniques have been used to investigate the structural, morphological, magnetic, and electronic properties. We now summarize the main results of this thesis.

High-quality Fe_3O_4 films grow epitaxially on $SrTiO_3$ substrates despite the large lattice mismatch of $-7.5\,\%$

A series of Fe_3O_4 films have been grown with a thickness of d=38 nm at different growth temperatures T_{growth}=200-500 °C. The quality of Fe_3O_4 films (100) on $SrTiO_3$ (100) was assured by different techniques. Low surface roughness and high crystallinity have been observed for all films. Additionally, the Verwey transition was detected around 120 K indicating the formation of the stoichiometric Fe_3O_4 phase.

Growth-induced lattice strain

The XRD measurements indicate that the Fe_3O_4 films grown at different temperatures show different out-of-plane lattice constants: (I) tensile strain ($T_{growth} = 500\,°C$), (II) absence of strain ($T_{growth} = 400\,°C$) and (III) compressive strain ($T_{growth} = 350\,°C$).

Tunable magnetic easy axis switching

The Fe_3O_4 film grown on $SrTiO_3$ substrate at T_{growth}=350 °C (compressive strain) has a magnetic easy axis switching from the ideal bulk direction [110] to [100] at room temperature and Verwey transition. However, a tunable switching of the magnetic easy axis is observed for the Fe_3O_4 film grown on $SrTiO_3$ substrate at T_{growth}=500 °C (tensile strain). The Fe_3O_4 film shows an easy axis direction of [100] at room temperature. Switching for the magnetic easy axis to [110] is detected at the Verwey transition. This means that with careful optimization for growth temperature and substrate choices (Nb:STO), we can tune the anisotropy of the thin films.

Formation of an interfacial ferrimagnetic γ-Fe_2O_3 layer of 2 u.c. in the Fe_3O_4/$SrTiO_3$ heterostructures

In order to study the effect of reduced dimensionality on the electronic and magnetic properties of the films and interfaces, we grew Fe_3O_4 films on TiO_2-terminated Nb:$SrTiO_3$ substrates at T_{growth}=400 °C and with different film thickness in the range of d=2-38 nm. The Verwey transition is detected for all the films down to the ultrathin film of d=2 nm. It decreases strongly to 25 K for the 2 nm thick film. The HAXPES and XMCD measurements reveal the formation of an interfacial ferrimagnetic γ-Fe_2O_3 layer of 2 u.c. in the Fe_3O_4/$SrTiO_3$ heterostructures, independent of the total film thickness.

$SrTiO_3$ substrate-induced interface oxidation

The formation of an oxidized γ-Fe_2O_3 intralayer is due to the diffusion of oxygen across the TiO_2 termination. The oxygen-deficient $SrTiO_3$ surface is changing the surface Gibbs formation energy which thermodynamically allows the diffusion of oxygen towards the Fe_3O_4 films.

YSZ substrate-assisted interface oxidation

We grew Fe_3O_4 on YSZ at different growth temperature T_{growth} = 300-500 °C and with different thicknesses d = 4-38 nm. YSZ substrate which is known to be an "inert" substrate induces an oxidized phase Fe_2O_3 at the Fe_3O_4/YSZ interface. The formation of the oxidized Fe_2O_3 intralayer can be explained by either (1) an interfacial redox reaction that arises at some particular level of doping of Y_2O_3 or (2) diffusion of oxygen through the substrate from the outside atmosphere. Our annealing studies support the second mechanism to be the origin of interfacial oxidation.

Thermally-induced phase transformation from Fe_3O_4 to γ-Fe_2O_3 and FeO

By annealing in different temperatures and oxygen environments, we were able to tune the magnetic properties of the films from the ferrimagnetic phases γ-Fe_2O_3 and Fe_3O_4 to the antiferromagnetic phase FeO. The phase transitions strongly differ from the standard Fe_xO_y temperature-pressure phase diagram and are significantly modulated by the reduction-oxidation processes within the all-oxide heterostructures.

Identifying the effective oxygen pressure in the heterostructures and adjusted phase diagram

We show the redox process at three relevant interfaces: (A) the outside atmosphere/Fe_xO_y film interface, (B) the interface between phase-transformed Fe_xO_y/Fe_xO_y intralayer, and (C) the Fe_xO_y/substrate interface. Accordingly, the effective oxygen pressure is identified. An adjusted phase diagram for all-oxides heterostructures, Fe_xO_y/Nb:$SrTiO_3$ and Fe_xO_y/YSZ is presented. These results reveal convincingly that the "active" oxide substrates make the most important contribution in the redox process, and prove the need for many further studies on specific all-oxide systems and a theoretical background.

Summary and outlook

Our study goes beyond the current understanding of phase transitions in oxide heterostructures and paves the way towards a most sensitive tuning between different magnetic iron oxide phases – and thereby between magnetic and electronic functionalities. In general, this novel approach opens up the route towards tuning physical functionalities in all-oxide heterostructures by a controlled thermal phase design.

Many new aspects arose from the experiments presented in this thesis and require further investigations. We will point out some of the open topics and some suggestions.

Theoretical calculations for the distortion of the tetrahedral and octahedral sites caused by strain

The distortion of the tetra- and octahedral sites in addition to the particular distribution of the anti-phase boundaries (APBs) causes switching of the easy axis. The oxidized γ-Fe_2O_3 phase at the interfaces may support this switching, however, more theoretical calculations are still needed. In addition experiments are needed to assess the strain effect on the easy axis, for example, (1) reciprocal space mapping (RSM) to calculate the in-plane and out-of-plane lattice constant, (2) angle dependent-magnetoresistance or magneto-optic Kerr effect (MOKE) which are sensitive techniques to identify the magnetic easy axis direction, (3) transmission electron microscope (TEM) which is capable of imaging the APBs together with the in-plane and out-of-plane lattice distortion, and (4) spin-resolved photoemission electron microscopy (SP-PEEM) for spin-polarization mapping of the APBs and magnetic domains of Fe_3O_4/$SrTiO_3$ systems.

Reversible oxidation-reduction process at the interfaces

Controlled reversibility of the interfacial phase transformations of Fe_xO_y films on oxide substrates is the next remaining topic. To have one complete picture about the reversibility of the redox process, first the reduction process which takes place by annealing in the UHV-atmosphere needs to be monitored (achieved in Chapter 7). Second, the reoxidation process by annealing with step-wise oxygen dosing is suggested. Third, monitoring the chemical composition in the entire heterostructures, in particular, the film oxidation state together with the substrate (Ti core levels) needs to be employed using hard and

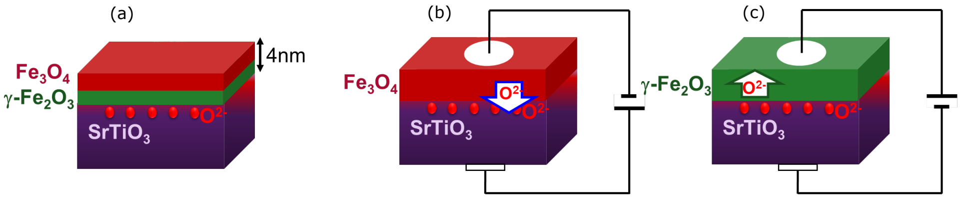

Figure 8.1: Schematic representation of (a) pristine state of the 4 nm thick film with mixed γ-Fe_2O_3 and Fe_3O_4 phases, (b) low resistance state with interfacial oxygen diffusion and reduction of γ-Fe_2O_3 to Fe_3O_4 phase, (c) high resistance state with interfacial oxygen diffusion and oxidation of Fe_3O_4 to γ-Fe_2O_3 phase.

soft x-rays techniques (HAXPES and XMCD) together with in-situ annealing and oxygen dosing.

Possible resistive switching devices accompanied by magnetization switching

By controlling the oxygen diffusion through the interfaces from and to the γ-Fe_2O_3 and Fe_3O_4 layers and Nb:$SrTiO_3$ substrates, we can switch between the iron phases and achieve resistive switching as well as magnetic switching. Applying an electric field promotes the oxygen ions migration through the interfaces. Consequently, the oxygen stoichiometry of the film changes. By proper control of the electric field, full reduction to Fe_3O_4 or full oxidation to γ-Fe_2O_3 may be achieved as shown in Figure 8.1. Fe_3O_4 is a conductor at room temperature and ferrimagnetic material ($4\,\mu_B$/f.u.), however, γ-Fe_2O_3 is an insulator and ferrimagnetic material ($2.5\,\mu_B$/f.u.). This may be a starting point for possible resistive and magnetic switching.

Appendix

A.1 XRR simulation

X-ray reflectivity (XRR) is used to measure the thickness of the film and the roughness of the surface and interface. Additionally, it may be used to estimate the densities of the film and substrate.

The values of the density and roughness extracted from the XRR spectra may have a large error. Thus, proper alignment for the experiment geometry is needed. However, the geometry of the experiment is not critical for the determination of the film thickness.

Sample alignment

Figure A.1 represents the geometry of the XRR experiment. In XRR, the X-ray beam is incident on a sample with an angle ω and reflects with an angle θ. If the sample has a perfect surface, the X-ray beam reflects with an angle $\theta = \omega$. If the samples are tilted with an offset angle of ω', we have to take into account this angle and in this case $\theta \neq \omega$. To solve this problem, proper alignment for the samples is needed.

1. We align the sample surface to be parallel to the incident X-ray ($\theta = 0°$).

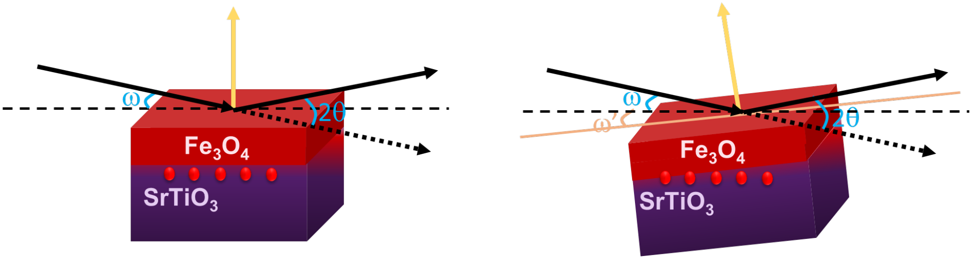

Figure A.1: Schematics representation of the XRR geometry without and with sample offset ω'.

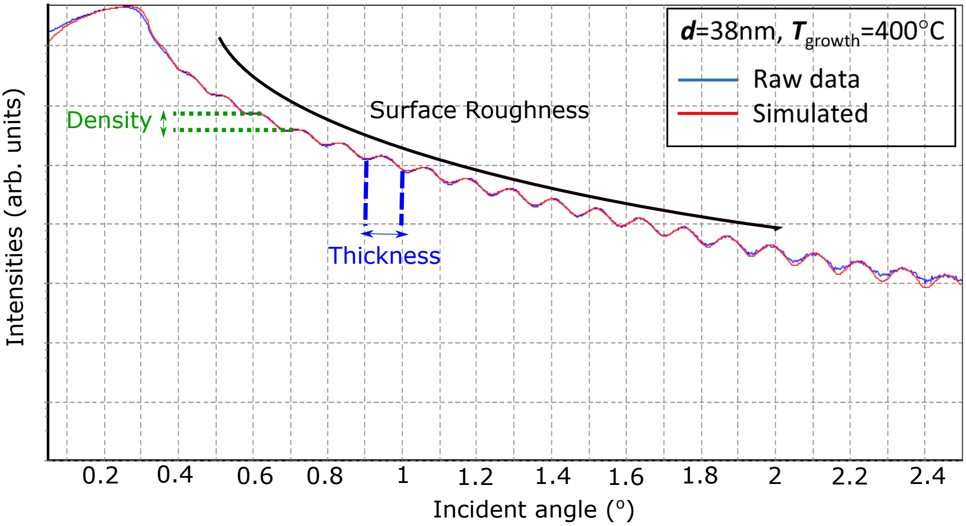

Figure A.2: The experimental data of X-ray reflectivity of 38 nm thick Fe_3O_4 film grown at temperature T_{growth}=400 °C (solid blue line) and the simulated spectra using the software X'Pert Reflectivity (solid red line).

2. We adjust the offset by measuring the rocking curve (ω scan at fixed θ) of the samples around the critical angle of $SrTiO_3$.

   The critical angle is the angle where a total reflection for the X-ray beam occurs. For $SrTiO_3$, it is around $\theta = 0.2°$.

   The maximum of the rocking peak equals $\theta + \omega'$.

3. We then can add the ω' in the X'Pert Reflectivity software for proper calculations to the density and roughness.

XRR curve

In XRR, the incident X-rays –with very low angles– reflect, interfere and form oscillations. Those oscillations are related to the different materials interfaced with the substrate.

1. The amplitude of the oscillations is due to the electron density as shown in Figure A.2. The larger differences between the substrate and film densities mean higher amplitude.
2. The distance between two consecutive oscillations is related inversely to the thickness of the films. The thicker film gives a shorter distance.
3. The rate of signal decay (slope) is assigned to the surface roughness. A larger roughness results in a faster decay.

4. The smeared out oscillations at high angles are related to the surface and interface roughness.

XRR simulation

To extract this important information from the XRR scans, we use the X'Pert Reflectivity software. An exemplary XRR scan of Fe_3O_4 38 nm thick film grown at temperature T_{growth}=400 °C is shown in Figure A.2 (solid blue line). The simulated spectra using the software X'Pert Reflectivity is shown in the solid red line. The simulated data agree very well the experimental data. However, the simulation procedure is far from trivial.

1. We have to provide the program with initial parameters to start the fitting. The densities of the Fe_3O_4 film and $SrTiO_3$ substrate are 5.17 gm/cm^3 and 5.12 gm/cm^3, respectively. The thickness of the substrate is set to 600000 nm. The film thickness and the roughness of the surface and interface are set differently for each film separately. For the exemplary XRR scan shown here, the thickness of the film is set initially to 38 nm and the roughness of the surface and interface to 0.6 nm, and 0.2 nm, respectively.

2. We are doing the fitting of the spectra step by step,

    - fixing all the parameters except the thickness, we choose the thickness to be in the range of 35 nm to 41 nm,

    - fixing all the parameters except the film thickness and the roughness of both surface and interface,

    - in the last step, fixing all parameters except, the film thickness, the roughness, and the densities of the films and substrate.

      We should be careful that the densities may have large errors again because of the sample alignment.

3. The fitted data sometimes does not perfectly match the experimental data. This may be attributed to the sample alignment or an interfacial phase which has a different density than the film and thus contributes to the XRR data.

   For example, in our samples, we know by XMCD and HAXPES that the sample has an intralayer of γ-Fe_2O_3 of thickness about 2 nm between Fe_3O_4 film and $SrTiO_3$ substrate. However, it is hard to extract this information by XRR. Because the γ-Fe_2O_3 phase has nearly identical density to the Fe_3O_4 phase of 5.49 gm/cm^3. Additionally, the thickness of 2 nm is hardly detected by XRR.

   Still adding this information to the XRR fitting program may help to get a perfect fitting for the experimental data.

A.2 Simulation of XMCD spectra

We determine the element-specific magnetic properties of the $Fe_3O_4/SrTiO_3$ films by XAS and XMCD. XAS spectra of the Fe $L_{2,3}$-edge of the films have been measured. The XAS was measured in total electron yield mode. In order to measure the XAS and XMCD spectra correctly, many measurement steps have to be done. Then, the data should be treated carefully before any calculations.

Experimental setup

1. The X-ray circular polarized beam is incident parallel to the magnetic field direction ($\theta = 0°$).
2. The Fe_3O_4 films have an in-plane magnetic easy axis. The sample should be aligned parallel to the field ($\theta = 0°$). This is difficult to achieve with the X-ray. Therefore, we adjusted the samples in a near-grazing emission geometry with an offset ($\theta = 10°$).
3. The applied magnetic field should be higher than the field needed for the saturation magnetization. The saturation magnetization of Fe_3O_4 films is achieved in the field of 1.2 T. In this study, we used a magnetic field of 1 T for measuring the XMCD to save time and energy.
4. For proper subtraction to the background and the XMCD calculations of the $L_{2,3}$-edge, the photon energy should be in an extended range of 680 eV to 780 eV. Because of the limited time of the experiment, we choose to use the photon energy of range between 690 eV to 740 eV and this is the minimum energy possible for the XMCD calculations and only valid because our films have a strong magnetic signal with respect to the noise. Therefore, it is not recommended for other studies.
5. To check for beam-damage, we measured five polarized absorption spectra (+ + - - +). The additional (+) at the beginning of the sequence is not taken into account and only used to adjust the X-ray beam. Thus, only four polarized absorption spectra (+ - - +) have been used in the calculations.
6. All the films have been cooled down to 10 K in a zero applied magnetic field. After stabilizing the temperature, the field has been applied.
7. The films also have been measured at room temperature to check the effect of the Verwey transition. We did not observe any differences between the room temperature and the low-temperature measurements because the applied field of 1 T is expected to be the saturation magnetization above and below the Verwey transition. For further studies on the Verwey temperature, it is recommended to use a magnetic field of 0.05 T.
8. All the samples have been measured on the same holder in the same environment which ensures an identical sample history.

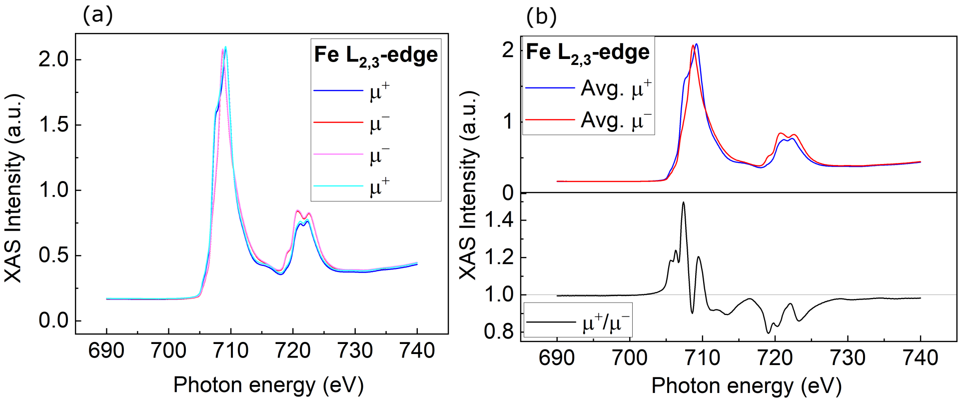

Figure A.3: (a) Four Fe $L_{2,3}$-edge XAS spectra recorded with two different X-ray polarization, a left- μ^+ and right-handed μ^- and (b) Top: two average XAS spectra $(\mu_1^+ + \mu_2^+)/2$ and $(\mu_1^- + \mu_2^-)/2$ and Bottom: the average μ^+ / average μ^-, of 38 nm thick Fe_3O_4 film grown at temperature T_{growth}=400 °C.

Data treatment

Before any calculations, we should ensure the quality of the XAS spectra in terms of background, signal quality, etc.

1. First, to calculate the XAS spectra, we divide the XAS intensities of Fe $L_{2,3}$-edge by the incident X-ray beam intensity I_0. Second, We check that all the four XAS spectra, two measured with positive polarization μ^+ and two with negative polarization μ^-, do not possess any beam damage as shown in Figure A.3 (a).

2. Linear fitting correction has to be done for the pre-edge (photon energy E = 690−700 eV). However, for all our spectra the noise to signal ratio is very small (strong XAS spectra) and the pre-edge is in good linear shape. Therefore, we didn't need this step.

3. We calculate the XAS spectra–Avg/mu^+ and Avg/mu^- (Figure A.3 (b-top))

$$Avg\,\mu^+ = \frac{\mu_1^+ + \mu_2^+}{2} \quad and \quad Avg\,\mu^- = \frac{\mu_1^- + \mu_2^-}{2} \quad . \tag{A.2.1}$$

4. Now, the post edge correction is needed E >730 eV. To do that properly we first calculated μ^+/μ^- as shown in Figure A.3 (b-bottom). Second, linear fitting is done between the pre- and post-edges ($I = a * E + b$, I is XAS intensity and E is photon energy). Third, we correct only one of the polarized spectra for example $Avg\,\mu^+$

$$Avg\,\mu^+_{corrected} = \frac{Avg\,\mu^+}{a * E + b} \quad . \tag{A.2.2}$$

5. We calculate average- XAS.

$$Avg\,XAS\ = \frac{Avg\,\mu^{+}_{corrected} + Avg\,\mu^{-}}{2} \quad . \tag{A.2.3}$$

6. We normalize the XAS spectra that the pre- and post- edges equal to 0 and 1, respectively. We call the normalization factor $Norm\,f$.

7. We calculate the XMCD spectra

$$XMCD\ = \frac{Avg\,\mu^{+}_{corrected} - Avg\,\mu^{-}}{Norm\,f} \quad . \tag{A.2.4}$$

8. We calculate the step function

$$\mu_{step} = \frac{2}{3}\frac{1}{1+e^{E_{L_3}-E}} + \frac{1}{3}\frac{1}{1+e^{E_{L_2}-E}} \quad . \tag{A.2.5}$$

9. Before calculating the integration of the Avg. XAS spectra, we have to subtract the step function $Avg\,XAS - \mu_{step}$.

A.3 Optimization of magnetite's growth parameters: pressure, laser fluence and frequency

The crystallinity and structural properties of the iron oxides films are investigated by X-ray diffraction (XRD). We can distinguish between different iron oxides phases by the structural properties where α-Fe_2O_3 has a corundum structure and both γ-Fe_2O_3 and Fe_3O_4 are spinels. All XRD patterns are normalized to their $SrTiO_3$ (002) reflection.

Background pressure

Figure A.4 illustrates the θ-2θ scans around the $SrTiO_3$ (002) reflection of films grown at different background pressure in comparison with reference spectra to α-Fe_2O_3, γ-Fe_2O_3 and Fe_3O_4. From the reference spectra, it is hard to differentiate between Fe_3O_4 and γ-Fe_2O_3 phases. The films grown at background pressure 10^{-5} mbar to 10^{-3} mbar show structural properties similar to the Fe_3O_4 and γ-Fe_2O_3 phases. However, the films grown at background pressure 10^{-2} mbar and 10^{-1} mbar show structural properties similar to α-Fe_2O_3. The film grown at 10^{-5} mbar shows a single crystalline characteristic. However, all the other films are polycrystalline. We can not differ between Fe_3O_4 and γ-Fe_2O_3 by XRD but it is possible by VSM. We measured MT curves for all the films to identify the Verwey transition. The film grown at 10^{-5} mbar shows a Verwey transition around 110 K indicate the formation of Fe_3O_4 phase. However, all the other films show a vanishing Verwey transition which indicates the formation of the γ-Fe_2O_3 phase.

Laser fluence

Figure A.5 illustrates the θ-2θ scans around the $SrTiO_3$ (002) reflection of films grown at different laser fluence in comparison with reference spectra to α-Fe_2O_3, γ-Fe_2O_3 and Fe_3O_4. Both films grown at laser fluence of 1.5 J/cm^2 and 1 J/cm^2 show structural properties similar to Fe_3O_4 and γ-Fe_2O_3. Both films are single crystalline. However, one grows parallel to (001) and the second grow parallel to (111), respectively. The Verwey transition is around 110 K for film grown at a laser fluence of 1.5 J/cm^2 indicate the formation of Fe_3O_4 phase. However, the film grown at a laser fluence of 1 J/cm^2 shows a vanishing for Verwey transition indicating the formation of the γ-Fe_2O_3 phase.

Frequency

Figure A.6 illustrates the θ-2θ scans around the $SrTiO_3$ (002) reflection of films grown at different frequency in comparison with reference spectra to α-Fe_2O_3, γ-Fe_2O_3 and Fe_3O_4. Both films grown at a frequency of 5 Hz and 2 Hz show structural properties similar to Fe_3O_4 and γ-Fe_2O_3. Both films are single crystalline parallel to (001). However, the films grown at 2 Hz shows a suppression to the Fe_3O_4 (004) peak indicating the inferior crystallinity of the film as well as it showing a vanishing Verwey transition.

Figure A.7 shows the roughness of the films measured by the AFM and XRR. The roughness decreases with decreasing background pressure.

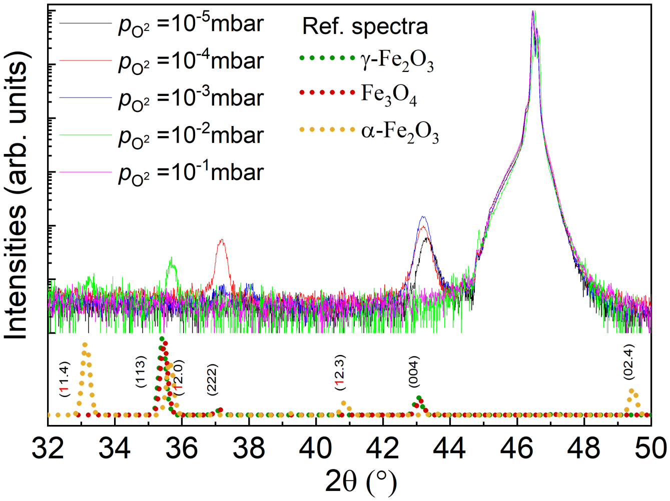

Figure A.4: Out-of-plane X-ray diffraction θ-2θ scans of the iron oxides films grown at different background pressure at constant temperature of 700 °C, frequency of 5 Hz and laser fluence of 1.5 J/cm^2.

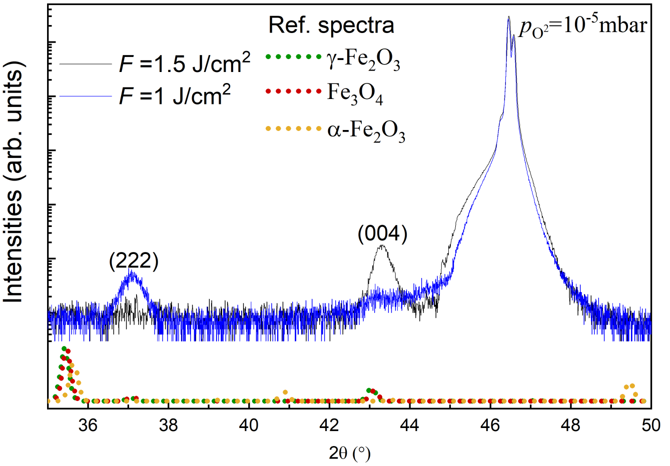

Figure A.5: Out-of-plane X-ray diffraction θ-2θ scans of the iron oxides films grown at different laser fluence at constant temperature of 700 °C, frequency of 5 Hz and background pressure of 2×10^{-5} mbar.

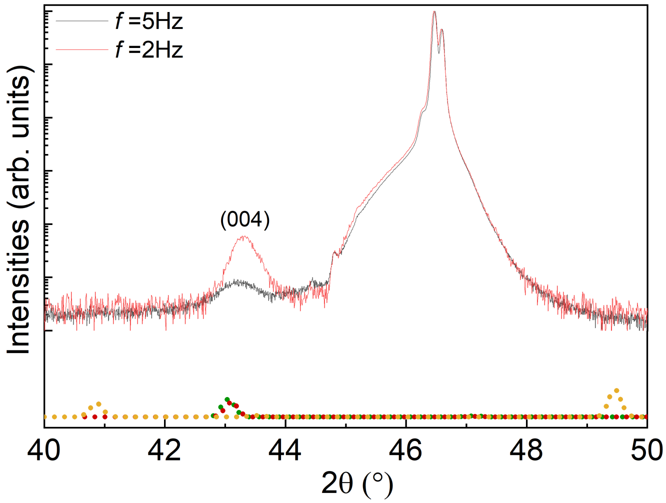

Figure A.6: Out-of-plane X-ray diffraction θ-2θ scans of the iron oxides films grown at different frequency at constant temperature of 700 °C, background pressure of 2×10^{-5} mbar and laser fluence of 1.5 J/cm^2.

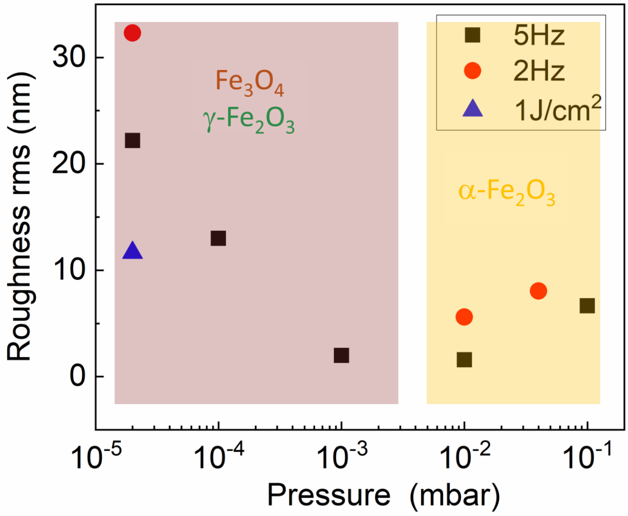

Figure A.7: The calculated roughness of the iron oxides films as a function of the background pressure.

A.4 Nb:SrTiO$_3$ surface preparation

The treatment of the Nb:SrTiO$_3$ surface was taken from [150, 151] and optimized by our colleague Ronja Hinz as follows:

1. 3 minutes in acetone in a supersonic bath adjusted to the lowest level.
2. 3 minutes in isopropanol in a supersonic bath adjusted to the lowest level.
3. Blowing the samples dry with nitrogen.
4. 3 minutes in deionized water in a supersonic bath adjusted to the lowest level.
5. Blowing the samples dry with nitrogen.
6. Etching each the substrate for 60 seconds in buffered hydrofluoric acid.
7. Putting the samples in deionized water to stop the etching process and remove any residual SrO layers and the buffered hydrofluoric acid.
8. 3 minutes in acetone in a supersonic bath adjusted to the lowest level.
9. 3 minutes in isopropanol in a supersonic bath adjusted to the lowest level.
10. Blowing the samples dry with nitrogen.
11. Annealing the samples at 950 °C, at normal atmosphere for 2.5 hours with a temperature ramp of 1.5 hours.

List of Abbreviations

STO	$SrTiO_3$
NSTO	$Nb:SrTiO_3$
YSZ	Yttria-Stabilized Zirconia
PLD	Pulsed Laser Deposition
AFM	Atomic Force Microscopy
XRD	X-ray Diffraction
XRR	X-ray Reflection
VSM	Vibrating Sample Magnetometer
HAXPES	Hard X-ray Photoelectron Spectroscopy
XAS	X-ray Absorption Spectroscopy
XMCD	X-ray Magnetic Circular Dichroism
TEY	Total Electron Yield
FY	Fluorescence Yield
APBs	Anti-Phase Boundaries

Bibliography

[1] M. N. Baibich, J. M. Broto, A. Fert, F. N. Van Dau, F. Petroff, P. Etienne, G. Creuzet, A. Friederich, and J. Chazelas, "Giant magnetoresistance of (001)Fe/(001)Cr magnetic superlattices", Phys. Rev. Lett. **61**, 2472 (1988) (cited on page 1).

[2] G. Binasch, P. Grünberg, F. Saurenbach, and W. Zinn, "Enhanced magnetoresistance in layered magnetic structures with antiferromagnetic interlayer exchange", Phys. Rev. B **39**, 4828 (1989) (cited on page 1).

[3] W. E. Pickett and D. J. Singh, "Electronic structure and half-metallic transport in the $La_{1-x}Ca_xMnO_3$ system", Phys. Rev. B **53**, 1146 (1996) (cited on page 1).

[4] V. Ferrari, J. M. Pruneda, and E. Artacho, "Density functionals and half-metallicity in $La_{2/3}Sr_{1/3}MnO_3$", physica status solidi (a) **203**, 1437 (2006) (cited on page 1).

[5] M. Bowen, M. Bibes, A. Barthélémy, J.-P. Contour, A. Anane, Y. Lemaıtre, and A. Fert, "Nearly total spin polarization in $La_{2/3}Sr_{1/3}MnO_3$ from tunneling experiments", Applied Physics Letters **82**, 233 (2003) (cited on page 1).

[6] M. Fonin, Y. S. Dedkov, J. Mayer, U. Rüdiger, and G. Güntherodt, "Preparation, structure, and electronic properties of Fe_3O_4 films on the Fe(110)/Mo(110)/Al_2O_3 (112", Phys. Rev. B **68**, 045414 (2003) (cited on page 1).

[7] Y. S. Dedkov, U. Rüdiger, and G. Güntherodt, "Evidence for the half-metallic ferromagnetic state of Fe_3O_4 by spin-resolved photoelectron spectroscopy", Phys. Rev. B **65**, 064417 (2002) (cited on page 1).

[8] V. N. Antonov, B. N. Harmon, and A. N. Yaresko, "Electronic structure and X-ray magnetic circular dichroism in Fe_3O_4 and Mn-, Co−, or Ni-substituted Fe_3O_4", Phys. Rev. B **67**, 024417 (2003) (cited on page 1).

[9] Z. Zhang and S. Satpathy, "Electron states, magnetism, and the Verwey transition in magnetite", Phys. Rev. B **44**, 13319 (1991) (cited on page 1).

[10] P. Seneor, A. Fert, J.-L. Maurice, F. Montaigne, F. Petroff, and A. Vaurès, "Large magnetoresistance in tunnel junctions with an iron oxide electrode", Applied Physics Letters **74**, 4017 (1999) (cited on page 1).

[11] K.-i. Aoshima and S. X. Wang, “Fe_3O_4 and its magnetic tunneling junctions grown by ion beam deposition”, Journal of Applied Physics **93**, 7954 (2003) (cited on page 1).

[12] A. Bataille, R. Mattana, P. Seneor, A. Tagliaferri, S. Gota, K. Bouzehouane, C. Deranlot, M.-J. Guittet, J.-B. Moussy, C. de Nadaı¨, N. Brookes, F. Petroff, and M. Gautier-Soyer, “On the spin polarization at the Fe_3O_4/γ-Al_2O_3 interface probed by spin-resolved photoemission and spin-dependent tunneling”, Journal of Magnetism and Magnetic Materials **316**, Proceedings of the Joint European Magnetic Symposia, e963 (2007) (cited on page 1).

[13] S. Parkin, Xin Jiang, C. Kaiser, A. Panchula, K. Roche, and M. Samant, “Magnetically engineered spintronic sensors and memory”, Proceedings of the IEEE **91**, 661 (2003) (cited on page 2).

[14] Z.-M. Liao, Y.-D. Li, J. Xu, J.-M. Zhang, K. Xia, and D.-P. Yu, “Spin-filter effect in magnetite nanowire”, Nano Letters **6**, 1087 (2006) (cited on page 2).

[15] E. Wada, K. Watanabe, Y. Shirahata, M. Itoh, M. Yamaguchi, and T. Taniyama, “Efficient spin injection into gaas quantum well across Fe_3O_4 spin filter”, Applied Physics Letters **96**, 102510 (2010) (cited on page 2).

[16] H.-C. Wu, O. N. Mryasov, M. Abid, K. Radican, and I. V. Shvets, “Magnetization states of all-oxide spin valves controlled by charge-orbital ordering of coupled ferromagnets.”, Scientific Reports **3**, 1830 (2013) (cited on page 2).

[17] T. Kado, “Large room-temperature inverse magnetoresistance in tunnel junctions with a Fe_3O_4 electrode”, Applied Physics Letters **92**, 092502 (2008) (cited on page 2).

[18] R. Ramos, T. Kikkawa, K. Uchida, H. Adachi, I. Lucas, M. H. Aguirre, P. Algarabel, L. Morellón, S. Maekawa, E. Saitoh, and M. R. Ibarra, “Observation of the spin Seebeck effect in epitaxial Fe_3O_4 thin films”, Applied Physics Letters **102**, 072413 (2013) (cited on page 2).

[19] M. Hopkin, “Homing pigeons reveal true magnetism”, Nature, 1476 (2004) (cited on page 2).

[20] R. B. Frankel, R. P. Blakemore, and R. S. Wolfe, “Magnetite in freshwater magnetotactic bacteria”, Science **203**, 1355 (1979) (cited on page 2).

[21] J. L. Kirschvink, A. Kobayashi-Kirschvink, and B. J. Woodford, “Magnetite biomineralization in the human brain.”, Proceedings of the National Academy of Sciences **89**, 7683 (1992) (cited on page 2).

[22] A. Ohtomo and H. Y. Hwang, “A high-mobility electron gas at the $LaAlO_3/SrTiO_3$ heterointerface”, Nature **427**, 423 (2004) (cited on page 2).

[23] S. Thiel, G. Hammerl, A. Schmehl, C. W. Schneider, and J. Mannhart, “Tunable quasi-two-dimensional electron gases in oxide heterostructures”, Science **313**, 1942 (2006) (cited on page 2).

[24] A. Brinkman, M. Huijben, M. van Zalk, J. Huijben, U. Zeitler, J. C. Maan, W. G. van der Wiel, G. Rijnders, D. H. A. Blank, and H. Hilgenkamp, “Magnetic effects at the interface between non-magnetic oxides”, Nature Materials **6**, 493 (2007) (cited on page 2).

[25] V. N. Antonov, B. N. Harmon, V. P. Antropov, A. Y. Perlov, and A. N. Yaresko, “Electronic structure and magneto-optical Kerr effect of Fe_3O_4 and Mg^{2+}- or Al^{3+}-substituted Fe_3O_4”, Phys. Rev. B **64**, 134410 (2001) (cited on page 6).

[26] M. E. Fleet, “The structure of magnetite”, Acta Crystallographica Section B **37**, 917 (1981) (cited on page 6).

[27] J. B. Goodenough, “Theory of the role of covalence in the perovskite-type manganites [La, M(II)]MnO_3”, Phys. Rev. **100**, 564 (1955) (cited on page 7).

[28] J. Kanamori, “Superexchange interaction and symmetry properties of electron orbitals”, Journal of Physics and Chemistry of Solids **10**, 87 (1959) (cited on page 7).

[29] P. W. Anderson, “Antiferromagnetism. theory of superexchange interaction”, Phys. Rev. **79**, 350 (1950) (cited on page 7).

[30] S. Blundell, *Magnetism in condensed matter*, Oxford Master Series in Condensed Matter Physics 4 (OUP Oxford, 2001) (cited on page 8).

[31] J.-B. Moussy, “From epitaxial growth of ferrite thin films to spin-polarized tunnelling”, Journal of Physics D: Applied Physics **46**, 143001 (2013) (cited on page 8).

[32] J. Stöhr and H. C. Siegmann, *Magnetism: from fundamentals to nanoscale dynamics*, Springer Series in Solid-State Sciences (Springer, 2006) (cited on pages 8, 28, 29).

[33] E. J. W. VERWEY, “Electronic conduction of magnetite (Fe_3O_4) and its transition point at low temperatures”, Nature **144**, 327 (1939) (cited on pages 8, 45).

[34] M. S. Senn, J. P. Wright, and J. P. Attfield, “Charge order and three-site distortions in the Verwey structure of magnetite”, Nature **481**, 1476 (2012) (cited on page 8).

[35] M. Iizumi, T. F. Koetzle, G. Shirane, S. Chikazumi, M. Matsui, and S. Todo, “Structure of magnetite (Fe_3O_4) below the Verwey transition temperature”, Acta Crystallographica Section B **38**, 2121 (1982) (cited on page 8).

[36] L. R. Bickford, “The low temperature transformation in ferrites”, Rev. Mod. Phys. **25**, 75 (1953) (cited on pages 8, 49).

[37] A. Yamamoto, “Modulated structure of wustite (Fe_1-xO) (three-dimensional modulation)”, Acta Crystallographica Section B **38**, 1451 (1982) (cited on page 8).

[38] F. Koch and J. B. Cohen, “The defect structure of $Fe_{1-x}O$”, Acta Crystallographica Section B **25**, 275 (1969) (cited on page 9).

[39] E. Gartstein, J. Cohen, and T. Mason, “Defect agglomeration in wüstite at high temperatures—II.: an electrical conduction model”, Journal of Physics and Chemistry of Solids **47**, 775 (1986) (cited on page 9).

[40] J.-E. Jørgensen, L. Mosegaard, L. E. Thomsen, T. R. Jensen, and J. C. Hanson, “Formation of γ-Fe_2O_3 nanoparticles and vacancy ordering: an in situ X-ray powder diffraction study”, Journal of Solid State Chemistry **180**, 180 (2007) (cited on page 9).

[41] E. N. Maslen, V. A. Streltsov, N. R. Streltsova, and N. Ishizawa, “Synchrotron X-ray study of the electron density in α-Fe_2O_3”, Acta Crystallographica Section B **50**, 435 (1994) (cited on page 9).

[42] R. J. Nelmes, G. M. Meyer, and J. Hutton, “Thermal motion in $SrTiO_3$ at room temperature: anharmonic or disordered?”, Ferroelectrics **21**, 461 (1978) (cited on page 10).

[43] K. van Benthem, C. Elsässer, and R. H. French, “Bulk electronic structure of $SrTiO_3$: experiment and theory”, Journal of Applied Physics **90**, 6156 (2001) (cited on page 10).

[44] H. Horiuchi, A. J. Schultz, P. C. W. Leung, and J. M. Williams, “Time-of-flight neutron diffraction study of a single crystal of yttria-stabilized zirconia, $Zr(Y)O_{1.862}$, at high temperature and in an applied electrical field”, Acta Crystallographica Section B **40**, 367 (1984) (cited on page 11).

[45] J. G. Zheng, G. E. Sterbinsky, J. Cheng, and B. W. Wessels, “Epitaxial Fe_3O_4 on $SrTiO_3$ characterized by transmission electron microscopy”, Journal of Vacuum Science & Technology B: Microelectronics and Nanometer Structures Processing, Measurement, and Phenomena **25**, 1520 (2007) (cited on pages 11, 31).

[46] S. Celotto, W. Eerenstein, and T. Hibma, “Characterization of anti-phase boundaries in epitaxial magnetite films”, The European Physical Journal B - Condensed Matter and Complex Systems **36**, 271 (2003) (cited on page 12).

[47] K. P. McKenna, F. Hofer, D. Gilks, V. K. Lazarov, C. Chen, Z. Wang, and Y. Ikuhara, “Atomic-scale structure and properties of highly stable antiphase boundary defects in Fe_3O_4”, Nature Communications **5**, 5740 (2014) (cited on pages 12, 46).

[48] M. W. Chase, *NIST-JANAF thermochemical tables*, 4th edition, Journal of physical and chemical reference data., Monograph ; no.9 (American Institute of Physics for the National Institute of Standards and Technology, U.S. Department of Commerce: Gaithersburg, MD, 1998) (cited on pages 12, 13, 75, 109).

[49] V. E. Alexandrov, E. A. Kotomin, J. Maier, and R. A. Evarestov, “First-principles study of bulk and surface oxygen vacancies in $SrTiO_3$ crystal”, The European Physical Journal B **72**, 53 (2009) (cited on pages 13, 75).

[50] M. Asadikiya, H. Sabarou, M. Chen, and Y. Zhong, “Phase diagram for a nano-yttria-stabilized zirconia system”, RSC Adv. **6**, 17438 (2016) (cited on page 13).

[51] M. Yazdi-Rizi, P. Marsik, B. P. P. Mallett, K. Sen, A. Cerreta, A. Dubroka, M. Scigaj, F. Sánchez, G. Herranz, and C. Bernhard, "Infrared ellipsometry study of photogenerated charge carriers at the (001) and (110) surfaces of $SrTiO_3$ crystals and at the interface of the corresponding $LaAlO_3/SrTiO_3$ heterostructures", Phys. Rev. B **95**, 195107 (2017) (cited on page 13).

[52] D. B. Chrisey and G. K. Hubler, *Pulsed laser deposition of thin films* (Wiley, New York, 1994) (cited on page 15).

[53] D. Nečas and P. Klapetek, "Gwyddion: an open-source software for SPM data analysis", Open Physics **10**, 181 (2011) (cited on pages 17, 34).

[54] H. Kiessig, "Interferenz von Röntgenstrahlen an dünnen Schichten", Annalen der Physik **402**, 769 (1931) (cited on page 18).

[55] L. G. Parratt, "Surface studies of solids by total reflection of X-rays", Phys. Rev. **95**, 359 (1954) (cited on page 18).

[56] S. Hüfner, *Photoelectron spectroscopy: principles and applications*, Springer Series in Solid-State Sciences (Springer Berlin Heidelberg, 2013) (cited on page 21).

[57] F. De Groot and A. Kotani, *Core level spectroscopy of solids*, Advances in Condensed Matter Science (Taylor & Francis Group, 2008) (cited on page 21).

[58] C. N. Berglund and W. E. Spicer, "Photoemission studies of copper and silver: experiment", Phys. Rev. **136**, A1044 (1964) (cited on page 21).

[59] S. Tanuma, C. J. Powell, and D. R. Penn, "Calculations of electron inelastic mean free paths. IX. data for 41 elemental solids over the 50 eV to 30 keV range", Surface and Interface Analysis **43**, 689 (2011) (cited on page 23).

[60] J. A. Colón Santana, *Quantitative core level photoelectron spectroscopy*, 2053-2571 (Morgan Claypool Publishers, 2015) (cited on page 23).

[61] T. Fujii, F. M. F. de Groot, G. A. Sawatzky, F. C. Voogt, T. Hibma, and K. Okada, "In situ XPS analysis of various iron oxide films grown by NO_2-assisted molecular-beam epitaxy", Phys. Rev. B **59**, 3195 (1999) (cited on pages 24–26, 39, 40, 65, 66, 93).

[62] S. Gota, E. Guiot, M. Henriot, and M. Gautier-Soyer, "Atomic-oxygen-assisted MBE growth of $\alpha-\mathrm{fe}_2\mathrm{o}_3$ on $\alpha-\mathrm{al}_2\mathrm{o}_3$(0001): metastable FeO(111)-like phase at subnanometer thicknesses", Phys. Rev. B **60**, 14387 (1999) (cited on pages 24, 25, 39, 40, 65, 66, 93).

[63] R. P. Gupta and S. K. Sen, "Calculation of multiplet structure of core p-vacancy levels", Phys. Rev. B **10**, 71 (1974) (cited on pages 25, 26).

[64] R. P. Gupta and S. K. Sen, "Calculation of multiplet structure of core p -vacancy levels. II", Phys. Rev. B **12**, 15 (1975) (cited on pages 25, 26).

[65] M. A. Brisk and A. Baker, "Shake-up satellites in X-ray photoelectron spectroscopy", Journal of Electron Spectroscopy and Related Phenomena **7**, 197 (1975) (cited on page 26).

[66] S.-J. Oh, “Origin of 2p core-level XPS satellites in the late 3d transition metal dihalides”, in Core-level spectroscopy in condensed systems, edited by J. Kanamori and A. Kotani (1988), pages 125–135 (cited on page 26).

[67] J. Strempfer, S. Francoual, D. Reuther, D. K. Shukla, A. Skaugen, H. Schulte-Schrepping, T. Kracht, and H. Franz, “Resonant scattering and diffraction beamline P09 at PETRA III”, Journal of Synchrotron Radiation **20**, 541 (2013) (cited on page 26).

[68] A. Gloskovskii, G. Stryganyuk, G. H. Fecher, C. Felser, S. Thiess, H. Schulz-Ritter, W. Drube, G. Berner, M. Sing, R. Claessen, and M. Yamamoto, “Magnetometry of buried layers—linear magnetic dichroism and spin detection in angular resolved hard X-ray photoelectron spectroscopy”, Journal of Electron Spectroscopy and Related Phenomena **185**, 47 (2012) (cited on page 26).

[69] M. Gorgoi, S. Svensson, F. Schäfers, G. Öhrwall, M. Mertin, P. Bressler, O. Karis, H. Siegbahn, A. Sandell, H. Rensmo, W. Doherty, C. Jung, W. Braun, and W. Eberhardt, “The high kinetic energy photoelectron spectroscopy facility at BESSY progress and first results”, Nuclear Instruments and Methods in Physics Research Section A: Accelerators, Spectrometers, Detectors and Associated Equipment **601**, Special issue in honour of Prof. Kai Siegbahn, 48 (2009) (cited on page 26).

[70] F. Schaefers, M. Mertin, and M. Gorgoi, “KMC-1: a high resolution and high flux soft X-ray beamline at BESSY”, Review of Scientific Instruments **78**, 123102 (2007) (cited on page 26).

[71] P. Carra, B. T. Thole, M. Altarelli, and X. Wang, “X-ray circular dichroism and local magnetic fields”, Phys. Rev. Lett. **70**, 694 (1993) (cited on pages 28, 42).

[72] C. T. Chen, Y. U. Idzerda, H.-J. Lin, N. V. Smith, G. Meigs, E. Chaban, G. H. Ho, E. Pellegrin, and F. Sette, “Experimental confirmation of the X-ray magnetic circular dichroism sum rules for iron and cobalt”, Phys. Rev. Lett. **75**, 152 (1995) (cited on pages 28, 42).

[73] D. J. Huang, C. F. Chang, H.-T. Jeng, G. Y. Guo, H.-J. Lin, W. B. Wu, H. C. Ku, A. Fujimori, Y. Takahashi, and C. T. Chen, “Spin and orbital magnetic moments of Fe_3O_4”, Phys. Rev. Lett. **93**, 077204 (2004) (cited on page 30).

[74] J. Stöhr and H. König, “Determination of spin- and orbital-moment anisotropies in transition metals by angle-dependent X-ray magnetic circular dichroism”, Phys. Rev. Lett. **75**, 3748 (1995) (cited on page 30).

[75] E. Stavitski and F. M. de Groot, “The CTM4XAS program for EELS and XAS spectral shape analysis of transition metal L edges”, Micron **41**, 687 (2010) (cited on pages 30, 72).

[76] *High Field Magnet, I10 beamline, Diamond Light Source*, `https://www.diamond.ac.uk/Instruments/Magnetic-Materials/I10/magnet.html`, Accessed: 21-12-2019 (cited on page 30).

[77] X. Guan, G. Zhou, W. Xue, Z. Quan, and X. Xu, "The investigation of giant magnetic moment in ultrathin Fe_3O_4 films", APL Materials **4**, 036104 (2016) (cited on pages 31, 32).

[78] H. Ji, Y. G. Wang, and Y. Li, "Charge screening-controlled Verwey phase transition in Fe_3O_4/$SrTiO_3$ heterostructure", Journal of Physics: Condensed Matter **30**, 11LT01 (2018) (cited on pages 31, 32).

[79] O. Kuschel, W. Spiess, T. Schemme, J. Rubio-Zuazo, K. Kuepper, and J. Wollschläger, "Real-time monitoring of the structure of ultrathin Fe_3O_4 films during growth on Nb-doped $SrTiO_3$(001)", Applied Physics Letters **111**, 041902 (2017) (cited on pages 31, 59, 67, 80, 81).

[80] A. Hamie, Y. Dumont, E. Popova, A. Fouchet, B. Warot-Fonrose, C. Gatel, E. Chikoidze, J. Scola, B. Berini, and N. Keller, "Investigation of high quality magnetite thin films grown on $SrTiO_3$(001) substrates by pulsed laser deposition", Thin Solid Films **525**, 115 (2012) (cited on pages 31, 49).

[81] Q.-X. Zhu, M. Zheng, M.-M. Yang, R.-K. Zheng, Y. Wang, X.-M. Li, and X. Shi, "Interface correlated exchange bias effect in epitaxial Fe_3O_4 thin films grown on $SrTiO_3$ substrates", Applied Physics Letters **105**, 241604 (2014) (cited on pages 31, 59, 62, 67, 80).

[82] G. Leung, M. Vickers, R. Yu, and M. Blamire, "Epitaxial growth of Fe_3O_4 (111) on $SrTiO_3$ (001) substrates", Journal of Crystal Growth **310**, 5282 (2008) (cited on page 31).

[83] R. Takahashi, H. Misumi, and M. Lippmaa, "Growth temperature effect on the structural and magnetic properties of Fe_3O_4 films grown by the self-template method", Journal of Applied Physics **116**, 033918 (2014) (cited on page 31).

[84] M. Hoppe, M. Gorgoi, C. M. Schneider, and M. Müller, "Wide-range structural and chemical stability of the magnetic oxide $NiFe_2O_4$ grown by O_2-assisted pulsed laser deposition", IEEE Transactions on Magnetics **50**, 1 (2014) (cited on page 31).

[85] G. Koster, B. L. Kropman, G. J. H. M. Rijnders, D. H. A. Blank, and H. Rogalla, "Quasi-ideal strontium titanate crystal surfaces through formation of strontium hydroxide", Applied Physics Letters **73**, 2920 (1998) (cited on page 32).

[86] J. X. Ma, D. Mazumdar, G. Kim, H. Sato, N. Z. Bao, and A. Gupta, "A robust approach for the growth of epitaxial spinel ferrite films", Journal of Applied Physics **108**, 063917 (2010) (cited on page 34).

[87] J. A. Moyer, R. Gao, P. Schiffer, and L. W. Martin, "Epitaxial growth of highly-crystalline spinel ferrite thin films on perovskite substrates for all-oxide devices", Scientific Reports **5**, 10363 (2015) (cited on page 34).

[88] S. Kale, S. M. Bhagat, S. E. Lofland, T. Scabarozi, S. B. Ogale, A. Orozco, S. R. Shinde, T. Venkatesan, B. Hannoyer, B. Mercey, and W. Prellier, "Film thickness and temperature dependence of the magnetic properties of pulsed-laser-deposited Fe_3O_4 films on different substrates", Phys. Rev. B **64**, 205413 (2001) (cited on page 38).

[89] C. Kim, I. K. Robinson, J. Myoung, K. Shim, M.-C. Yoo, and K. Kim, "Critical thickness of GaN thin films on sapphire (0001)", Applied Physics Letters **69**, 2358 (1996) (cited on page 38).

[90] H. Elnaggar, R. Wang, M. Ghiasi, M. Yañez, M. U. Delgado-Jaime, M. H. Hamed, A. Juhin, S. S. Dhesi, and F. de Groot, "Probing the local distortion of Fe sites in Fe_3O_4 thin films using enhanced symmetry selection in XMLD", Phys. Rev. Materials **4**, 024415 (2020) (cited on page 38).

[91] D. H. Kim, H. J. Lee, G. Kim, Y. S. Koo, J. H. Jung, H. J. Shin, J.-Y. Kim, and J.-S. Kang, "Interface electronic structures of $BaTiO_3$@X nanoparticles (X = γ-Fe_2O_3, Fe_3O_4, α-Fe_2O_3, and Fe) investigated by XAS and XMCD", Phys. Rev. B **79**, 033402 (2009) (cited on pages 40, 67).

[92] E. Pellegrain, M. Hagelstein, S. Doyle, H. O. Moser, J. Fuchs, D. Vollath, S. Schuppler, M. A. James, S. S. Saxena, L. Niesen, O. Rogojanu, G. A. Sawatzky, C. Ferrero, M. Borowski, O. Tjernberg, and N. B. Brookes, "Characterization of nanocrystalline γ-Fe_2O_3 with synchrotron radiation techniques", physica status solidi (b) **215**, 797 (1999) (cited on pages 42, 70).

[93] F. Schedin, E. W. Hill, G. van der Laan, and G. Thornton, "Magnetic properties of stoichiometric and nonstoichiometric ultrathin Fe_3O_4(111) films on Al_2O_3(0001)", Journal of Applied Physics **96**, 1165 (2004) (cited on pages 42, 70, 73).

[94] E. Goering, S. Gold, M. Lafkioti, and G. Schütz, "Vanishing Fe 3d orbital moments in single-crystalline magnetite", Europhysics Letters (EPL) **73**, 97 (2006) (cited on page 42).

[95] C. Piamonteze, P. Miedema, and F. M. F. de Groot, "Accuracy of the spin sum rule in XMCD for the transition-metal L edges from manganese to copper", Phys. Rev. B **80**, 184410 (2009) (cited on page 45).

[96] C. Schmitz-Antoniak, D. Schmitz, A. Warland, M. Darbandi, S. Haldar, S. Bhandary, B. Sanyal, O. Eriksson, and H. Wende, "Suppression of the Verwey transition by charge trapping", Annalen der Physik **530**, 1700363 (2018) (cited on page 45).

[97] W. Q. Liu, Y. B. Xu, P. K. J. Wong, N. J. Maltby, S. P. Li, X. F. Wang, J. Du, B. You, J. Wu, P. Bencok, and R. Zhang, "Spin and orbital moments of nanoscale Fe_3O_4 epitaxial thin film on MgO/GaAs(100)", Applied Physics Letters **104**, 142407 (2014) (cited on page 45).

[98] Weiss, Pierre and Forrer, R., "La saturation absolue des ferromagnétiques et les lois d'approche en fonction du champ et de la température", Ann. Phys. **10**, 279 (1929) (cited on pages 45, 46, 84).

[99] W. Eerenstein, T. T. M. Palstra, S. S. Saxena, and T. Hibma, "Spin-polarized transport across sharp antiferromagnetic boundaries", Phys. Rev. Lett. **88**, 247204 (2002) (cited on page 46).

[100] D. T. Margulies, F. T. Parker, F. E. Spada, R. S. Goldman, J. Li, R. Sinclair, and A. E. Berkowitz, "Anomalous moment and anisotropy behavior in Fe_3 O_4 films", Phys. Rev. B **53**, 9175 (1996) (cited on pages 46, 50).

[101] Ö. Özdemir, "Coercive force of single crystals of magnetite at low temperatures", Geophysical Journal International **141**, 351 (2000) (cited on page 46).

[102] S. Arajs, N. Amin, and E. E. Anderson, "Magnetic coercivity of Fe_3O_4 particle systems", Journal of Applied Physics **69**, 5122 (1991) (cited on page 46).

[103] Ö. Özdemir, D. J. Dunlop, and B. M. Moskowitz, "Changes in remanence, coercivity and domain state at low temperature in magnetite", Earth and Planetary Science Letters **194**, 343 (2002) (cited on page 46).

[104] R. M. Cornell and U. Schwertmann, *The iron oxides structure, properties, reactions, occurrences, and uses*, 2nd, completely rev. and extended ed, Includes bibliographical references (p. 553-646) and index (Weinheim Wiley-VCH, 2003) (cited on page 46).

[105] A. R. Muxworthy and E. McClelland, "Review of the low-temperature magnetic properties of magnetite from a rock magnetic perspective", Geophysical Journal International **140**, 101 (2000) (cited on page 46).

[106] K. Abe, Y. Miyamoto, and S. Chikazumi, "Magnetocrystalline anisotropy of low temperature phase of magnetite", Journal of the Physical Society of Japan **41**, 1894 (1976) (cited on pages 46, 48).

[107] J. [la Figuera], L. Vergara, A. T. N'Diaye, A. Quesada, and A. K. Schmid, "Micromagnetism in (001) magnetite by spin-polarized low-energy electron microscopy", Ultramicroscopy **130**, Eighth International Workshop on LEEM/PEEM, 77 (2013) (cited on page 46).

[108] A. Muxworthy, "Low-temperature susceptibility and hysteresis of magnetite", Earth and Planetary Science Letters **169**, 51 (1999) (cited on pages 46, 48).

[109] F. Walz, "The Verwey transition - a topical review", Journal of Physics: Condensed Matter **14**, R285 (2002) (cited on page 49).

[110] R. Aragón, D. J. Buttrey, J. P. Shepherd, and J. M. Honig, "Influence of nonstoichiometry on the Verwey transition", Phys. Rev. B **31**, 430 (1985) (cited on page 49).

[111] X. H. Liu, A. D. Rata, C. F. Chang, A. C. Komarek, and L. H. Tjeng, "Verwey transition in Fe_3O_4 thin films: influence of oxygen stoichiometry and substrate-induced microstructure", Phys. Rev. B **90**, 125142 (2014) (cited on pages 49, 50, 62, 65).

[112] S. Alraddadi, W. Hines, T. Yilmaz, G. D. Gu, and B. Sinkovic, "Structural phase diagram for ultra-thin epitaxial Fe_3O_4 / MgO(0 0 1) films: thickness and oxygen pressure dependence", Journal of Physics: Condensed Matter **28**, 115402 (2016) (cited on pages 49, 62).

[113] J. A. Moyer, S. Lee, P. Schiffer, and L. W. Martin, "Magnetically disordered phase in epitaxial iron-deficient Fe_3O_4 thin films", Phys. Rev. B **91**, 064413 (2015) (cited on page 49).

[114] M. B. Yazdi, M. Major, A. Wildes, F. Wilhelm, A. Rogalev, W. Donner, and L. Alff, “Possible evidence for a spin-state crossover in the Verwey state in Fe_3O_4 thin films”, Phys. Rev. B **93**, 014439 (2016) (cited on page 49).

[115] J. Dho, B.-g. Kim, and S. Ki, “Distinctive uniaxial magnetic anisotropy and positive magnetoresistance in (110)-oriented Fe_3O_4 films”, Journal of Applied Physics **117**, 163904 (2015) (cited on pages 49, 62).

[116] J. Orna, P. A. Algarabel, L. Morellón, J. A. Pardo, J. M. de Teresa, R. López Antón, F. Bartolomé, L. M. Garcıa, J. Bartolomé, J. C. Cezar, and A. Wildes, “Origin of the giant magnetic moment in epitaxial Fe_3O_4 thin films”, Phys. Rev. B **81**, 144420 (2010) (cited on pages 49, 62).

[117] C. F. Chang, Z. Hu, S. Klein, X. H. Liu, R. Sutarto, A. Tanaka, J. C. Cezar, N. B. Brookes, H.-J. Lin, H. H. Hsieh, C. T. Chen, A. D. Rata, and L. H. Tjeng, “Dynamic atomic reconstruction: how Fe_3O_4 thin films evade polar catastrophe for epitaxy”, Phys. Rev. X **6**, 041011 (2016) (cited on pages 49, 62).

[118] A. K. H. Lee, P. B. Jayathilaka, C. A. Bauer, M. C. Monti, J. T. Markert, A. de Lozanne, and C. W. Miller, “Magnetic force microscopy of epitaxial magnetite films through the Verwey transition”, Applied Physics Letters **97**, 162502 (2010) (cited on page 50).

[119] X. Liu, C.-F. Chang, A. D. Rata, A. C. Komarek, and L. H. Tjeng, “Fe_3O_4 thin films: controlling and manipulating an elusive quantum material”, npj Quantum Materials **1**, 16027 (2016) (cited on page 50).

[120] W. C. Zheng, D. X. Zheng, Y. C. Wang, C. Jin, and H. L. Bai, “Uniaxial strain tuning of the Verwey transition in flexible Fe_3O_4/muscovite epitaxial heterostructures”, Applied Physics Letters **113**, 142403 (2018) (cited on page 50).

[121] P.-C. Wu, P.-F. Chen, T. H. Do, Y.-H. Hsieh, C.-H. Ma, T. D. Ha, K.-H. Wu, Y.-J. Wang, H.-B. Li, Y.-C. Chen, J.-Y. Juang, P. Yu, L. M. Eng, C.-F. Chang, P.-W. Chiu, L. H. Tjeng, and Y.-H. Chu, “Heteroepitaxy of Fe_3O_4/Muscovite: a new perspective for flexible spintronics”, ACS Applied Materials & Interfaces **8**, 33794 (2016) (cited on page 50).

[122] M. Monti, M. Sanz, M. Oujja, E. Rebollar, M. Castillejo, F. J. Pedrosa, A. Bollero, J. Camarero, J. L. F. Cuñado, N. M. Nemes, F. J. Mompean, M. Garcia-Hernández, S. Nie, K. F. McCarty, A. T. N’Diaye, G. Chen, A. K. Schmid, J. F. Marco, and J. de la Figuera, “Room temperature in-plane $\langle 100 \rangle$ magnetic easy axis for $Fe_3O_4/SrTiO_3(001)$:Nb grown by infrared pulsed laser deposition”, Journal of Applied Physics **114**, 223902 (2013) (cited on pages 51, 53, 56, 57).

[123] J. L. F. Cuñado, J. Camarero, F. J. Pedrosa, N. M. Nemes, M. Sanz, M. Oujja, E. Rebollar, J. F. Marco, J. de la Figuera, M. Monti, M. Castillejo, T. Feher, B. Nafradi, L. Forró, and A. Bollero, “Evidence of anomalous switching of the in-plane magnetic easy axis with temperature in Fe_3O_4 film on $SrTiO_3$:Nb by v-MOKE and ferromagnetic resonance”, Nanoscale **11**, 19870 (2019) (cited on pages 51, 53).

[124] M. H. Hamed, R. A. Hinz, P. Lömker, M. Wilhelm, A. Gloskovskii, P. Bencok, C. Schmitz-Antoniak, H. Elnaggar, C. M. Schneider, and M. Müller, "Tunable magnetic phases at $Fe_3O_4/SrTiO_3$ oxide interfaces", ACS Applied Materials & Interfaces **11**, 7576 (2019) (cited on page 59).

[125] M. Hoppe, S. Döring, M. Gorgoi, S. Cramm, and M. Müller, "Enhanced ferrimagnetism in auxetic $NiFe_2O_4$ in the crossover to the ultrathin-film limit", Phys. Rev. B **91**, 054418 (2015) (cited on page 61).

[126] M. Foerster, M. Iliev, N. Dix, X. Martí, M. Barchuk, F. Sánchez, and J. Fontcuberta, "The poisson ratio in $CoFe_2O_4$ spinel thin films", Advanced Functional Materials **22**, 4344 (2012) (cited on page 61).

[127] X. W. Li, A. Gupta, G. Xiao, and G. Q. Gong, "Transport and magnetic properties of epitaxial and polycrystalline magnetite thin films", Journal of Applied Physics **83**, 7049 (1998) (cited on page 65).

[128] R. A. Pattrick, G. Van Der Laan, C. M. B. Henderson, P. Kuiper, E. Dudzik, and D. J. Vaughan, "Cation site occupancy in spinel ferrites studied by X-ray magnetic circular dichroism: developing a method for mineralogists", European Journal of Mineralogy **14**, 1095 (2002) (cited on page 72).

[129] E. Arenholz, G. van der Laan, R. V. Chopdekar, and Y. Suzuki, "Anisotropic X-ray magnetic linear dichroism at the Fe $L_{2,3}$ edges in Fe_3O_4", Phys. Rev. B **74**, 094407 (2006) (cited on page 72).

[130] G. van der Laan and E. Arenholz, "Anisotropic X-ray magnetic linear dichroism", The European Physical Journal Special Topics **169**, 187 (2009) (cited on page 72).

[131] D. Gryaznov, E. Blokhin, A. Sorokine, E. A. Kotomin, R. A. Evarestov, A. Bussmann-Holder, and J. Maier, "A comparative ab initio thermodynamic study of oxygen vacancies in ZnO and $SrTiO_3$: emphasis on phonon contribution", The Journal of Physical Chemistry C **117**, 13776 (2013) (cited on page 75).

[132] C. Mitra, C. Lin, J. Robertson, and A. A. Demkov, "Electronic structure of oxygen vacancies in $SrTiO_3$ and $LaAlO_3$", Phys. Rev. B **86**, 155105 (2012) (cited on page 75).

[133] P. Lömker, T. C. Rödel, T. Gerber, F. Fortuna, E. Frantzeskakis, P. Le Fèvre, F. ç. Bertran, M. Müller, and A. F. Santander-Syro, "Two-dimensional electron system at the magnetically tunable $EuO/SrTiO_3$ interface", Phys. Rev. Materials **1**, 062001 (2017) (cited on page 76).

[134] Z. Ren, X. Hu, X. Xue, and K. Chou, "Solid state reaction studies in Fe_3O_4–TiO_2 system by diffusion couple method", Journal of Alloys and Compounds **580**, 182 (2013) (cited on page 76).

[135] X. Zhang, S. Yang, Z. Yang, and X. Xu, "Kinetics and intermediate phases in epitaxial growth of Fe_3O_4 films from deposition and thermal reduction", Journal of Applied Physics **120**, 085313 (2016) (cited on pages 76, 101).

[136] T. Tsuchiya, K. Terabe, M. Ochi, T. Higuchi, M. Osada, Y. Yamashita, S. Ueda, and M. Aono, “In situ tuning of magnetization and magnetoresistance in Fe_3O_4 thin film achieved with all-solid-state redox device”, ACS Nano **10**, 1655 (2016) (cited on page 81).

[137] E. Liu, Y. Yin, L. Sun, Y. Zhai, J. Du, F. Xu, and H. Zhai, “Increasing spin polarization in Fe_3O_4 films by engineering antiphase boundary densities”, Applied Physics Letters **110**, 142402 (2017) (cited on page 81).

[138] D. Gilks, L. Lari, K. Matsuzaki, H. Hosono, T. Susaki, and V. K. Lazarov, “Structural study of Fe_3O_4(111) thin films with bulk like magnetic and magnetotransport behaviour”, Journal of Applied Physics **115**, 17C107 (2014) (cited on page 81).

[139] J. Janek and C. Korte, “Electrochemical blackening of yttria-stabilized zirconia – morphological instability of the moving reaction front”, Solid State Ionics **116**, 181 (1999) (cited on page 87).

[140] B. Savoini, C. Ballesteros, J. E. Muñoz Santiuste, R. González, and Y. Chen, “Thermochemical reduction of yttria-stabilized-zirconia crystals: optical and electron microscopy”, Phys. Rev. B **57**, 13439 (1998) (cited on page 87).

[141] V. M. Orera, R. I. Merino, Y. Chen, R. Cases, and P. J. Alonso, “Intrinsic electron and hole defects in stabilized zirconia single crystals”, Phys. Rev. B **42**, 9782 (1990) (cited on page 88).

[142] M. H. Hamed, D. N. Mueller, and M. Müller, “Thermal phase design of ultrathin magnetic iron oxide films: from Fe_3O_4 to γ-Fe_2O_3 and feo”, J. Mater. Chem. C **8**, 1335 (2020) (cited on page 89).

[143] F. Genuzio, A. Sala, T. Schmidt, D. Menzel, and H.-J. Freund, “Interconversion of α-Fe_2O_3 and Fe_3O_4 thin films: mechanisms, morphology, and evidence for unexpected substrate participation”, The Journal of Physical Chemistry C **118**, 29068 (2014) (cited on page 89).

[144] M. Rioult, D. Stanescu, E. Fonda, A. Barbier, and H. Magnan, “Oxygen vacancies engineering of iron oxides films for solar water splitting”, The Journal of Physical Chemistry C **120**, 7482 (2016) (cited on page 89).

[145] C. Schlueter, M. Lübbe, A. Gigler, and W. Moritz, “Growth of iron oxides on Ag(111) — reversible Fe_2O_3/Fe_3O_4 transformation”, Surface Science **605**, 1986 (2011) (cited on page 89).

[146] N. S. McIntyre and D. G. Zetaruk, “X-ray photoelectron spectroscopic studies of iron oxides”, Analytical Chemistry **49**, 1521 (1977) (cited on page 91).

[147] A. P. Grosvenor, B. A. Kobe, M. C. Biesinger, and N. S. McIntyre, “Investigation of multiplet splitting of Fe 2p XPS spectra and bonding in iron compounds”, Surface and Interface Analysis **36**, 1564 (2004) (cited on page 91).

[148] G. Ketteler, W. Weiss, W. Ranke, and R. Schlögl, “Bulk and surface phases of iron oxides in an oxygen and water atmosphere at low pressure”, Phys. Chem. Chem. Phys. **3**, 1114 (2001) (cited on pages 95, 101, 110).

[149] F. Bertram, C. Deiter, K. Pflaum, M. Suendorf, C. Otte, and J. Wollschläger, "In-situ X-ray diffraction studies on post-deposition vacuum-annealing of ultra-thin iron oxide films", Journal of Applied Physics **110**, 102208 (2011) (cited on page 101).

[150] P. Lömker, "Interfacing EuO in confined oxide and metal heterostructures", englisch, PhD thesis (Zugleich: Dissertation, Universität Dortmund, 2017, Jülich, 2018), VI, 140 Seiten (cited on page 126).

[151] M. Hoppe, "Magnetic, structural, and electronic properties of $NiFe_2O_4$ ultrathin films", englisch, PhD thesis (Zugleich: Duisburg, Universität, Dissertation, 2016, Jülich, 2016), VII, 118 Seiten (cited on page 126).

Acknowledgements

In the beginning, I would like to thank the Ph.D. committee for reading my thesis and their generous support:

Prof. Dr. Martina Müller (Konstanz University)

Prof. Dr. Claus M. Schneider (Duisburg-Essen University)

Prof. Dr. Ulf Wiedwald (Duisburg-Essen University)

Prof. Dr. Björn Sothmann (Duisburg-Essen University)

I would also like to thank **Dr. Connie Bednarski-Meinke** for the language corrections for my thesis.

This thesis has been done through the support of many people. I want to express my gratitude to:

Prof. Dr. Claus M. Schneider, for giving me the chance to be a member of PGI-6 and his guidance and continuous support.

Prof. Dr. Martina Müller, for her helpful advice and valuable discussions, which helped me immensely. I am most thankful for allowing me to be a part of "Oxide Spintronics Laboratory" group.

Dr. David Müller, for all the educative and helpful discussions on thermodynamic potentials.

Dr. Carolin Schmitz-Antoniak, Dr. Tomáš Duchoň and Dr. Stefan Cramm, for sharing their valuable knowledge and experience in the field of XMCD.

I would like to thank all the Ph.D. students who have been a part of the "Oxide Spintronics Laboratory" group. Thanks for **Marek Wilhelm, Patrick Lömker, Paul Rosenberger, and Thomas Szyjka**. Special thanks to **Ronja Anjka Hinz** for your

constant support with discussions and suggestions and your devoted guidance. Thanks for your countless lessons about working in the PLD laboratory and motivating me for my further work. Thanks for being my closest friend.

I am grateful for all the Ph.D. students in PGI-6 and FZ Jülich for being good friends and making my life enjoyable: especially **Umut, Pika, Tristan, Anjka, Asmaa and Katrin**.

I would like to thank **Berthold Schmitz, Georg Pickartz, Thomas Jansen, René Borowski, Heinz Pfeiffer and Norbert Schnitzler** for their technical support.

I thank **Prof. Dr. Regina Dittmann** (PGI-7) for providing the PLD setup. As well as, **Dr. Felix Gunkel** for his support during working in the PLD and XRD laboratory.

I thank **Prof. Dr. Thomas Brückel** (JCNS-2 / PGI-4) for providing the Quantum Design Dynacool PPMS and **Dr. Oleg Petracic** for all the discussions about the VSM and magnetism.

I am grateful to **Dr. Hebatalla Elnaggar** (Debye Institute) for sharing her expertise and generous support to do the XMCD calculations.

I want to thank the beamline staff at the beamlines:

- KMC-1 (BESSY, HZB, Berlin): **Roberto Felix Duarte**,
- P22 – former P09 (PETRA III, DESY, Hamburg): **Andrei Gloskovskii and Christoph Schlueter**,
- I10 (Diamond Light Source, Didcot): **Peter Bencok**.

I am endlessly thankful to my husband **Waleed Esmail**. Thanks for your constant support on both personal and scientific levels. Thank you for reading my thesis.

Last but not least, I thank my friends and family. I am forever thankful to my mother **Dr. Farha Mourad** and my father **Hussein Abdalla** for their continuous love and support. I thank my brother **Moustafa Hussein** for his positive and energetic spirit.

Curriculum Vitae

Personal information

Name	**Mai Hussein Abdalla Hamed**
Address	**Wiesenstr. 6G, 52428 Jülich**
Email	**maioush1@yahoo.com**
Birthday	**13.01.1988**
Birthplace	**Cairo, Egypt**
Nationality	**Egyptian**

Education

2016 – 2020	**Ph.D.**, Faculty of Physics, University of Duisburg-Essen, Germany Thesis title: *Interface Functionalization of Magnetic Oxide* $Fe_3O_4/SrTiO_3$ *Heterostructures*, PGI-6, Forschungszentrum Jülich GmbH
2014 – 2015	**Diploma**, Faculty of Science, Helwan University, Egypt.
05 – 08/2012	**Physicist**, Physics Department, Brock University, Canada.
2009 – 2013	**M.Sc.**, Faculty of Science, Helwan University, Egypt. Thesis title: *Magneto-electric Properties and Phase Transformation in Multiferroic Materials Based on Transition Metal Oxide.*
2008 – 2009	**Pre-Master**, Faculty of Science, Helwan University, Egypt.
2004 – 2008	**B.Sc.**, Faculty of Science, Helwan University, Egypt.

Own Publications

1. Preparation Parameters Optimization and Structure Investigation of Multiferroic Bismuth Ferrite, H. M. Hashem and **M. H. Hamed**, Materials Chemistry and Physics, 2018, **211**, 445-451. `DOI:10.1016/j.matchemphys.2018.03.012`.

2. Tunable Magnetic Phases at Fe_3O_4/$SrTiO_3$ Oxide Interfaces, **M. H. Hamed**, R. A. Hinz, P. Lömker, M. Wilhelm, A. Gloskovskii, P. Bencok, C. Schmitz-Antoniak, H. Elnaggar, C. M. Schneider and M. Müller, ACS applied materials & interfaces, 2019, **11**(7), 7576-7583. `DOI:10.1021/acsami.8b20625`.

3. Thermal Phase Design of Ultrathin Magnetic Iron Oxide Films: From Fe_3O_4 to γ-Fe_2O_3 and FeO, **M. H. Hamed**, D. N. Mueller and M. Müller, Journal of Materials Chemistry C, 2020, **8**, 1335-1343. `DOI:10.1039/c9tc05921k`.

4. Probing the Local distortion of Fe Sites in Fe_3O_4 Thin-films Using the Enhanced Symmetry Selectivity of XMLD, H. Elnaggar, R. Wang, M. Ghiasi, M. Yañez, M. U. Delgado-Jaime, **M. H. Hamed**, A. Juhin, S. S. Dhesi and F. de Groot, Physical Review Materials, 2020, **4**, 024415. `DOI:10.1103/PhysRevMaterials.4.024415`.

Conference Contributions

1. Thermal phase transformations through iron oxides/ oxide substrates interfaces, **M. H. Hamed**, D. N. Mueller, T. Duchoň, R. A. Hinz, C. M. Schneider and M. Müller, Talk, DPG Spring Meeting in Dresden, March, 2020 (the conference did not take place because of coronavirus (COVID-19)).

2. Thermal phase design of ultrathin magnetic iron oxide films: From Fe_3O_4 to γ-Fe_2O_3 and FeO, **M. H. Hamed**, T. Duchon, D. N. Mueller, S. Cramm, T. Szyjka and M. Müller, Poster, 11th Joint BER II and BESSY II User Meeting, Berlin, December, 2019.

3. Tunable magnetic phases at $Fe_3O_4/SrTiO_3$ oxide interfaces, **M. H. Hamed**, R. A. Hinz, M. Wilhelm, A. Gloskovskii, P. Bencok, C. Schmitz-Antoniak, H. Elnaggar, C. M. Schneider and M. Müller, Talk, DPG Spring Meeting in Regensburg, April, 2019.

4. Live monitoring of interfacial chemical transition by hard X-rays, **M. H. Hamed**, R. F. Duarte, C. M. Schneider and M. Müller, Poster, IFF Spring School, Jülich , March, 2019.

5. Live monitoring of oxygen diffusion in $Fe_3O_4/SrTiO_3$ heterointerfaces by hard X-rays, **M. H. Hamed**, R. A. Hinz, P. Rosenberger, T. Szyjka, R. F. Duarte, C. M. Schneider and M. Müller, Poster, 10th Joint BER II and BESSY II User Meeting, Berlin, December, 2018.

6. Magnetic and electronic properties of $Fe_3O_4/SrTiO_3$ heterointerfaces monitored by X-rays, **M. H. Hamed**, R. A. Hinz, M. Wilhelm, P. Lömker, A. Gloskovski, W. Drube, C. M. Schneider and M. Müller, Poster, 9th JEMS Conference, Mainz, September, 2018.

7. Magnetoelectronic structure of ultrathin Fe_3O_4/$SrTiO_3$ heterointerfaces, **M. H. Hamed**, R. A. Heinen, M. Wilhem, P.Lömker, C. Schmitz-Antoniak, A. Gloskovsky, W. Drube, C. M. Schneider and M. Müller, Poster, DPG Spring Meeting in Berlin, March, 2018.
8. Influence of interface electronic structure on Verwey and magnetic structure of Fe_3O_4 ultrathin films, **M.H.Hamed**, R.A.Heinen, C.M.Schneider and M.Müller, Poster, POF meeting, Forschungszentrum Jülich (PGI 6), October, 2017.
9. Influence of growth temperature on stoichiometry and Verwey transition of magnetite thin films, **M.H.Hamed**, R.A.Heinen, C.M.Schneider and M.Müller, Poster, Bad Honnef Physics School, September, 2017.
10. Magnetoelectric properties and phase transformation in multiferroic materials based on transition metal oxide, **M.H.Hamed**, H.M.Hashem, S.Soltan, A.Abdel Aal and A. A. Ramadan, Poster, SESAME 13th User Meeting, Jordan, November, 2015.
11. Optimization of preparation parameters and properties investigation of applicable room temperature multiferroic $BiFeO_3$, **M.H.Hamed**, S.Soltan, A.Abdel Aal, A.Moustafa and A.A.Ramadan, Talk, Workshop of application of advanced materials in industry under the frame of DAAD and BMBF, German University in Cairo, June, 2013.

Erklärung

Hiermit erkläre ich, dass ich die vorliegende Arbeit selbständig und ohne fremde Hilfe verfasst habe. Ferner habe ich außer den angegebenen Quellen keine anderen Quellen und Hilfsmittel benutzt. Die dem Sinn oder Wortlaut nach entnommen Textpassagen oder Abbildungen habe ich in jedem Einzelfall kenntlich gemacht. Dieser Dissertation geht weder ein erfolgloser Promotionversuch voraus, noch wurde sie in einem weiteren Promotionsverfahren eingereicht. Abgesehen von den angegebenen Publikationen sind die Ergebnisse dieser Dissertation unveröffentlicht. Diese Dissertation, die den Doktorgrad "Dr. rer. nat" anstrebt, wurde von Prof. Dr. C. M. Schneider betreut.

Jülich, 6/2020

Mai Hussein Abdalla Hamed

Band / Volume 219
Postnatale Ontogenesestudie (Altersstudie) hinsichtlich der Zyto- und Rezeptorarchitektonik im visuellen Kortex bei der grünen Meerkatze
D. Stibane (2020), 135 pp
ISBN: 978-3-95806-473-7

Band / Volume 220
Inspection Games over Time: Fundamental Models and Approaches
R. Avenhaus und T. Krieger (2020), VIII, 455 pp
ISBN: 978-3-95806-475-1

Band / Volume 221
High spatial resolution and three-dimensional measurement of charge density and electric field in nanoscale materials using off-axis electron holography
F. Zheng (2020), xix, 182 pp
ISBN: 978-3-95806-476-8

Band / Volume 222
Tools and Workflows for Data & Metadata Management of Complex Experiments
Building a Foundation for Reproducible & Collaborative Analysis in the Neurosciences
J. Sprenger (2020), X, 168 pp
ISBN: 978-3-95806-478-2

Band / Volume 223
Engineering of *Corynebacterium glutamicum* towards increased malonyl-CoA availability for polyketide synthesis
L. Milke (2020), IX, 117 pp
ISBN: 978-3-95806-480-5

Band / Volume 224
Morphology and electronic structure of graphene supported by metallic thin films
M. Jugovac (2020), xi, 151 pp
ISBN: 978-3-95806-498-0

Band / Volume 225
Single-Molecule Characterization of FRET-based Biosensors and Development of Two-Color Coincidence Detection
H. Höfig (2020), XVIII, 160 pp
ISBN: 978-3-95806-502-4

Band / Volume 226
Development of a transcriptional biosensor and reengineering of its ligand specificity using fluorescence-activated cell sorting
L. K. Flachbart (2020), VIII, 102 pp
ISBN: 978-3-95806-515-4

Band / Volume 227
Strain and Tool Development for the Production of Industrially Relevant Compounds with *Corynebacterium glutamicum*
M. Kortmann (2021), II, 138 pp
ISBN: 978-3-95806-522-2

Band / Volume 228
Complex magnetism of nanostructures on surfaces:
from orbital magnetism to spin excitations
S. Brinker (2021), III, 208 pp
ISBN: 978-3-95806-525-3

Band / Volume 229
High-throughput All-Electron Density Functional Theory Simulations
for a Data-driven Chemical Interpretation of X-ray Photoelectron Spectra
J. Bröder (2021), viii, 169, XL pp
ISBN: 978-3-95806-526-0

Band / Volume 230
Molecular tools for genome engineering of *Corynebacterium glutamicum*
C. K. Sonntag (2021), VIII, 111 pp
ISBN: 978-3-95806-532-1

Band / Volume 231
Interface Functionalization of Magnetic Oxide Fe_3O_4/$SrTiO_3$ Heterostructures
M. H. A. Hamed (2021), xvii, 151 pp
ISBN: 978-3-95806-535-2

Weitere ***Schriften des Verlags im Forschungszentrum Jülich*** unter
http://wwwzb1.fz-juelich.de/verlagextern1/index.asp

Schlüsseltechnologien / Key Technologies
Band / Volume 231
ISBN 978-3-95806-535-2

Mitglied der Helmholtz-Gemeinschaft

JÜLICH
Forschungszentrum